Astronomy Letters, Vol. 30, No. 2, 2004, pp. 100–116. Translated from Pis'ma v Astronomicheskiĭ Zhurnal, Vol. 30, No. 2, 2004, pp. 121–138.
Original Russian Text Copyright © 2004 by Matveyenko, Zakharin, Diamond, Graham.

Evolution of the Structure of the H_2O Supermaser Outburst Region in Orion KL

L. I. Matveyenko[1*], **K. M. Zhakharin**[1], **P. J. Diamond**[2], and **D. A. Gram**[3]

[1] *Space Research Institute, ul. Profsoyuznaya 84/32, Moscow, 117997 Russia*
[2] *Nuffield Radio Observatory, Macclesfield, Cheshire SK11, 9DL, UK*
[3] *Max-Planck-Institut für Radioastronomie, Auf dem Hügel 69, 53121 Bonn, Germany*

Received August 7, 2003

Abstract—During the period 1979–1999, we investigated the hyperfine structure of the H_2O supermaser region located in the core of the molecular cloud OMC-1 in Orion KL. The angular resolution is 0.1 mas, which corresponds to 0.045 AU. The detected structure, which consists of a central object, an accretion disk, a bipolar outflow, and an envelope, corresponds to the initial formation stage of a low-mass star. The accretion disk is at the stage of separation into groups of concentric rings. The bipolar outflow is a neutral, highly collimated jet of accreted material that includes H_2O molecules and dust grains in the icy envelope. The injector is a bright compact source with a size <0.05 AU and a brightness temperature $T_\mathrm{b} \approx 10^{17}$ K. The velocity of the bipolar outflow is $v \approx 10$ km s^{-1}. The rotation velocity of the jet is $v_\mathrm{rot} \approx 1.5$ km s^{-1}. The jet has the shape of a conical helix due to the precession of the rotation axis. Occasionally, dense blobs (comet-shaped bullets) are ejected. The envelope amplifies the radio emission from the structures in a $\sim$0.5 km s^{-1} maser window band with velocities $v \approx 7.65$ km s^{-1} by more than two orders of magnitude. *© 2004 MAIK "Nauka/Interperiodica".*

Key words: *interstellar medium, gaseous nebulae.*

INTRODUCTION

Galactic gas–dust complexes are unique space laboratories with a broad spectrum of physical conditions. Gravitational instability gives rise to local active zones in them in which protostars are formed. The star-formation processes are assumed to be collective in nature (Ambartsumyan 1953, 1980). Water-vapor line observations confirmed this assumption (Genzel *et al.* 1978). The ages of these compact regions, $\sim 10^4$ yr, suggest that they are associated with hot young stars. Low-mass ($<0.1 M_\odot$) stars are formed through gravitational collapse (Turner 1988). The physical and chemical processes in active zones produce both simple and complex molecules and are accompanied by intense water-vapor maser emission. However, it is not clear what star-formation phase this emission accompanies. Maser emission can originate both from outer regions of the protostar itself and from nearby gas–dust structures where planets and comets are formed. Dense massive blobs may contract into planets before they are swept out into interstellar space, much as is the case with low-mass accelerated blobs that escape from the gravitational sphere of the star (Strelnitskij 1974, 1984). Star formation is accompanied by the formation of an accretion disk (Matveyenko 1981; Bachiller 1984, 1996). Intense H_2O maser emission probably accompanies the initial formation phase of stars and planetary systems, which are dynamically unstable systems (Shklovsky 1967; Litvak 1969). The water-vapor molecular emission corresponds to the 6_{16}–5_{23} rotational transition at frequency $f = 22\,235.08$ MHz, $\lambda = 1.35$ cm. The H_2O maser emission is linearly polarized, and the degree of polarization reaches $\sim$40%. The intensity of the emission and the degree of its polarization vary with time. In some cases, unusually high activity is observed—the intensity of the emission of one of the spectral lines increases by several orders of magnitude. This phenomenon was first observed on June 6, 1971, in the object W49. The radio flux density in the $v = -1.8$ km s^{-1} line increased by more than an order of magnitude. Measurements with the Simeiz–Haystack radio interferometer show that the angular size of the outburst region did not exceed 0.2 mas and that its brightness temperature reached $T_\mathrm{b} \approx 10^{16}$ K (Burke *et al.* 1972, 1973). Thus, H_2O maser emission is a tracer of ongoing processes and opens up wide possibilities for detecting and investigating the spatial structure and growth dynamics of active zones

---

[*] E-mail: `lmatveen@mx.iki.rssi.ru`

by the VLBI method. In this paper, we present the results of our long-term studies of the fine structure of the Orion Nebula, one of the most interesting objects in the Galaxy.

STUDIES OF THE ACTIVE REGION IN THE COMPLEX ORION KL

The Orion Nebula is one of the most interesting gas–dust complexes in the Galaxy. VLBI observations show that compact H_2O maser sources are concentrated in eight active zones with sizes reaching 2×10^3 AU. The maser flux density for the strongest sources exceeds $F > 10$ kJy. The sizes of the sources are ~0.5 AU, and their velocities lie within the range of -8 to 20 km s^{-1}. Some of them are dense maser clouds embedded in a low-velocity ($v \approx 18$ km s^{-1}) flow of matter. In other cases, they belong to a high-velocity flow, and their velocities are 30–100 km s^{-1} (Genzel *et al.* 1978). The beginning of high activity for one of the zones was observed on September 24, 1979. The radio flux density in the $v \approx 8$ km s^{-1} line increased to 500 kJy and reached 2 MJy on October 15 (Abraham *et al.* 1981; Matveyenko *et al.* 1980). The high activity lasted until 1987 and was accompanied by strong radio outbursts reaching $F \approx 8$ MJy, which corresponded to a brightness temperature $T_b \approx 10^{17}$ K. The outburst emission had a high degree of polarization $P > 60\%$ and was concentrated in a narrow line $\Delta f \approx 30$ kHz in width (Matveyenko *et al.* 1980, 1982; Matveyenko 1981; Abraham *et al.* 1981, 1986; Garay *et al.* 1989).

We investigated active zones in Orion KL in H_2O maser emission, determined the characteristic structures of star-forming regions at early formation stages, studied the evolution of the structures, and established their association with supermaser outbursts. We observed Orion KL during the first (1979–1987) and second (1998–1999) epochs of high activity and the period of quiescence. The measurements during the first period of activity, when the radio flux density in the $v \approx 8$ km s^{-1} line occasionally exceeded $F > 4$ MJy, were carried out using a global radiointerferometric network. The studies were continued in a wide dynamic range in 1995 with the VLBA (Very Large Baseline Array) during the period of quiescence, when the maser flux density in the expected velocity range did not exceed 500 Jy, and during the second period of activity, when the flux density was $F \geq 1$ MJy. The angular resolution reached 0.1 mas, which corresponds to 0.045 AU at a distance of 450 pc to the Orion Nebula. Below, we present the results of our studies of the hyperfine structure of this active zone.

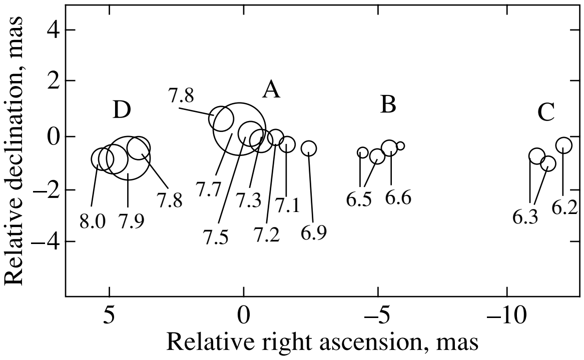

Fig. 1. Structure of the H_2O supermaser region at the first epoch of activity in October 1985. The circle diameters correspond to the flux density of the component on a logarithmic scale (the largest circle corresponds to the source's brightness temperature $T_b = 10^{17}$ K). The velocities of the components are also shown here.

THE 1979–1987 EPOCH OF ACTIVITY

H_2O supermaser outbursts in the $v \approx 8$ km s^{-1} line were observed in Orion KL during 1979–1987. The line profile had a low-velocity tail, and the line FWHM was $\Delta f \approx 30$ kHz (Matveyenko *et al.* 1980, 1982; Abraham *et al.* 1981, 1986; Matveyenko 1981; Garay *et al.* 1989). The duration of the outbursts reached several months, but the duration of one of them did not exceed two days.

The position of the supermaser region was measured with the VLA (Very Large Array) in April 1982 when the flux density reached $F = 0.5$ MJy (Garay *et al.* 1989):

$$\alpha = 05^{\mathrm{h}}32^{\mathrm{m}}46\overset{\mathrm{s}}{.}64 \pm 0\overset{\mathrm{s}}{.}01,$$

$$\delta = -05^\circ 24' 29\overset{''}{.}8 \pm 0\overset{''}{.}1 \; (1959.0).$$

The coordinates of the region were refined by using VLA observations in 1983, $F \approx 0.5$ MJy (Greenhill *et al.* 1998):

$$\alpha = 05^{\mathrm{h}}35^{\mathrm{m}}14\overset{\mathrm{s}}{.}121 \pm 0\overset{\mathrm{s}}{.}003,$$

$$\delta = -05^\circ 22' 36\overset{''}{.}27 \pm 0\overset{''}{.}05 \; (2000.0).$$

We investigated the spatial structure of this region in Orion KL at the initial stage of activity in September 1979 using the Simeiz–Pushchino radio interferometer. The H_2O maser emission with $F = 0.5$ MJy was concentrated in a $\Delta f = 30$ kHz band and was determined by a compact source located at the edge of an elongated extended component. The size of the source was 0.25 AU, and its brightness temperature was $T_b = 5 \times 10^{15}$ K. The size of the elongated extended component was 2.5 AU, and its brightness temperature was $T_b = 3 \times 10^{14}$ K. The velocity of the component was lower than the velocity

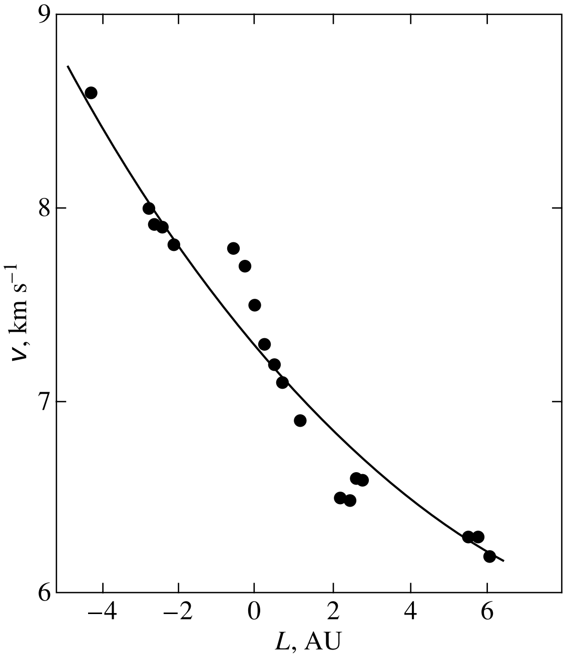

Fig. 2. Velocity of the components versus their relative positions.

of the compact source, which determined the low-velocity tail of the profile. Subsequent studies showed that the outburst region was a highly organized structure in the form of an elongated chain of components. The VLBI observations in October 1985 using seven radio telescopes expanded the dynamic range of the measurements and allowed the structure of the supermaser region to be refined. A limiting angular resolution of 0.1 mas, or 0.045 AU, was achieved. The maser emission was concentrated in a narrow line $\Delta f = 42$ kHz in width, the peak flux density was $F \approx 2$ MJy, and $v \approx 7.7$ km s^{-1} (Matveyenko *et al.* 1988). The emission intensity of the low-velocity tail in the line profile was conserved, but its relative contribution decreased due to an increase in the intensity in the central part of the line profile.

The structure of the outburst region is an elongated chain, 21.6 mas (10.8 AU) in length, that consists of five groups of compact sources distributed roughly in the E–W direction. The positions and velocities of the sources are shown in Fig. 1. The circle diameters are proportional to the logarithm of the flux density for the sources. The brightness of the eastern group is low and is not shown in this figure. The sizes of the compact sources do not exceed 0.2 mas or 0.1 AU. The brightness temperatures of the components are $T_\mathrm{b} \approx 10^{15}$–$10^{17}$ K (Matveyenko *et al.* 1988, 1992). The velocities of the group increase along the chain from $v_\mathrm{W} = 6.2$ km s^{-1} to $v_\mathrm{E} = 8.7$ km s^{-1}, which, to a first approximation, corresponds to a velocity gradient $\Delta v/\Delta L \approx 0.28$ km s^{-1} AU^{-1}. The velocities of the components are plotted against their positions in Fig. 2. Group A consists of seven components distributed in a chain of ~60°. The length of the chain is 4 mas, or 2 AU. The velocities of the sources smoothly change along the chain from 7.8 km s^{-1} of the eastern component to 6.9 km s^{-1} of the western component.

The maser emission was linearly polarized, and the degree of its polarization exceeded $P \geq 70\%$. The position angle of the polarization X changed monotonically within the line profile. The polarization gradient is $\Delta X/\Delta v \approx 25°$/km s^{-1}. This suggests that a certain orientation of the polarization corresponds to each group, and its change along the chain is $\Delta X/\Delta L \approx 7$ deg AU^{-1} (Matveyenko 1994).

The supermaser region is located in the core of a dense molecular cloud, OMC-1 (Orion KL), which also contains H_2O molecules. Our improved estimate of the cloud velocity is $v = 7.65$ km s^{-1} (Matveyenko *et al.* 1998). This medium or envelope of the structure under consideration amplifies the emission from the components whose velocities lie within a $\Delta v \approx \pm 0.3$ km s^{-1} maser window by more than two orders of magnitude. The conservation of the outburst velocity is explained in the same way.

The highly organized structure, a chain of compact components, may be represented as an accretion disk at the stage of separation into protoplanetary rings observed edge-on. An edge-on ring represents two components connected by a bar. The compact components correspond to the tangential directions of the ring. The optical depth in the tangential directions is much larger than that in the ring cross section, and the unsaturated maser emission from the compact sources will be many orders of magnitude more intense than the bar emission. The velocities of the compact sources are determined by the rotation velocity of the ring, but they differ in sign. The envelope, a narrow active filter, amplifies the emission from only one side of the ring whose velocity is equal to the velocity of the filter. Since the opposite side of the ring lies outside the filter band, its emission is not amplified and remains invisible. The ring emission is concentrated in the azimuthal plane. A nonuniform distribution of water-vapor molecules in the ring or nonuniform pumping lead to nonuniform maser emission in the azimuthal plane and, hence, to variable emission from a rotating ring.

In the model under consideration, the velocities and relative positions of the components are related by Keplerian motion: $Rv_\mathrm{rot}^2 = MG$. However, an active narrow-band filter limits the visibility of the components of the structure throughout the velocity spectrum. Data on the velocity of the protostar in the local standard of rest are also lacking. Its velocity may differ from the velocity of the molecular cloud OMC-1. Therefore, we obtained the solution in a model approximation for given masses of the protostar. Observational data agree with a protostar mass $M = (0.2–0.5)M_\odot$ (the curve in Fig. 2). In this case, the velocity in the local standard of rest is $v_{\rm LSR} \approx 5$ km s^{-1}, the radius of the inner ring is $R \approx 6$ AU, and its rotation velocity is $v_{\rm rot} \approx 5$ km s^{-1}. The expansion velocity of the ring is $v_{\rm exp} \approx 3.8$ km s^{-1} and changes as $v_{\rm exp} \sim R^{-0.5}$. The outer radius of the disk (outer ring) is $R \approx 16.5$ AU. The rotation velocity of the rings follows the Keplerian law. The distribution of the group-A components deviates from the orientation of the entire chain (Fig. 1), because the planes of the group-A concentric rings deviate from the disk plane.

The expansion of the rings suggests that the structure of the forming system is nonstationary. However, the maser rings containing water-vapor molecules could actually be not associated directly with the Keplerian rings, including the ice particles themselves. Stellar radiation and stellar wind sublimate water-vapor molecules and blow them away, much as is the case in comets. A halo of radially accelerated water-vapor molecules, an expanding maser ring, is formed around the ring. The emission from one of the parts of the ring whose velocity corresponds to the maser window of the envelope is amplified to a supermaser level. The emission from the opposite part of the ring is not amplified and is below the detection threshold.

THE EPOCH OF QUIESCENCE

The flux density of the H_2O-maser emission from Orion KL on May 25, 1995, in the expected velocity range $v = 7.5–8.5$ km s^{-1} did not exceed $F \approx 1$ kJy. We investigated a 100×100 mas area where the active region was located earlier. The velocity resolution was taken to be $\Delta v = 0.2$ km s^{-1}. The high sensitivity and the wide dynamic range of the system (~ -40 dB) allowed us to achieve a very high angular resolution, up to 0.1 mas, or 0.045 AU. There was no chain of compact components, rings or their bars, in the area under consideration, but we detected an elongated jet-type structure and two compact components, bullets (Fig. 3).

The jet has a symmetric S-like shape. The size of the jet reaches 18 mas, or 9.0 AU, while its thickness does not exceed 0.15 mas, or 0.07 AU. The bright middle part of the jet is oriented at an angle $X = -33°$. A bright elongated feature with sizes of 1.0×0.1 mas (0.5×0.05 AU) is located at the center; it is oriented at an angle $X = -44°$. This structure corresponds to the injector and the nearby part of the bipolar outflow. The total radio flux density of the jet is $F = 1060$ Jy. The emission is concentrated in a narrow line with a radial velocity $v \approx 7.63$ km s^{-1} and a width $\Delta v \approx 0.48$ km s^{-1}. The brightness temperature of the jet is $T_{\rm b} \leq 10^{12}$ K and, in the injector region, $T_{\rm inj} \approx 9 \times 10^{12}$ K. The velocity of the injector is $v_0 \approx 7.63$ km s^{-1}, while the relative longitudinal outflow velocity components are $v_{\rm NW} \approx 0.1$ km s^{-1} and $v_{\rm SE} \approx -0.1$ km s^{-1}.

The compact N–W component (a bullet) is at a distance of 55 mas, or 27 AU, from the injector in the direction $X = -54°$. The S–E bullet is at a distance of 44 mas, or 22 AU, in the direction $X = 140°$. The radial velocity components of the N–W and S–E bullets are $v_{\rm NW} \approx 7.45$ km s^{-1} and $v_{\rm SE} \approx 7.95$ km s^{-1}; i.e., their velocities relative to the injector are $\Delta v_{\rm NW} \approx -0.18$ km s^{-1} and $\Delta v_{\rm SE} \approx 0.32$ km s^{-1}, respectively. The velocities of the bullets are higher than those of the bipolar outflows of the jet and differ in sign. The latter may be attributable to both the difference between the directions of motion of the bullets and to their acceleration by radiation pressure and stellar wind. However, the bullets may be dense compact ice blobs injected at a velocity higher than the outflow velocity. In this case, their initial velocities and directions of motion can have a large spread and differ from one another. On the other hand, we are observing the structures through a narrow-band, active filter with a velocity $v = 7.65$ km s^{-1} and a width $\Delta v \approx 0.5$ km s^{-1}. Thus, we see only a limited velocity range of the water-vapor molecules in the outflow.

The impact of the environment on the bullet, including radiation pressure and stellar wind, forms its comet-type (head–tail) structure. As a result, a tail is formed; this tail can be in front of or behind the head (see Fig. 3), suggesting that the water-vapor molecules of the tail are accelerated to velocities higher or lower than the velocity of the dense head. The sizes of the S–E “comet” are 3×0.2 mas, or 1.5×0.1 AU; it is oriented at an angle $\alpha = -70°$. The maser radio flux density of the bullet is $F = 485$ Jy, and its brightness temperature is $T_{\rm peak} = 2.2 \times 10^{12}$ K. The N–W bullet is at a distance of 27.5 AU from the injector in the direction $X = -54°$. Its radio flux density, sizes, and brightness temperature are $F = 317$ Jy, 1.3×0.9 AU, and $T_{\rm b} = 1.7 \times 10^{12}$ K, respectively.

Polarization of the Emission

The maser emission from the jet and the bullets is linearly polarized. The degree of polarization of the jet emission in the central part is $P = 33\%$. It increases to $P = 45$ and 52% in the S–E and N–W parts of

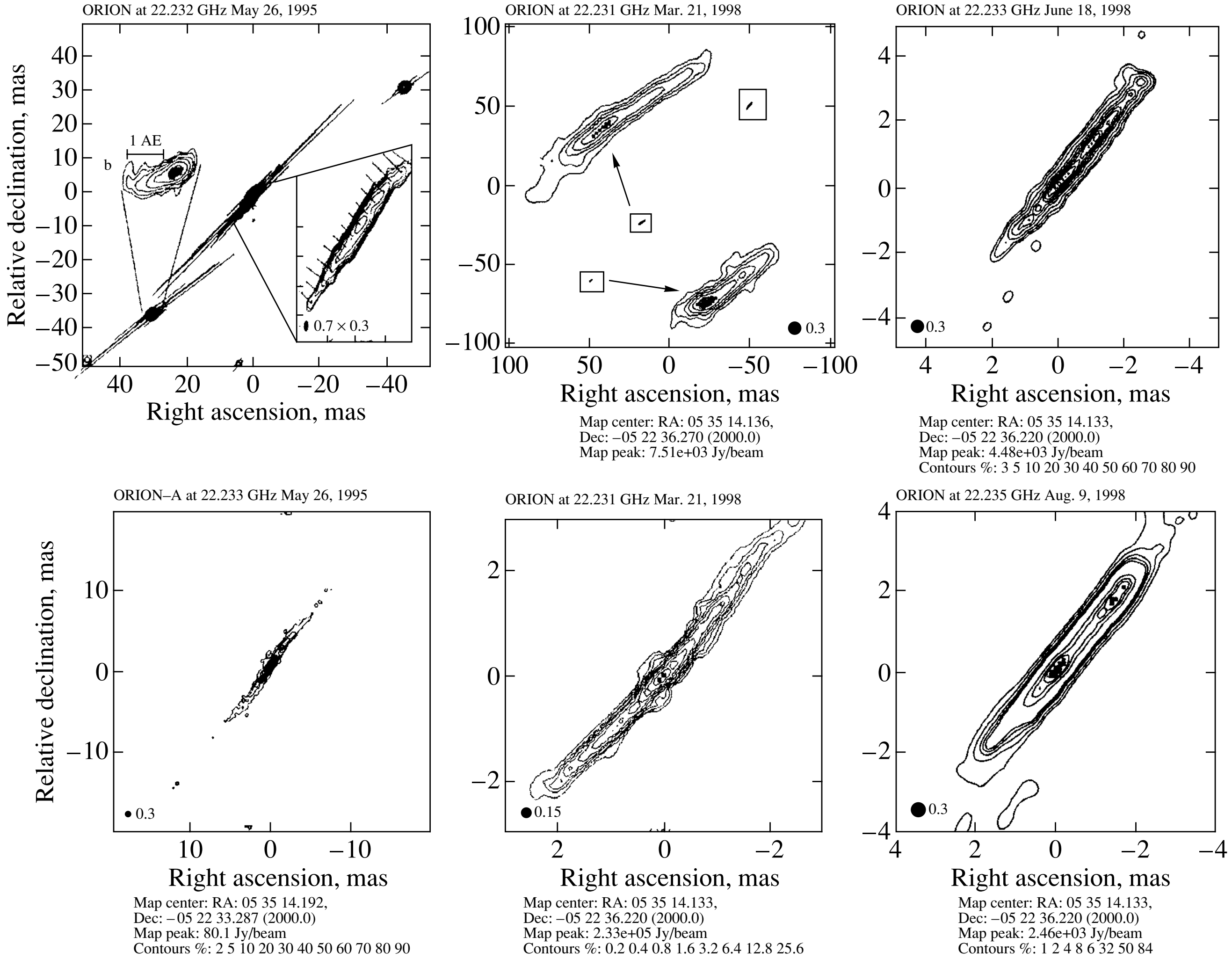

Fig. 3. Structure of the active region in H_2O maser emission. The angular resolution is shown at the bottom of each map. The peak brightnesses are in Jy/beam; the isophotal levels (in %) and the dates of measurements are indicated under and above the maps, respectively:

May 26, 1995, the epoch of quiescence: the bipolar jet and bullets are shown on an enlarged scale with an angular resolution $\varphi = 0.3 \times 0.7$ mas. The rectilinear segments correspond to the intensity level and orientation of the polarized emission. The position angle of the polarization on the large-scale map of the jet was rotated through 90°, $v = 7.8$ km s^{-1}

May 26, 1995, the jet structure with an increased angular resolution $\varphi = 0.3$ mas; the brightness temperature of the injector is $T_{\rm inj} = 3 \times 10^{12}$ K, $v = 7.8$ km s^{-1}.

March 21, 1998, the structure of the H_2O supermaser region with $\varphi = 0.3$ mas, also shown here are the bullet images on an enlarged scale, $v = 8$ km s^{-1}.

March 21, 1998, the jet structure with a very high angular resolution, $\varphi = 0.15$ mas, $T_{\rm inj} \approx 7 \times 10^{16}$ K, $v = 8$ km s^{-1}.

June 18, 1998, the jet structure with $\varphi = 0.3$ mas, $T_{\rm inj} \approx 4 \times 10^{16}$ K, $v = 8.26$ km s^{-1}.

August 9, 1998, the jet structure with $\varphi = 0.3$ mas, $T_{\rm inj} \approx 10^{16}$ K, $v = 8.11$ km s^{-1}.

October 14, 1998, the jet structure with $\varphi = 0.15$ mas, $T_{\rm inj} \approx 5 \times 10^{14}$ K, $v = 8.51$ km s^{-1}.

October 14, 1998, the jet structure with $\varphi = 0.15$ mas, $T_{\rm inj} \approx 1.5 \times 10^{17}$ K, $v = 7.59$ km s^{-1}.

December 6, 1998, the jet structure with $\varphi = 0.15$ mas, $T_{\rm inj} \approx 1.8 \times 10^{16}$ K, $v = 7.68$ km s^{-1}.

January 23, 1999, the jet structure with $\varphi = 0.15$ mas, $T_{\rm inj} \approx 3.6 \times 10^{16}$ K, $v = 7.58$ km s^{-1}.

March 12, 1999, the jet structure with $\varphi = 0.15$ mas, $T_{\rm inj} \approx 2 \times 10^{16}$ K, $v = 7.36$ km s^{-1}.

March 29, 1999, the jet structure with $\varphi = 0.15$ mas, $T_{\rm inj} \approx 4 \times 10^{17}$ K, $v = 7.5$ km s^{-1}.

April 24, 1999, the jet structure with $\varphi = 0.15$ mas, $T_{\rm inj} \approx 4.5 \times 10^{16}$ K, $v = 7.43$ km s^{-1}.

June 12, 1999, the jet structure with $\varphi = 0.15$ mas, $T_{\rm inj} \approx 5 \times 10^{15}$ K, $v = 7.16$ km s^{-1}.

August 11, 1999, the jet structure with $\varphi = 0.15$ mas, $T_{\rm inj} \approx 2 \times 10^{14}$ K, $v = 7.6$ km s^{-1}.

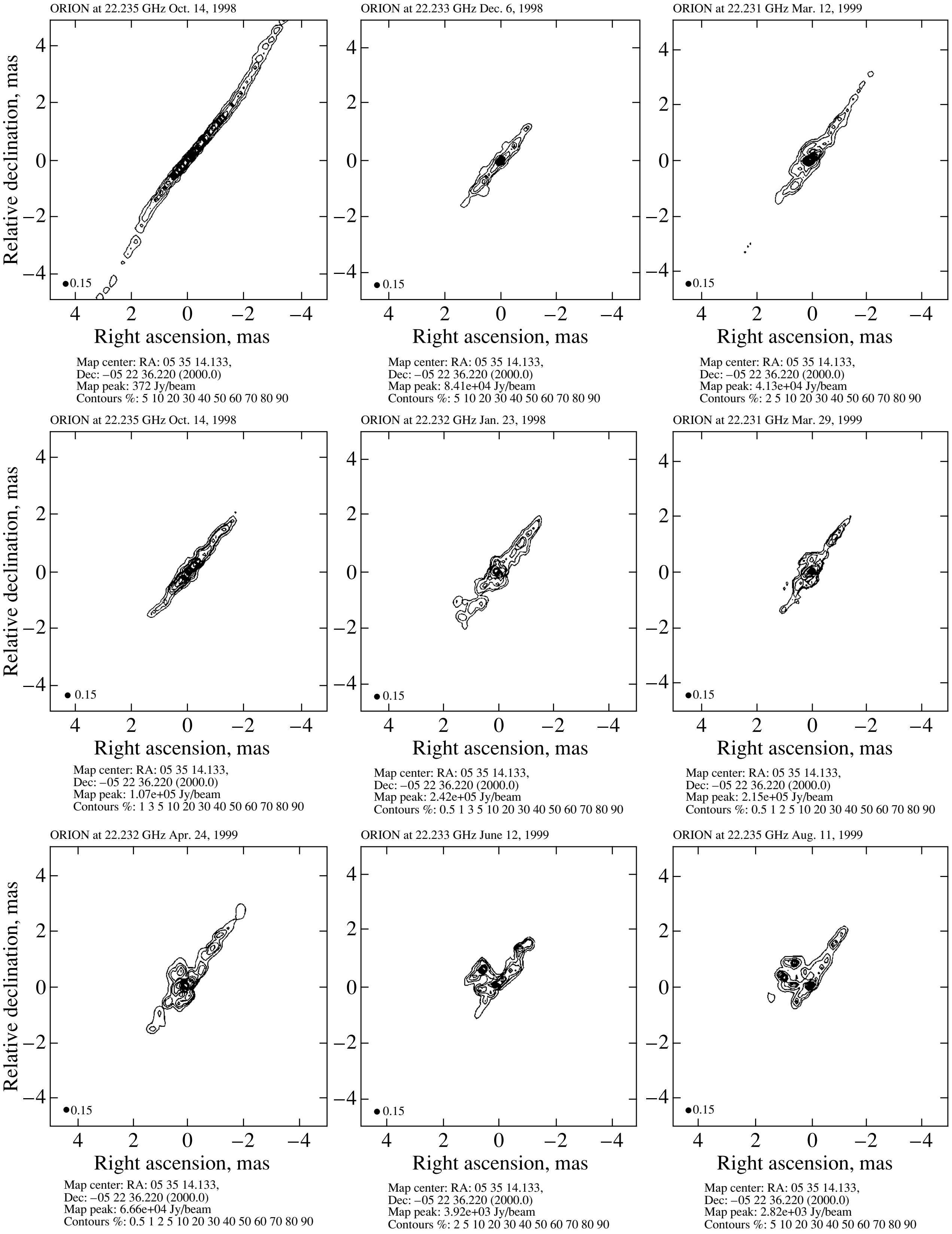

ORION at 22.235 GHz Oct. 14, 1998

Map center: RA: 05 35 14.133,
Dec: –05 22 36.220 (2000.0)
Map peak: 372 Jy/beam
Contours %: 5 10 20 30 40 50 60 70 80 90

ORION at 22.233 GHz Dec. 6, 1998

Map center: RA: 05 35 14.133,
Dec: –05 22 36.220 (2000.0)
Map peak: 8.41e+04 Jy/beam
Contours %: 5 10 20 30 40 50 60 70 80 90

ORION at 22.231 GHz Mar. 12, 1999

Map center: RA: 05 35 14.133,
Dec: –05 22 36.220 (2000.0)
Map peak: 4.13e+04 Jy/beam
Contours %: 2 5 10 20 30 40 50 60 70 80 90

ORION at 22.235 GHz Oct. 14, 1998

Map center: RA: 05 35 14.133,
Dec: –05 22 36.220 (2000.0)
Map peak: 1.07e+05 Jy/beam
Contours %: 1 3 5 10 20 30 40 50 60 70 80 90

ORION at 22.232 GHz Jan. 23, 1998

Map center: RA: 05 35 14.133,
Dec: –05 22 36.220 (2000.0)
Map peak: 2.42e+05 Jy/beam
Contours %: 0.5 1 3 5 10 20 30 40 50 60 70 80 90

ORION at 22.231 GHz Mar. 29, 1999

Map center: RA: 05 35 14.133,
Dec: –05 22 36.220 (2000.0)
Map peak: 2.15e+05 Jy/beam
Contours %: 0.5 1 2 5 10 20 30 40 50 60 70 80 90

ORION at 22.232 GHz Apr. 24, 1999

Map center: RA: 05 35 14.133,
Dec: –05 22 36.220 (2000.0)
Map peak: 6.66e+04 Jy/beam
Contours %: 0.5 1 2 5 10 20 30 40 50 60 70 80 90

ORION at 22.233 GHz June 12, 1999

Map center: RA: 05 35 14.133,
Dec: –05 22 36.220 (2000.0)
Map peak: 3.92e+03 Jy/beam
Contours %: 2 5 10 20 30 40 50 60 70 80 90

ORION at 22.235 GHz Aug. 11, 1999

Map center: RA: 05 35 14.133,
Dec: –05 22 36.220 (2000.0)
Map peak: 2.82e+03 Jy/beam
Contours %: 5 10 20 30 40 50 60 70 80 90

Fig. 3. (Contd.)

the jet. The position angle of the polarization in the central and N–W parts of the jet is $X = -45°$ and changes to $X = -38°$ in the S–E part. The degree of polarization and its position angle for the bullets are $P_{\rm NW} \approx 12.5\%$, $X \approx -55°$ and $P_{\rm SE} \approx 45°$, $X = -53°$, respectively (Fig. 3).

The observed orientation of the polarization plane actually differs from the initial one. Faraday rotation changes the orientation as the emission passes through the H II region located in front of the molecular cloud OMC-1. The electron density in the H II region is $N_e \sim 10^3$ cm^{-3}, while the magnetic field is $B \approx -(10-50)$ μG and is directed toward the observer. The size of the region along the line of sight is $l \approx 0.6$ pc (Turner 1988). The rotation measure is defined as $RM = \int N_e H dl$; in our case, it varies within the range $25 \times 10^3 > RM > -5 \times 10^3$ rad m^{-2}. The Faraday rotation is $X = RM\lambda^{-2}$; at a wavelength of 1.35 cm, it corresponds to $-5 < X < -1$ rad (Matveyenko *et al.* 1998, 2000). Such a wide range of position angles for the polarization plane does not allow its orientation to be compared with the orientation of the structure with the required accuracy.

Let us determine the orientation of the polarization plane of the emission from theoretical considerations. The linear polarization of the emission is determined by the spin alignment of the molecules in the environment. A static spin alignment arises in a thermodynamically equilibrium environment with a strong magnetic field. In our case, however, when a directed beam of emission or fast particles interacts with the environment in a nonequilibrium system, a dynamic spin alignment parallel or antiparallel to the outflow arises (Varshalovich 1970). The observed structures (the jet and the bullets) are the directed outflows of particles that interact with the environment. Both the outflows and the medium contain water-vapor molecules. The outflow aligns the spins of the particles in the environment and entrains them in the direction of its motion. The spins of the molecules in the beam itself are aligned in a similar way. Thus, the polarization plane of the maser emission is parallel to the outflow velocity. A similar conclusion follows from the papers by Western and Watson (1983, 1984): even a small pumping anisotropy ($\sim$10%) results in a high degree of polarization reaching $P \approx 90\%$, particularly in an unsaturated maser regime.

In our case, the maser emission from the structure is additionally amplified in the environment. The amplifying H_2O-maser environment can produce a particularly strong effect of spin alignment. Hyperfine level splitting takes place in the presence of a weak magnetic field. The intense beamed polarized monochromatic radio emission that corresponds to the resonance transition between the hyperfine-structure levels of the ground state aligns the particle spins at both resonance levels. The particle spins are parallel and directed mostly along or across the field. Even unpolarized emission becomes polarized after passing through an aligned environment. In this case, coherent amplification of the radio emission is possible (Varshalovich 1970). Thus, even a weak magnetic field increases significantly the degree of polarization.

Identification of the Supermaser Region

It was necessary to identify the detected structures with the ring structure of the preceding period of supermaser activity. We applied the standard procedure of determining the position of the synthesized beam from a reference quasar (the amplitude and phase calibration of the correlated signals). To increase the accuracy, we took the intense nearby compact source as the reference one and measured its coordinates from the fringe rate. The velocity of this reference source is $v = 6.37$ km s^{-1}, the line width is $\Delta v = 1.2$ km s^{-1}, and $F = 1300$ Jy. Its coordinates relative to the coordinates of the $v = 7.6$ km s^{-1} supermaser source are

$$\Delta\alpha = -879.1 \pm 8.4 \text{ mas},$$
$$\Delta\delta = -3163.0 \pm 59.6 \text{ mas (2000.0)}.$$

The relative positions of the H_2O-maser sources in Orion KL were measured with an accuracy of 10 mas on August 5, 1991, using the VLA (Gaume *et al.* 1998). The absolute error did not exceed $0''\!.1$. The coordinates of the source with a velocity $v = 7.6$ km s^{-1} and a maser radio flux density $F = 13.92$ kJy are

$$\alpha = 5^{\rm h}32^{\rm m}46^{\rm s}\!.646, \quad \delta = -05°24'29''\!.87 \text{ (1950.0)}.$$

Its coordinates relative to the source with a velocity $v = 6.3$ km s^{-1} and a flux density $F = 686$ Jy are

$$\Delta\alpha = -1010 \text{ mas}, \quad \Delta\delta = -3110 \text{ mas (1950.0)}.$$

The relative positions of the sources under consideration differ by

$$^2\Delta\alpha = 121 \text{ mas} \quad \text{and} \quad ^2\Delta\delta = 53 \text{ mas}.$$

The relative declinations are virtually equal, within the limits of the measurement errors. In contrast, the right ascensions are outside these limits. The observed discrepancy may be attributable to the complex structure of the components under consideration, which were measured with the markedly differing angular resolutions of the VLA and VLBI systems. Changes in the coordinates over the period from 1991 until 1995 are also possible. Thus, the positions of the areas under study coincide, to within ±50 mas, in both coordinates.

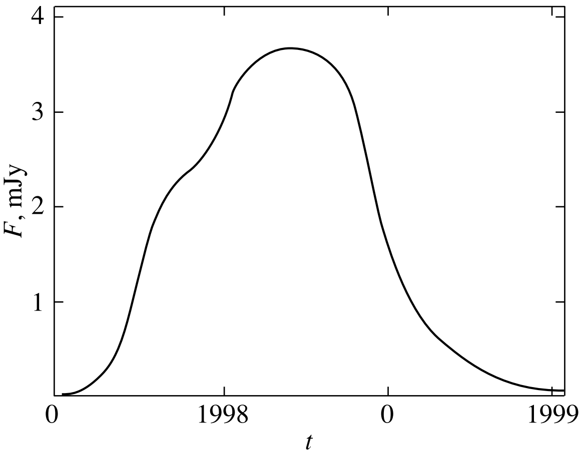

Fig. 4. Variation in the flux density of the maser emission from the outburst during the second period of activity.

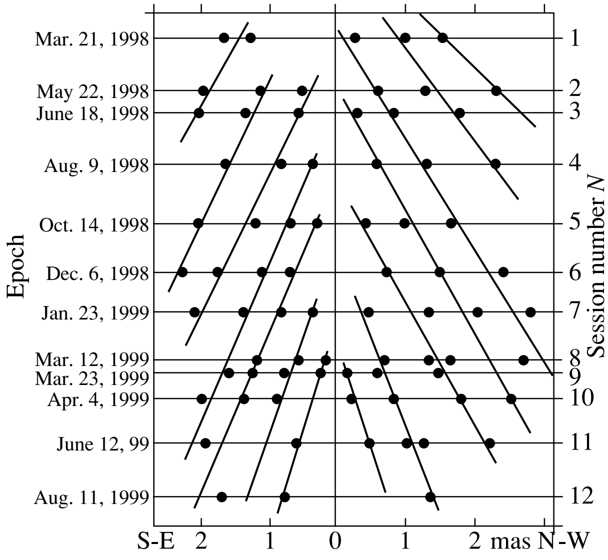

Fig. 5. Motion of the bullets in the jet at various epochs.

THE 1998–1999 PERIOD OF ACTIVITY

At the end of 1997, the H_2O-maser emission at a velocity $v \approx 7.7$ km s^{-1} was much more intense than the emission during the period of quiescence; it corresponded to the normal flux density for the low-velocity components, $F = 14$ kJy. In the period August–October 1998, the flux density of the emission reached $F \approx 4.3$ MJy (Omodaka *et al.* 1998; Kobayashi *et al.* 2000; Tolmachev 2000). The emission was concentrated in a line with a width $\Delta v \approx 0.5$ km s^{-1}. Within the measurement accuracy, the radio flux density of the outburst increased in two stages. At the first stage, before April 1998, the flux density rose exponentially and reached $F \approx 2.4$ MJy. Subsequently, in June 1998, the second stage began, and the flux density was 4.3 MJy in August. In November, a general exponential decline in emission intensity was observed, and the emission returned to its original level in May–June 1999 (Fig. 4). The development of activity was accompanied by certain changes in the structure of the emission region. We investigated the hyperfine structure of the active outburst region over the entire period of its development. Below, we consider the structure of the outburst region and its evolution at the separate stages.

Structure of the Outburst Region at the Initial Stage

At the first stage of the outburst (March–October 1998), the structure of the emitting region was virtually the same as that during the period of quiescence: a core, a bipolar jet, and bullets (see Fig. 3). Its S-like shape was also retained. The apparent sizes of the jet and the core were $\sim 8 \times 0.15$ mas and ~ 0.1 mas, respectively. However, the brightness of the components increased significantly (Matveyenko *et al.* 2001). Compared to the period of quiescence, the brightness temperature of the jet increased by three orders of magnitude and reached $T_{\rm jet} \approx 2 \times 10^{15}$ K, while the brightness temperature of the central compact core (injector) increased by four orders of magnitude, $T_{\rm b} \approx 5 \times 10^{16}$ K. The velocities of the N–W and S–E parts of the jet relative to the injector were $v_{\rm NW} \approx -0.3$ km s^{-1} and $v_{\rm SE} \approx 0.3$ km s^{-1}. However, this velocity range, along with the apparent sizes of the jet, may be limited by the width of the maser window of the surrounding envelope. Bright compact structures were observed in the jet itself. In the N–W part of the jet, a bright local region, an ejected blob with a velocity $v \approx 6$ km s^{-1} in the plane of the sky, was observed at a distance of 2.3 mas from the core from March 21 through August 9, 1998 (Fig. 3) (Kobayashi *et al.* 2000; Matveyenko *et al.* 2001). In December 1998, compact components were also seen in both parts of the bipolar outflow (see Fig. 3).

The Final Phase of Activity

The structure of the jet at the epoch of decline in activity (January 23–April 24, 1999) changed significantly (see Fig. 3). In January 1999, two components separated symmetrically relative to the injector by a distance of 0.8 mas in the direction $X \approx 4°$ appeared in the central part. Previously, embryos of a similar structure were observed on March 21, 1998, but its brightness was lower (Fig. 3). Changes in the orientation of the central part of the bipolar outflow, the injector axis, were also observed at the final phase of activity. The axis was oriented at an angle $\sim -37°$.

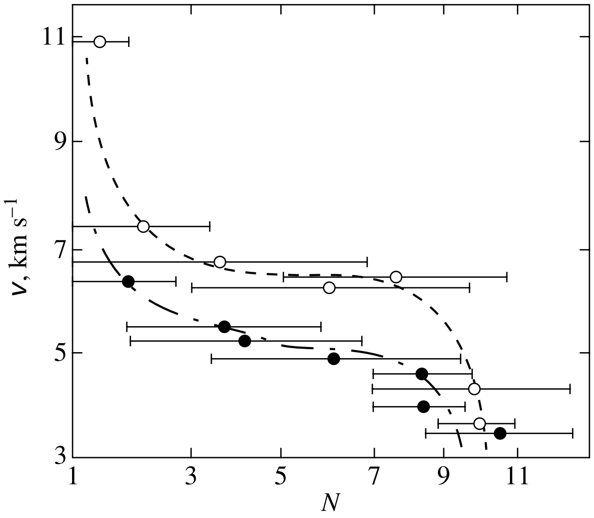

Fig. 6. Bullet velocities at various epochs of observation in the N—W (circles) and S—E (dots) parts of the outflow.

The injected flow was then transformed into the large-scale structure of the jet. The radial velocity components of the N—W and S—E parts of the jet differed from one another by $\Delta v \approx \pm 0.15$ km s^{-1}, $v_{\rm NW} \approx -0.15$ km s^{-1} and $v_{\rm SE} \approx 0.15$ km s^{-1}. The brightness temperature of the injector was $T_{\rm b} \approx 2 \times 10^{16}$ K, and its radial velocity was $v_0 \approx 7.45$ km s^{-1}.

As previously, compact structures are embedded in the outflows. The change in the positions of the components with time allows their velocities in the plane of the sky to be determined. Figure 5 shows the positions of the individual structures in the N—W and S—E parts of the outflows. The straight lines connect the positions of the individual components; their slopes correspond to the velocities of the components. The measurement accuracy and the limited visibility window of the components determined by the envelope, an active filter ($\Delta v \approx 0.5$ km s^{-1}), do not allow the possible deceleration of the components to be estimated. Generalized velocity data are shown in Fig. 6. The circles and the dots indicate the mean velocities of the individual components in the N—W and S—E parts of the bipolar outflow that correspond to the times marked by rectilinear segments. The times (session numbers) correspond to the observing sessions listed in the table. The dotted and dashed—dotted lines reflect the changes in the velocities of the components in the N—W and S—E parts of the bipolar outflow, respectively. At the beginning of the outburst, the velocities of the components rapidly decrease from 10 to 7 km s^{-1} in the N—W part of the bipolar outflow and from 8 to 6 km s^{-1} in its S—E part. Subsequently, between the third and seventh sessions, the velocities of the components decrease only slightly, $v_{\rm NW} = 6.8$ km s^{-1} and $v_{\rm SE} = 5.0$ km s^{-1}. At the decay stage of the supermaser emission, the velocities of the components decrease sharply to $\sim$3.5 km s^{-1}. The observed changes in the velocities of the components embedded in the bipolar outflows correlate with the change in outburst intensity. The higher intensity of the emission corresponds to the high velocity of the N—W outflow than that of its S—E part. The outburst is preceded by a high injection velocity, while the outburst decay is preceded by a decrease in velocity (Fig. 6). The flow injection velocity can be related to the amount of accreted matter the energy of whose torque transforms into the kinetic energy of the flow.

The velocity components in the plane of the sky significantly exceed the radial velocity components. The low radial velocity components, $v_{||} \leq 0.3$ km s^{-1}, may actually reflect the limited visibility of the maser amplifier window. The total velocity of the bipolar outflow is most likely $v \approx 10$ km s^{-1}.

The Helical Structure of the Jet

Analysis of the maps at different velocities and different times indicates that the orientation and shape of the N—W and S—E branches of the outflows change with time. These changes are determined by their helical structure. Figure 7 shows the helix constructed from the data of several sessions. The helix pitch and diameter increase with distance from the injector R, being $T = 1.3 \times R^{0.1}$ mas and $\varnothing = 0.28 + 0.08R$ mas, respectively. The orientation of the jet (helix) axis changes over the period under consideration from $X = -40°$ in March 1998 to $X = -33°$ at the end of activity (June 1999) (see the table and Fig. 3). The helix axis is more accurately determined in the central part of the jet closer to the injector. The orientation of the axis $X(t)$ as a function of time is shown in Fig. 8. The observed changes are probably determined by the precession of the injector rotation axis. The above dependence is indicated in the figure by the solid line and corresponds to

$$X = -\{30° + 16° \cos[2\pi(5.5 + t)/T]\},$$

where t is the time, in months, measured from the epoch 1998.0.

The precession period is $T = 110.4$ months. The projection of the rotation axis onto the plane of the sky is $-30°$, and the precession angle is $16°$. If the rotation axis of the system precesses, then the direction of the injected flow must also change. Our studies of the hyperfine structure of the jet at the epoch of quiescence 1995.5 show that a bright point source with a size of no larger than 0.1 mas, or 0.05 AU, is located at its center (see Fig. 3). Its brightness

Table 1. Parameters of the structure

Component	S−E	Core (jet)	N−W	Disk	Note
May 26, 1995					Jet is helical
X, deg	147	−53 (−33)	−33		
L, mas	7.5 × 1.5	0.1(0.1 × 0.8)	7.5 × 1.5		
V, km s^{-1}	7.84	7.6	7.22		
T_b, 10^{12} K	$\leq$1	9 (3)	$\leq$0.7		
No. 1. March 21, 1998					N−W part of jet—helix, $T = 6$ mas
X, deg	136	−44 (−44)	−38.5	8	
L, mas	3.5 × 0.15	0.1 × 0.9	4.2 × 0.15	0.8 × 0.1	
V, km s^{-1}	7.9	7.6	6.9	6.8	
T_b, 10^{15} K	$\leq$2	65 (10)	$\leq$2	1	
No. 2. May 22, 1998					N−W part of jet is curved. The velocities changed sign
X, deg	135	−45 (−45)	−38.5		
L, mas	3.0 × 0.15	0.1 × 1.0	4.0 × 0.15		
V, km s^{-1}	7.1	7.66	8.3		
T_b, 10^{15} K	$\leq$2	(10) 3	$\leq$2		
No. 3. June 18, 1998					Jet is straight. Components: 1.3 mas to S−E and 1.8 mas to N−W
X, deg	138	−40.5 (−40.5)	−40.5		
L, mas	2.5 × 0.1	0.1 × 1.3	4.0 × 0.1		
V, km s^{-1}	7.67	7.67	7.67		
T_b, 10^{15} K	$\leq$10	(40) 15	$\leq$10		
No. 4. August 9, 1998					Components: 2.3 mas to N−W, 1.7 mas to S−E
X, deg	141	41 (−41.5)	−41.5		
L, mas	4.0 × 0.15	0.1 × 0.9	3.5 × 0.15		
V, km s^{-1}	7.2	7.64	8.1		
T_b, 10^{15} K	$\leq$1	(12) 4	$\leq$6		
No. 5. October 14, 1998					Helical jet, $T = 3$ mas. Component: 2 mas to N−W
X, deg	144	−39.5 (−39.5)	−39.5		
L, mas	3.0 × 0.15	0.1 × 1.5	3.0 × 0.15		
V, km s^{-1}	6.6	7.65	8.5		
T_b, 10^{15} K	$\leq$0.5	(15) 4	$\leq$1.5		
No. 6. December 6, 1998					Two components in each of the N−W and S−E parts of the jet
X, deg	140	−52 (−40)	−40		
L, mas	4.0 × 0.15	0.1 × 0.8	3.0 × 0.15		
V, km s^{-1}	6.7	7.68	8.6		
T_b, 10^{15} K	$\leq$0.2	(18) 5	$\leq$0.5		

Table 1. (Contd.)

Component	S–E	Core (jet)	N–W	Disk	Note
No. 7. January 23, 1999					
X, deg	140	−54 (−40.5)	−40.5	2.0	
L, mas	4.0 × 0.5	0.1 × 0.3	5.0 × 0.5	0.8 × 0.1	
V, km s^{-1}	6.5	7.65	9.2	7.6	
T_b, 10^{15} K	≤0.8	(36) 6	≤1.5	1.5	
No. 8. March 12, 1999					Jet is helical, torus
X, deg	145	−50 (−37)	−37	3	
L, mas	2.0 × 0.5	0.1 × 0.4	3.2 × 0.5	0.8 × 0.1	
V, km s^{-1}	7.65	7.65	7.65	7.2	
T_b, 10^{15} K	≤1	(21) 3	≤1	1.0	
No. 9. March 29, 1999					Jet is helical, torus
X, deg	144	−55 (−36)	−36	3	
L, mas	2.0 × 0.5	0.1 × 0.5	3.5 × 0.5	0.8 × 0.1	
V, km s^{-1}	7.66	7.66	7.66	7.66	
T_b, 10^{15} K	≤0.6	(42) 5	≤1.2	1	
No. 10. April 24, 1999					Jet is helical, torus
X, deg	144	−62 (−36)	−36	20	
L, mas	2.0 × 0.5	0.1 × 0.5	3.0 × 0.5	1.0 × 0.2	
V, km s^{-1}	6.6	7.65	7.6	7.65	
T_b, 10^{15} K	≤0.2	(45) 6	≤0.8	0.8	
No. 11. June 12, 1999					Jet is helical, torus
X, deg	145	−63 (−35)	−35	45	
L, mas	0.8 × 0.3	0.1 × 0.3	2.0 × 0.5	0.78 × 0.2	
V, km s^{-1}	7.9	7.67	7.7	7.0	
T_b, 10^{15} K	≤0.6	(4.8) 0.6	≤0.8	0.2	
No. 12. August 11, 1999					Jet is helical, torus
X, deg	147.5	68 (−32.5)	−32.5	54	
L, mas	0.7	0.1	2.0 × 0.5	2.3 × 1.2	
V, km s^{-1}	8.1	7.6	7.2	7.3	
T_b, 10^{15} K	≤0.04	(1.3) 0.3	≤0.2	≤0.8	

temperature is $T_b \cong 10^{13}$ K. This point source lies in the central part of a thin, elongated component with sizes of 0.8 × 0.1 mas, or 0.4 × 0.05 AU. This component corresponds to the injected bipolar flow in the immediate vicinity of the nozzle (injector). Its brightness temperature is $T_b = 9 \times 10^{12}$ K. The component is oriented at an angle $X = -53°$. The distant ends of the component gradually turn around as one recedes from the injector and approaches the jet axis $X = -33°$. The high brightness temperature of the core and the structure of the elongated component suggest that the point source is the injector of the bipolar particle flow, while the thin elongated component is the particle flow itself, which also includes

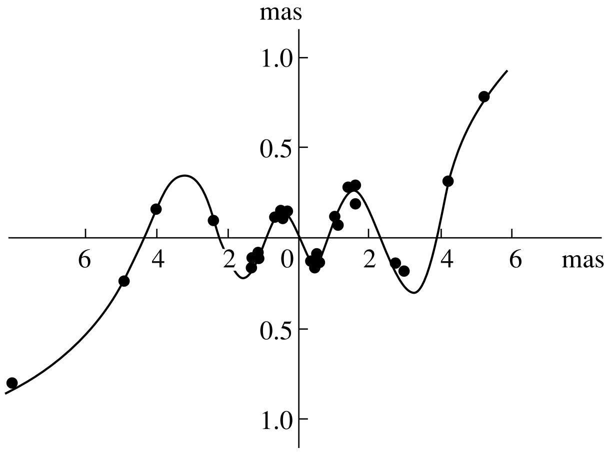

Fig. 7. Structure of the bipolar outflow.

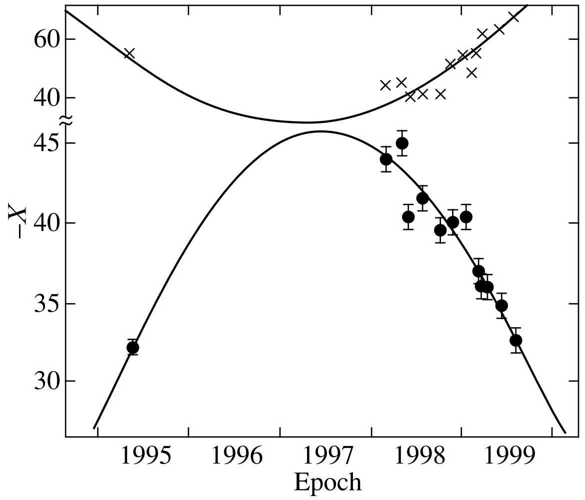

Fig. 8. Changes in the orientations of the jet (lower curve) and injector (upper curve) axes.

water-vapor molecules. We are observing their maser emission. The velocity of the injector in the local frame of reference is $v = 7.65$ km s^{-1}.

During the period of enhanced maser activity, the brightness temperature of the core (injector) rose by more than four orders of magnitude, $T_b = (1–7) \times 10^{16}$ K. However, its size did not change and was no larger than 0.1 mas, or 0.045 AU. The sizes of the thin elongated jet were 0.05×0.5 AU, and its brightness temperature was $T_b \approx 10^{16}$ K.

The orientation of the injector axis changes with time, which may be due to the precession of the rotation axis of the system (see the table). The crosses in the upper part of Fig. 8 indicate changes in the orientation of the axis with time. The observed change was virtually out of phase with the change in the position of the outflow (jet), being

$$X = -\{63^\circ + 33^\circ \cos[2\pi(45.7 - t)/T]\}.$$

The projection of the rotation axis onto the plane of the sky is -63°, and the precession angle is 33°. Thus, the precession of the jet axis lags behind by $\sim$40 months, and its precession angle is half the precession angle of the injector.

The observed peculiarities of the jet structure — the high flow collimation, $\sim$30 (1.5×0.05 AU); the helical structure with an increasing pitch; and the precession lag—are determined by the focusing action of the magnetic field and its viscosity.

The orientation of the injector axis must determine the direction of motion of the bullets. Indeed, they lie within the following angles: $X = -37^\circ \pm 5^\circ$ and $X = 138^\circ \pm 5^\circ$ (Fig. 9). Various shapes and orientations of the bullets are observed. In March 1998, the bullet nearest the injector had an elongated comet-shaped structure with sizes of 0.5×3.5 mas, or 0.25×1.7 AU, and oriented at an angle $X = -50^\circ$; its tail was behind the head. The brightness temperature of the head was $T_{\text{peak}} = 4 \times 10^{15}$ K. The distant bullet with sizes of 0.25×5 AU and $T_{\text{peak}} = 4 \times 10^{14}$ K had a similar comet-shaped structure with a trailing tail. However, in May 1995, during the period of low activity, the bullet tail was in front of the head, suggesting that the bullet velocity was relatively low. Light pressure and stellar wind blow the bullet tail forward.

The Toroidal Structure

As we see from Fig. 3, on March 21, 1998, a weak elongated component with sizes of 0.8×0.1 mas oriented at an angle $X = 8^\circ$ and with bright compact regions at the edges appeared in the injector region. The brightness temperatures of the extended component and the compact components were $T_b = 7 \times 10^{12}$ K and $T_b = 4 \times 10^{13}$ K, respectively. The injector axis was almost perpendicular to the major axis of the structure under consideration, the disk plane. This structure was again visible on January 23, 1999, and was preserved until March 29, 1999 (Fig. 3). As previously, its sizes did not change, being 0.8×0.1 mas, and its position angle was $X = 2^\circ$. In April 24, 1999, it was seen more clearly, and its sizes were 1×0.2 mas, but its position angle changed to $X = 21^\circ$. In June–August 1999, components that complemented the toroidal structure (disk) observed at an angle appeared in the central region. The sizes of the torus are 2.4×1.6 mas, and its thickness is $\sim$0.3 mas. The major axis of the torus is oriented at an angle of about 90° relative to the injector axis. Based on the ratio of the major and minor axes of the structure, we obtain a disk inclination of $\sim 50^\circ$.

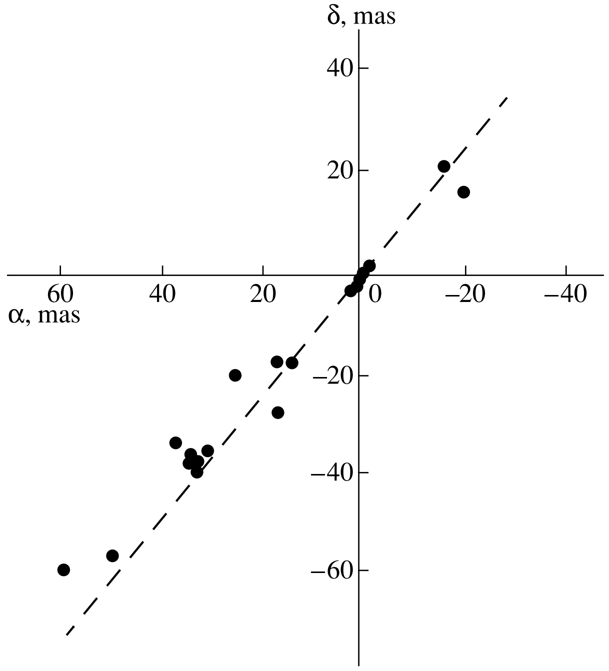

Fig. 9. Positions of the bullets.

The radial velocity of the disk is $v \approx 7.1$ km s^{-1} and lies outside the maser amplification window in the envelope. The brightnesses of the components at its edges are determined by the larger optical depth—the tangential directions of the disk. The highest brightness temperatures of the individual components in the N–W and S–E parts of the disk are $T_b \approx 5 \times 10^{13}$ K and $T_b \approx 10^{12}$ K, respectively. The changes in the visible structure probably result from the precession of the torus (disk) observed at different angles.

The Core Emission Line Profile

As follows from the observational data, the injector region corresponds to the bright compact source with sizes ≤ 0.1 mas, or ≤ 0.045 AU, and the thin elongated component—the injected flow with sizes of its bright part 0.05×0.2 AU. The emission from this structure is concentrated in a narrow spectral line with broad wings. The line velocity is $v = 7.65$ km s^{-1}. The line spectrum may be represented as two Gaussians with intensities $I_1 = 3 \times 10^5$ Jy/beam and $I_2 = 400$ Jy/beam and FWHMs $\Delta v_1 = 0.42$ km s^{-1} and $\Delta v_2 = 2.2$ km s^{-1}, respectively. The apparent brightness temperatures of the injector and the injected flow itself are $T_b \approx 5 \times 10^{16}$ K and $T_b \approx 10^{14}$ K, respectively. The broad spectral line is probably determined by the maser emission from the stream of water-vapor molecules immediately at the injector exit. This emission is amplified by the external medium (envelope) with a radial velocity $v = 7.65$ km s^{-1}. Thus, we are observing the amplified emission from the injector region. It follows from the ratio of the Gaussian amplitudes that the maser amplification in the envelope is $G \approx 750$. The high brightness temperature and the Gaussian profile of the observed emission from the central region suggest that the maser amplifier is not saturated.

The observed broad maser line profile can be explained by the peculiarities of the emission source itself. The bipolar flow is injected along the rotation axis of the accretion disk (injector), which leads to the rotation of the particle flow. In the case of a stationary velocity of the injected matter and its low temperature, the width of the line profile is determined by the rotation velocity of the flow itself: $\Delta v_{||} \approx 2v_{\rm rot}$. For a radius of the flow cross section $R \approx 0.02$ AU and observations at a mean angle, $v_{\rm rot} \approx 1.1$ km s^{-1}; this value corresponds to a rotation period $T \approx 5$ months. Thus, the rotation velocity of the flow is a factor of $\sim$20 higher than the precession velocity of the injector rotation axis (110 months).

INTERPRETATION OF THE OBSERVATIONAL DATA

The active region under consideration is located in the core of the dense molecular cloud OMC-1 in the Orion Nebula. As follows from our studies of the hyperfine structure of the active region in the maser emission line, the formation of a star is associated with the formation of an accretion disk, with the bipolar outflow of matter, and with the ejection of bullets—compact ice blobs. This structure is surrounded by an envelope containing water molecules. The star formation is accompanied by intense maser emission in water-vapor lines. We observed two epochs of high activity—supermaser emission. In the first period of activity, 1979–1988, the H_2O-maser emission originated from the accretion disk at the stage of its separation into groups of concentric rings; in the second period of activity, 1998–1999, it originated from the toroid—the thick disk, the bipolar outflow, and the bullets. The environment (envelope) amplified the emission from the components with radial velocities equal to its velocity by more than two orders of magnitude. The envelope velocity was $v \approx 7.56$ km s^{-1}, and the width of the maser window was $\Delta v \approx 0.5$ km s^{-1}.

The sublimation of water molecules and their acceleration by radiation pressure form a halo, a maser ring emitting in the azimuthal plane, around the rings. For a nonuniform distribution of water molecules in the maser ring, the emission is nonuniform and leads to the observation of rapid variability determined by the rotation velocity of the ring and the gradient in the distribution of water molecules. The disk precession and the envelope amplification determine the activity (the visibility of this emission) and the supermaser emission, respectively. The constancy of the velocity of the supermaser emission during the entire period of observations is related to the amplification by the envelope with a constant velocity. Thus, the precession of the accretion disk and the fact that the velocities of the emitting structures are equal to the envelope velocity act as a trigger of activity. The nonuniform injection of matter and the narrow maser amplifier window, which limits the visibility of the structure as a whole over the entire velocity range, have a certain effect on the manifestation of activity. The diameter of the accretion disk is ∼33 AU, and the mass of the central body lies within the range 0.2–$0.5M_\odot$. The emission from the rings was amplified in the surrounding envelope at a velocity of $v = 7.65$ km s^{-1} in the maser window band $\Delta v = 0.5$ km s^{-1}.

At the second epoch of activity, a torus 1.2 AU in diameter and ∼0.15 AU in thickness can be identified in the central part. The plane of the torus is perpendicular to the injector axis. Since the radial velocity of the torus, $v \approx 7.1$ km s^{-1}, lies outside the maser amplifier window in the envelope, its brightness is low. The structure of the star-forming region changed significantly over several months. This change resulted from the precession of the injector rotation axis. The precession period is ∼10 yr, and the rotation period of the axis is ∼0.5 yr. The precession angle of the injected flow immediately at the exit from the nozzle is ∼33° and decreases by a factor of 2 at a distance of ∼1 AU. The rotation is delayed in phase by ∼3.3 yr.

The structure that we detected in the H_2O-supermaser emission lines is characteristic of the initial formation phase of a low-mass protostar: class "0". Note, for comparison, that the similar structure observed in the nearby active zone in Orion KL has the mass of the central body $\sim 0.01M_\odot$ (Matveyenko *et al.* 2000). The objects of this class are located in dense molecular clouds and are observed as submillimeter sources. In Orion KL, the infrared spectrum revealed clusters of planetary-mass objects and brown dwarfs with masses of 0.008–$0.10M_\odot$ (Lucas and Roshe 2000). As follows from the most recent improved data, the central object of the structure under consideration may be the infrared source IRc-4 (Gaume *et al.* 1998). Bipolar outflows of molecular gas accompany the formation of low-mass stars. They carry away the angular momentum of the accreting cloud, thereby favoring the subsequent contraction of matter. The disk can be surrounded by an extended envelope with the size reaching 100 AU, and its mass lies within the range 0.01–$1M_\odot$; the mass of the surrounding gas exceeds the stellar mass. The matter of the environment is accreted onto the disk in the azimuthal plane and is ejected along its rotation axis. The disk energy transforms into bipolar outflows. The interaction of the outflow with the environment leads to the formation of a nozzle (injector). The pressure of the environment focuses the outflow (Bachiller 1996). The magnetic field determines the initial anisotropy and orientation of the protostellar disk and the jet. The accretion and injection of matter are two independent, but complementary processes. Stellar wind is ejected by the poloidal magnetic field as if from a centrifuge (Lovelace *et al.* 1991, 1993).

As follows from our data, the bipolar outflows are highly collimated. The ratio of the apparent size of the bipolar outflow (∼3 AU) to its diameter (∼0.05 AU) reaches ∼60. The observed maser emission corresponds to a neutral outflow of matter containing water-vapor molecules. These peculiarities suggest the presence of free electrons and a magnetic field that form a twisted bipolar outflow in the shape of a conical helix with a variable pitch. A small number of free electrons affect the neutral component, forming highly collimated bipolar outflows. The presence of a small number of such electrons (the degree of ionization is $\sim 10^{-6}$–10^{-5}) is also required for an effective operation of the collisional pumping (Strelnitskij 1984).

The maser emission is observed immediately at the exit of the injector itself in the form of a bright ($T_b \approx 10^{14}$ K), compact (<0.05 AU) source. This is also suggested by the absence of a bright head in the jet, which must be present when the water-vapor molecules distributed in the environment are excited. The intensity of the maser emission from the outflow decreases with increasing distance from the injector.

We also see the emission from individual ejections—the bullets and compact structures moving inside the outflow itself. The bullets exhibit a head that may be associated with a dense structure composed of ice particles with carbon nuclei. Their interaction with the environment leads to the formation of comet-shaped structures. Depending on the bullet velocity and the acceleration of sublimated water-vapor molecules by radiation pressure and stellar wind, the tail can be behind and in front of the head. The ejections of bullets are observed within an angle of ∼10°, which is determined by the precession of the injector rotation axis. The bullets are made up of neutral material with embedded particles in the form of carbon nuclei in an ice envelope and moving rectilinearly in the direction determined by the location of the injector rotation axis.

The interaction of the particle flow with the environment causes collisional maser pumping. The velocity of the visible part of the flow is $v \approx 10$ km s^{-1}, and the bullet velocity exceeds it. The highly collimated flow hydrodynamically interacts with the environment to form a thin transition layer (Bachil-

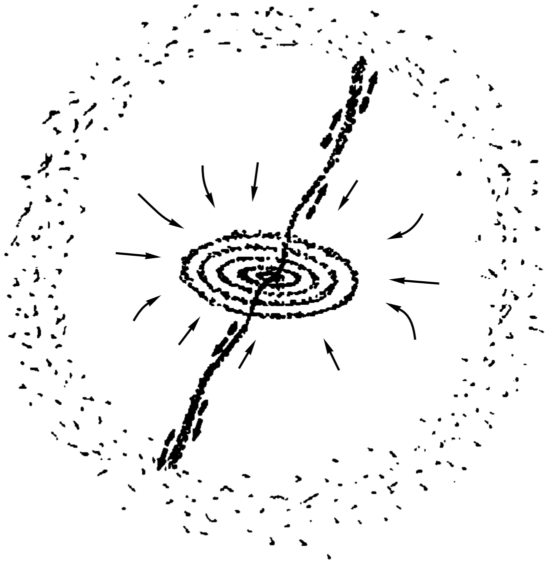

Fig. 10. Schematic structure of the active region: the torus, accretion disk the bipolar outflow of particles and envelope.

ler 1996). The maser emission may originate from this layer. Several percent of the kinetic energy of the particle flow converts into infrared pumping radiation at a wavelength of $\sim 40\ \mu$m. The kinetic energy of a typical blob with a size of $\sim 10^{14}$ cm and a hydrogen density of $\sim 10^8$ cm^{-3} moving at a velocity of 10–40 km s^{-1} is high enough to excite high-power masers, but not supermasers (Reid and Moran 1988). The kinetic energy of the particle flow can be partly increased by increasing the hydrogen density. The limiting hydrogen density does not exceed 10^{11} cm^{-3} because of rapid cooling. However, a mixture of free electrons and neutral particles can significantly exceed this limit. The pumping will be at a maximum for an ionization of $\sim 10^{-5}$ (Strelnitskij 1984). In our case, the supermaser emission can be more easily explained by the amplification of the envelope emission by more than two orders of magnitude.

The intense infrared source IRc-4 is located at the center of the active zone, while the clusters of infrared sources with a total flux at 40 μm of $F \approx 50$ kJy are concentrated in the core of the molecular cloud OMC-1 (Goudis 1982). This emission excites the water-vapor molecules of the accretion disk and the environment. It is beamed with respect to the maser rings, which explains its high degree of polarization. This source produces the pumping for the envelope that amplifies the maser emission by three orders of magnitude at a velocity of 7.56 km s^{-1}. This amplifier is responsible for the conservation of the velocity of supermaser outbursts at different epochs.

The observed emission had a high degree of linear polarization. The polarization of the emission was determined by the directed pumping relative to the maser. For the supermaser emission with $F \approx 4$ MJy, the polarization reached $P \approx 70\%$, and its position angle was $X \approx -22°$. As the emission passes through the H II region, the Faraday rotation changes significantly, and corresponds to $-5 < X < -1$ rad at a wavelength of 1.35 cm. However, the rotation angle of the polarization plane on the time scale under consideration probably does not change (Matveyenko 1994). The degree of polarization can increase significantly as the emission passes through the amplifying envelope, as follows from the papers by Varshalovich (1970) and Western and Watson (1983, 1984).

At the epoch of quiescence, the emission $F \approx 10^3$ Jy, $v \approx 7.9$ km s^{-1} was determined by the bipolar outflow; the degree of polarization is $P \approx 33\%$ and $X \approx -47°$ (Matveyenko *et al.* 1998). In the second period of activity, 1998–1999, the emission was determined, as in the period of quiescence, by the bipolar outflow of particles, but the relative contribution of the injector emission increased. As previously, the polarization of the emission and its orientation are related to directed pumping—the directed flow of particles.

There is a certain correlation of the polarization parameters with the flux density: $F = 2.4$ MJy, $P = 46\%$, and $X \approx 26°$; $F \approx 1.2$ MJy, $P = 38\%$, and $X = 30°$; $F \approx 0.5$ MJy, $P = 34\%$, and $X = 40°$; $F = 49$ kJy, $P = 29\%$, and $X = 42°$ (Horiuchi and Kameya 2000). The polarization P and its orientation X within the period under consideration depend on the flux density of the emission and may be represented as follows: $P = 30 + 6.4F$ [%] and $X = 42–6.9F$ [deg]. In reality, this dependence is more complex and is determined by the vector sum of the polarization parameters for the components. The observed radio flux density $F = GF_0$ equally depends on the amplification G in the envelope and the original emission. Thus, the observed effect is determined by the activity of the star-formation process: the number of excited water-vapor molecules, i.e., the pumping, and the number of H_2O molecules, as well as the magnetic field of the envelope.

The maser mechanism is the stimulated amplification of the transmitted radiation through the induced emission of resonance photons by excited molecules of the environment. Thus, the emission is coherently amplified (Matveyenko *et al.* 1980; Moran 1989). The brightness temperature of the compact source (injector) is high, $T_b \approx 10^{14}$ K, and the apparent temperature is $T_b \approx 10^{16}$ K. Its angular size does not exceed 0.1 mas, or 0.05 AU. The sizes of the coherent radiation area are determined by the geometric phase shift at its edges, $2\pi L/\lambda(1-\cos\alpha)=\pi/4$. At a distance to the Orion Nebula of $L=1.5\times10^{21}$ cm, the angle $\alpha=1.5\times10^{-11}$ rad and the sizes of the coherent area are $\varnothing=2\times10^{10}$ cm. Phase shifts related to small-scale inhomogeneities both in the nebula itself (H II region) and in the interstellar medium can arise within such a large aperture. However, this does not rule out the possibility that the coherent radiation is preserved within small areas determined by the inhomogeneity sizes and the characteristic time scale. In this case, the maser emission source consists of a cluster of point sources twinkling like sparklers. This twinkling may be observed when mapping maser sources.

CONCLUSIONS

Our studies of one of the most active star-forming regions located in the core of the dense molecular cloud OMC-1 (Orion KL) with a very high resolution (0.045 AU) have revealed the following:

—A structure that includes an accretion disk, a bipolar outflow, and an envelope (see Fig. 10) is formed at the early formation stage of a low-mass star.

—The process is accompanied by intense maser emission in water-vapor lines. H_2O-supermaser outbursts are occasionally observed.

—The accretion disk 0.05 AU in thickness is at the stage of its separation into groups of concentric protoplanetary rings. The diameter of the outer ring reaches 32 AU. A toroidal structure 1.1 AU in diameter and 0.15 AU in thickness is located in the central part. The mass of the central object is $\sim0.1-0.5M_\odot$. The rotational velocity of the rings is determined by Keplerian motion. The expansion of the maser rings is the radial acceleration of water-vapor molecules by radiation pressure.

—The accretion and injection of matter are a unified process. The injected neutral material contains H_2O molecules, including those in the form of carbon grains in the ice envelope. The size of the injector (nozzle) does not exceed 0.05 AU; it is observed in the form of a bright compact maser source with $T_b\approx10^{17}$ K. The injected flow of neutral matter with embedded H_2O molecules and free electrons is collimated into a thin jet with $T_b<10^{14}$ K. The collimation reaches 60, and the flow velocity is $\sim$10 km s^{-1}.

—The rotation of the disk (nozzle) twists the injected flow with a rotation velocity of $\sim$1.1 km s^{-1}. The precession period of the rotation axis reaches $\sim$10 yr and is a factor of 20 longer than the rotation period of the flow. The precession and the magnetic field form a flow structure similar to a conical helix with a variable pitch.

—The spectral profile of the maser emission line immediately at the exit of the injector has a width of $\Delta v=2.2$ km s^{-1}, $v=7.65$ km s^{-1}. This emission is amplified in the envelope by approximately three orders of magnitude within the maser window.

—Ejections of dense compact structures (bullets) are observed. The ejection angle corresponds to a precession angle of $\sim$10°.

—The kinetic energy of the flow and the bullets transforms into the directed, collisional pumping of maser emission, which is responsible for the high linear polarization of the maser emission.

—The object IRc-4, a source of directed radiation pumping with respect to the protoplanetary rings, is probably located at the center of the system. This explains the high linear polarization of the maser emission, which increases as the latter passes through the maser environment of the envelope.

—The envelope amplifies the radio emission from the structures at a velocity of $v=7.65$ km s^{-1} in a maser window band of $\Delta v=0.5$ km s^{-1} by approximately three orders of magnitude. This amplification is responsible for the supermaser emission from the active region and for the conservation of its velocity.

—The emission from the rings is concentrated in the azimuthal plane. The nonuniform distribution of water molecules in the maser ring leads to nonuniform emission and to the observed variability as it rotates. The precession of the ring limits its visibility.

Thus, this unique case of H_2O-supermaser outbursts confirms that particularly active star formation takes place during the formation of young low-mass objects in molecular clouds.

ACKNOWLEDGMENTS

L.I. Matveyenko wishes to thank MPIFR and NRAO for their support and hospitality. The studies were supported by the Russian Foundation for Basic Research (project no. 02-02-16179), the Ministry of Science of Russia, and the Nonstationary Objects Program of the Russian Academy of Sciences.

REFERENCES

1. Z. Abraham, N. L. Cohen, R. Opher, *et al.*, Astron. Astrophys. **100**, L10 (1981).
2. Z. Abraham, J. W. S. Vilas Boas, and L. F. Giampo, Astron. Astrophys. **167**, 311 (1986).
3. V. A. Ambartsumyan, *Proc. of 2nd Meeting on Cosmogony Problems* (Akad. Nauk SSSR, Moscow, 1953), p. 9 [in Russian].
4. V. A. Ambartsumjan, Ann. Rev. Astron. Astrophys. **18**, 1 (1980).
5. R. Bachiller, Ann. Rev. Astron. Astrophys. **207**, 339 (1984).

6. R. Bachiller, Ann. Rev. Astron. Astrophys. **34**, 111 (1996).
7. B. F. Burke, K. J. Johnston, V. A. Efanov, *et al.,* Astron. Zh. **49**, 465 (1972) [Sov. Astron. **16**, 379 (1972)].
8. B. F. Burke, K. J. Johnston, V. A. Efanov, *et al.,* Radiofizika **5**, 799 (1973).
9. G. Garay, J. M. Moran, and A. D. Hashick, Astrophys. J. **338**, 244 (1989).
10. R. A. Gaume, J. M. Wilson, R. J. Vrba, and K. J. Jonston, Astron. Astrophys. **493**, 940 (1998).
11. R. Genzel, D. Downes, J. M. Moran, *et al.*, Astron. Astrophys. **66**, 13 (1978).
12. G. Goudis, *The Orion Complex: A Case Study of Interstellar Matter* (Astrophys. Space Sci. Lib., 1982), Vol. 90.
13. L. J. Greenhill, C. R. Gwinn, *et al.*, Nature **396**, 650 (1998).
14. S. Horiuchi and O. Kameya, Preprint No. 4 (Mizusawa Astrogeodynamics Observ., 2000).
15. H. Kobayashi, T. Shimoikura, T. Omodaka, and P. J. Diamond, *Proc. of the VSOP Symp., Inst. of Space Astronautical Sci., 2000*, Ed. by H. Hirabashi, P. G. Edwards, and D. W. Murphy, p. 109.
16. M. M. Litvak, Science **165**, 855 (1969).
17. R. V. E. Lovelace, H. L. Berk, and J. Contopoulos, Astrophys. J. **379**, 696 (1991).
18. R. V. E. Lovelace, M. M. Romanova, and J. Contopoulos, Astrophys. J. **403**, 158 (1993).
19. R. W. Lucas and P. F. Roshe, Mon. Not. R. Astron. Soc. **314**, 858 (2000).
20. L. I. Matveyenko, Pis'ma Astron. Zh. **7**, 100 (1981) [Sov. Astron. Lett. **7**, 54 (1981)].
21. L. I. Matveyenko, Pis'ma Astron. Zh. **20**, 456 (1994) [Astron. Lett. **20**, 388 (1994)].
22. L. I. Matveyenko, L. R. Kogan, and V. I. Kostenko, Pis'ma Astron. Zh. **6**, 505 (1980) [Sov. Astron. Lett. **6**, 279 (1980)].
23. L. I. Matveyenko, D. M. Moran, and R. Genzel, Pis'ma Astron. Zh. **8**, 711 (1982) [Sov. Astron. Lett. **8**, 382 (1982)].
24. L. I. Matveyenko, D. A. Graham, and P. J. Diamond, Pis'ma Astron. Zh. **14**, 1101 (1988) [Sov. Astron. Lett. **14**, 468 (1988)].
25. L. I. Matveyenko, P. J. Diamond, D. A. Graham, and W. Junor, in *Proceedings of Conference on Astrophysical Masers, Arlington, Virginia, USA*, Ed. by A. W. Clegg and G. Enedoluha (Springer-Verlag, 1992), p. 176.
26. L. I. Matveyenko, P. J. Diamond, and D. A. Graham, Pis'ma Astron. Zh. **24**, 723 (1998) [Astron. Lett. **24**, 623 (1998)].
27. L. I. Matveyenko, P. J. Diamond, and D. A. Graham, Astron. Zh. **77**, 869 (2000) [Astron. Rep. **44**, 592 (2000)].
28. L. I. Matveyenko, P. J. Diamond, and D. A. Graham, *IAU Coll. 205: Cosmic Masers: From Protostars to Blackholes,* Ed. by V. Migenes and M. J. Reid (2001), p. 96.
29. J. M. Moran, *Molecular Astrophysics,* Ed. by T. Hartquist (Cambridge Univ. Press, 1989).
30. T. Omodaka, T. Maeda, M. Miyoshi, *et al.*, Publ. Astron. Soc. Jpn. **51**, 333 (1999).
31. M. J. Reid and J. M. Moran, *Galactic and Extra Galactic Radioastronomy,* Ed. by G. K. Verschuur and K. I. Kellermann (Springer-Verlag, 1988), p. 255.
32. I. S. Shklovsky, Astron. Tsirk, No. 372, 1 (1967).
33. V. S. Strelnitskij, Usp. Fiz. Nauk **113**, 463 (1974).
34. V. S. Strelnitskij, Mon. Not. R. Astron. Soc. **207**, 339 (1984).
35. A. M. Tolmachev, Pis'ma Astron. Zh. **26**, 41 (2000) [Astron. Lett. **26**, 34 (2000)].
36. B. E. Turner, *Galactic and Extragalactic Radio Astronomy,* Ed. by G. K. Verschuur and K. I. Kellermann (Springer-Verlag, 1988).
37. D. A. Varshalovich, Usp. Fiz. Nauk **101**, 369 (1970).
38. L. R. Western and W. D. Watson, Astrophys. J. **275**, 195 (1983).
39. L. R. Western and W. D. Watson, Astrophys. J. **285**, 158 (1984).

Translated by V. Astakhov

Astronomy Letters, Vol. 30, No. 2, 2004, pp. 117–123. Translated from Pis'ma v Astronomicheskiĭ Zhurnal, Vol. 30, No. 2, 2004, pp. 139–145.
Original Russian Text Copyright © 2004 by Arkhipova, Ikonnikova.

Pre- and Post-Outburst Parameters for the Components of the Symbiotic Star V1329 Cyg

V. P. Arkhipova[*] **and N. P. Ikonnikova**

Sternberg Astronomical Institute, Universitetskii pr. 13, Moscow, 119992 Russia

Received October 21, 2002; in final form, September 18, 2003

Abstract—We present new UBV observations of the symbiotic nova V1329 Cyg. Based on all our UBV observations of a uniform system, we redetermined the orbital period of the binary and estimated the magnitudes and luminosities of its components. We show that the pre-outburst visual luminosities of the red giant and the hot star were almost equal and that the rapid irregular photographic variability of the star was caused by the nonstationary behavior of the hot component. The outburst amplitude of the hot component (subdwarf) in 1964 was found to be $\sim 2^m$ in the V band, which is typical of ordinary symbiotic stars. We estimated the continuum luminosity of the gaseous component that appeared after the outburst. In the V band, it was almost 1^m fainter than the flared hot star. Structurally, the gaseous component is an ionized gaseous disk comparable in size to an M giant.

Key words: *symbiotic stars, photometry, component parameters, V1329 Cyg.*

INTRODUCTION

Despite the numerous studies of HBV 475 = V1329 Cyg ($\alpha = 20^{\mathrm{h}}51\overset{\mathrm{m}}{.}0$, $\delta = +35°35'$, 2000), a symbiotic star with the only novalike outburst that began in 1964, the parameters of its binary components are still highly uncertain. Grygar *et al.* (1979) and Iijima *et al.* (1981) derived the mass function of the binary, $f_{\mathrm{hot}}(M) = 23M_{\odot}$, from the radial velocities of emission lines, which suggested the presence of a high-mass component. Based on ultraviolet spectra, Nussbaumer *et al.* (1981) also obtained $f_{\mathrm{hot}}(M) = 22M_{\odot}$. However, Baratta and Viotti (1990) showed that, in general, the emission lines did not represent the orbital motion of the hot binary component. Ikeda and Tamura (2000) obtained a new value of the mass function for the components, $f_{\mathrm{hot}}(M) = M^3_{\mathrm{cool}} \sin^3 i/(M_{\mathrm{cool}} + M_{\mathrm{hot}})^2 = 1.2M_{\odot}$, and masses of $0.65M_{\odot}$ and $2.1M_{\odot}$ for the hot and cool components, respectively, from features in the profiles of the Hα, λ4686 HeII, and λ5007 [OIII] emission lines. Based on spectroscopic observations of the red giant, Fekel *et al.* (2001) determined the mass function, $f_{\mathrm{cool}}(M) = 0.0481$, and the masses of the components, $0.75M_{\odot}$ and $2.2M_{\odot}$, respectively, from the radial velocities. The latter studies probably yielded the most reliable mass estimates for the binary components, and we use these values below.

As regards the luminosities of the components, there have been no luminosity estimates for the hot star before and after its outburst until now.

The mass of the hot component in the binary V1329 Cyg is near the upper mass limit for the central stars of planetary nebulae. Its luminosity is of interest from the viewpoint of the theory of late stellar evolution.

We decided to use our long-term photometric observations to estimate the magnitudes and luminosities of the components of the binary V1329 Cyg before and after its outburst. Particular attention was given to the gaseous and hot components of the binary.

THE COOL COMPONENT IN THE BINARY V1329 Cyg AND THE PRE-OUTBURST LUMINOSITY OF THE HOT COMPONENT

Before its outburst, several eclipses were observed in the binary V1329 Cyg. According to the numerous photographic observations of the star from 1891 until 1965, its phase light curve was Algol-like (Stienon *et al.* 1974; Grygar *et al.* 1979; Munari *et al.* 1988; Arkhipova and Mandel 1991). The orbital period was estimated by different authors to be 950–960 days. The mean brightness between eclipses was $m_{\mathrm{pg}} = 15^m$, with large fluctuations, while at minimum the star faded to $\geq 17^m$. The brightness fluctuations outside eclipses were attributable to the nonstationary

---

[*] E-mail: `vera@sai.msu.ru`

Table 1. HK observations of V1329 Cyg

Author	H(red)	K(red)
Taranova and Yudin (1986)	7.50 ± 0.15	6.93
Allen and Glass (1974)	7.43	6.85
Tamura (1983)	7.33	6.83
Kenyon (1988)	7.33	6.87

behavior of the hot component, so before the outburst it was an irregular variable with an amplitude of the photographic brightness variations up to 2^m.

Infrared JHK observations of V1329 Cyg allowed the brightness and color indices of the cool component to be estimated. The J-band data of different authors show a large scatter, and the cause of this scatter is unclear. The red component is most likely a constant star, and the discrepancy between the J magnitude estimates may be due to instrumental effects.

The discrepancy between the H and K magnitude estimates by different authors is much smaller. Table 1 gives the H and K magnitudes by different authors. We took $H(\text{cool}) = 7\overset{m}{.}40 \pm 0.1$, $K(\text{cool}) = 6\overset{m}{.}87 \pm 0.03$, $H - K = 0.53$.

The spectral type of the cool component was estimated by Rudy *et al.* (1999) as M5.5 III. According to Nussbaumer and Schmutz (1983) and Mueller *et al.* (1986), the mean color excess of V1329 Cyg is $E(B-V) = 0.53$ and $A(V) = 3.1E(B-V) = 1.64$. Taking the interstellar extinction law in the range $\lambda\lambda 6600$ Å—5 μm in the form $(\lambda) \propto \lambda^{-1.85}$ (Landini *et al.* 1984), we obtain $A(H) = 0.34$, $A(K) = 0.19$, $E(V-H) = 1.30$, $E(V-K) = 1.45$. Hence we derive the V magnitude of the M-type component: since, according to Straizys (1977), $(V-H)_0 = 6.39$ and $V-H = 7.69$ for M5.5 III, we find that $V(\text{cool}) = 15\overset{m}{.}09$. The estimate calculated from the K magnitude in a similar way is $V(\text{cool}) = 15\overset{m}{.}02$.

Thus, the red giant in the binary V1329 Cyg has $V(\text{cool}) = 15\overset{m}{.}05$, and its photographic magnitude is $m_{\text{pg}}(\text{cool}) = 17\overset{m}{.}1$, in good agreement with the available data obtained during eclipses. Before the outburst, the photographic brightness of the binary was mainly determined by its hot component.

If we assume the distance to V1329 Cyg in accordance with the luminosity of an M5.5 III giant, $M_V = 0\overset{m}{.}0$, it will be $d = 4800$ pc, in agreement with the estimate $d = 5500$ pc obtained by Rudy *et al.* (1999) from the J magnitude. We can then estimate the mean pre-outburst magnitude of the hot component by using the phase light curve of the binary outside eclipses. The mean photographic magnitude of the hot star was $m_{\text{pg}}(\text{hot}) = 15\overset{m}{.}15$. Assuming that the pre-outburst temperature of the hot component, as for other symbiotic novae, was $T(\text{hot}) > 20\,000$ K, its V magnitude is $V(\text{hot}) \approx 14\overset{m}{.}9$. At a distance of 4800 pc, the mean absolute visual pre-outburst magnitude of the hot star was $M_V(\text{hot}) \approx -0\overset{m}{.}1$. This star is still far from being a white dwarf; its luminosity suggests that it belongs to hot subdwarfs.

The semimajor axis of the orbit of V1329 Cyg for the period $P = 2.64$ years is $a = 2.35$, AU $= 593R_\odot$.

Assuming the effective temperature $T(\text{cool}) = 3500$ K and $\Delta M_{\text{bol}} = -3.0$ (Flower 1996) for M5.5 III, we obtain $M_{\text{bol}}(\text{cool}) = -3.^m1$, $(\log L/L_\odot = 3.12)$ and the radius of the giant is $R(\text{cool}) \cong 100R_\odot$. The cool component does not fill its Roche lobe, whose size is $140R_\odot$ at its mass of $2.1M_\odot$, and matter is transferred from it to the subdwarf through stellar wind.

THE POST-OUTBURST LUMINOSITIES OF THE COMPONENTS OF V1329 Cyg

Our long-term UBV observations of V1329 Cyg allowed us to study the brightness variations in the star after its 1964 outburst and the changes in its phase light curves (Arkhipova and Mandel 1973; Arkhipova 1977; Arkhipova and Belyakina 1984; Arkhipova and Ikonnikova 1989; Chochol *et al.* 1999). Table 2 gives our new observations of the star performed during the period 1998–2002 in the same photometric system as previously. We obtained 44 magnitude estimates for V1329 Cyg with a UBV photometer attached to a 60-cm reflector at the Crimean Station of the Sternberg Astronomical Institute. The accuracy of these observations was $\sim 0\overset{m}{.}02$ in the B and V bands and $\sim 0\overset{m}{.}03$ in the U band. The orbital period has repeatedly been sought from our photometric observations (Grygar *et al.* 1979; Schild and Schmid 1997; Chochol *et al.* 1999). We used the new observations to redetermine the light elements of the binary. After 1973, the star exhibited a small decrease in mean brightness in all the UBV bands; we removed this trend when searching for the period and constructing the phase light curves. The light elements were found from all our B-band observations ($N = 343$) to be

$$\text{JD(min)} = 2442005.4 + 954.5(\pm 7.4)E.$$

A characteristic feature of the phase light curves is the change in their shape after the outburst. The V and B curves were almost sinusoidal; the U phase curve was dome-shaped (Fig. 1), showing a significant duration of the eclipse when the M component was in front of the hot component. This implies that a component comparable in size to or even larger than the red giant appeared in the binary. The formation of an ionized gaseous disk surrounding the hot component is most likely. Not only the continuum but also the emission lines originate in this disk. The disk most likely resulted from prolonged accretion of the stellar wind from the M giant onto the hot star.

The structure of the disk can be judged from the phase color curves (Fig. 2), which we improved significantly compared to our previous study (Arkhipova and Ikonnikova 1989). As we found previously and confirmed here, both color indices, $(B-V)$ and $(U-B)$, exhibit two rather narrow maxima at phases 0.8 and 0.2, decrease significantly at phase 0.5, but the color indices at phase 0.0 are not so large as those at phases 0.2 and 0.8. This implies that, after the outburst of V1329 Cyg, the red giant does not completely cover the ionized region at phase 0.0, and the bluest, outer parts of the disk are eclipsed in turn at phases 0.8 and 0.2. This clearly nonspherical (Arkhipova and Ikonnikova 1989) object probably has a structure such that the gas density in its central part closest to the subdwarf is very high, while the outer parts of the disk have a density of $\sim 10^6-10^7$ cm^{-3} and are optically thin in the continuum. The radiation of gas with $\tau < 1$ is characterized by the presence of large emission jumps near the limits of the series, in particular, the Balmer jump. The density ($N_e \sim 10^6-10^7$ cm^{-3}) and electron temperature ($T_e = 15\,000$ K) of the ionized gas in the binary V1329 Cyg were estimated by Nussbaumer and Schmutz (1983).

The two-color $U-B$, $B-V$ diagram (Fig. 3) shows the dereddened position of the star at the above orbital phases. Our calculated color indices for the hydrogen–helium continuum of a gas with an electron density $N_e \geq 10^6$ cm^{-3} and electron temperature of 15 000 K are also plotted in the diagram. We assumed the helium abundance from the emission-line intensities for V1329 Cyg published by Iijima *et al.* (1981): $\mathrm{He}^+/\mathrm{H}^+ = 0.04$, $\mathrm{He}^{++}/\mathrm{H}^+ = 0.064$.

The color indices of V1329 Cyg at phase 0.5 may be interpreted as the sum of the radiations from a blackbody with a very high temperature and a gas continuum with an electron temperature of 15 000 K. The contribution from emission lines to the UBV bands is not too large, and we disregard it. Once we estimated the contributions of the radiation components from the two-color diagram, we found that the extinction-corrected post-outburst magnitudes of the hot and gaseous components are $V_0(\mathrm{hot}) = 11\overset{m}{.}5$ and $V_0(\mathrm{gas}) = 12\overset{m}{.}4$, respectively. The observed V magnitudes are then $V(\mathrm{hot}) = 13\overset{m}{.}2$ and $V(\mathrm{gas}) = 14\overset{m}{.}1$,

Table 2. The UBV observations of V1329 Cyg in 1998–2002

JD 2400000+	U	B	V	$U-B$	$B-V$
50958	12.62	13.27	13.03	−0.65	0.24
50994	12.46	13.52	13.04	−1.06	0.48
50996	12.48	13.52	13.00	−1.04	0.52
51014	12.40	13.46	12.86	−1.06	0.60
51016	12.44	13.47	12.91	−1.03	0.54
51023	12.38	13.44	12.87	−1.06	0.57
51074	12.36	13.42	12.92	−1.06	0.50
51081	12.36	13.40	12.92	−1.04	0.48
51104	12.41	13.45	12.94	−1.04	0.51
51110	12.48	13.44	12.99	−0.96	0.45
51369	13.79	14.34	13.78	−0.55	0.56
51399	13.43	14.35	13.77	−0.92	0.58
51408	13.80	14.32	13.78	−0.52	0.54
51452	14.20	14.60	14.14	−0.40	0.46
51453	14.05	14.58	14.05	−0.53	0.53
51454	14.00	14.62	14.09	−0.62	0.53
51455	13.96	14.59	14.11	−0.63	0.48
51701	13.82	14.28	13.62	−0.46	0.66
51702	13.80	14.23	13.56	−0.43	0.67
51706	13.85	14.18	13.55	−0.33	0.63
51722	13.91	14.28	13.57	−0.37	0.71
51752	13.63	14.16	13.52	−0.53	0.64
51754	13.70	14.11	13.55	−0.41	0.56
51765	13.80	14.07	13.47	−0.27	0.60
51779	13.57	14.10	13.51	−0.53	0.59
51781	13.63	14.11	13.42	−0.68	0.69
51788	13.47	14.09	13.48	−0.62	0.61
51817	13.47	14.05	13.47	−0.58	0.58
51822	13.39	14.02	13.41	−0.63	0.61
51836	13.21	13.96	13.33	−0.75	0.63
51843	13.26	13.92	13.26	−0.66	0.66
51850	13.24	13.87	13.21	−0.63	0.66
52030	12.56	13.51	13.07	−0.95	0.44
52078	12.49	13.55	13.00	−1.06	0.55
52083	12.48	13.53	12.98	−1.05	0.55
52106	12.38	13.54	13.04	−1.16	0.50
52112	12.46	13.54	12.99	−1.08	0.55
52134	12.51	13.53	13.00	−1.02	0.53
52142	12.58	13.58	12.99	−1.00	0.59
52172	12.67	13.62	13.01	−0.95	0.61
52193	12.80	13.73	13.14	−0.93	0.59
52209	12.90	13.79	13.22	−0.89	0.57
52459	14.30	15.07	14.37	−0.77	0.70
52462	14.35	15.03	14.31	−0.68	0.72

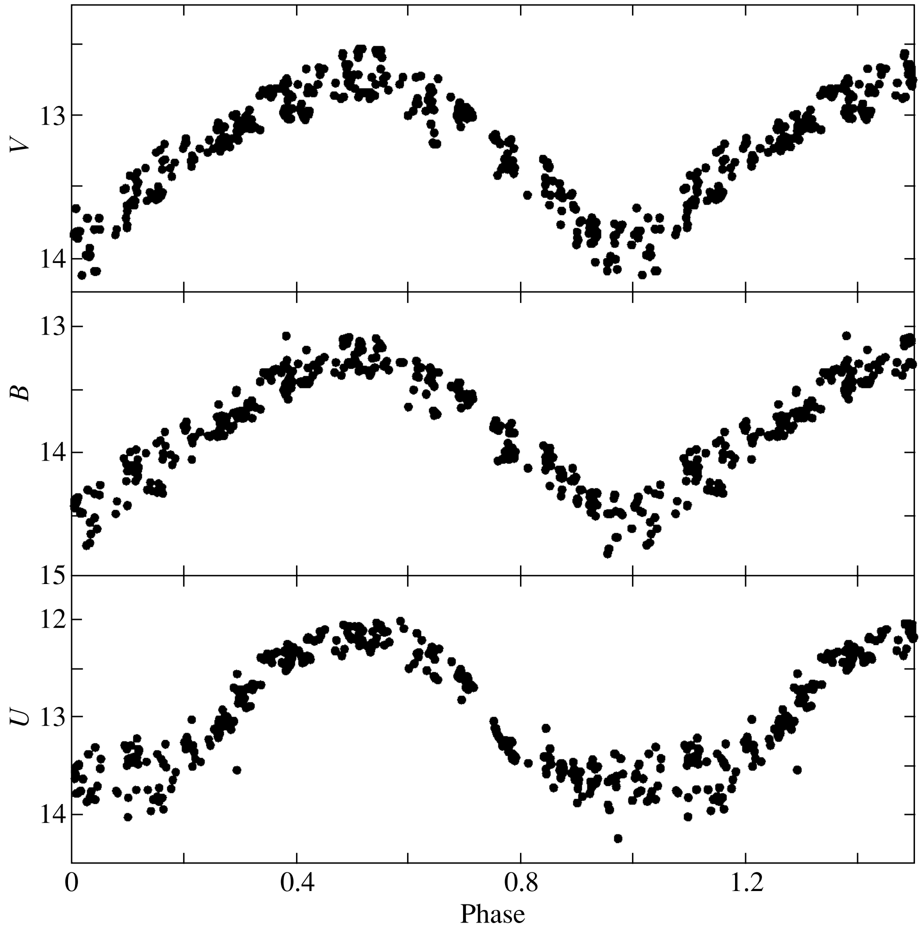

Fig. 1. UBV phase light curves of V1329 Cyg (the period is $954^{\mathrm{d}}_{\cdot}5$).

respectively. The contribution of the cool component to the V-band radiation at phase 0.5 is negligible. Here, by the hot component we mean not only the hot subdwarf, but also its new environment after the outburst. This can be a dense quasi-photosphere that also includes the inner layers of the disk.

By analogy, we can quantitatively estimate the contributions from the components of V1329 Cyg at other orbital phases by using the two-color diagram. Naturally, as the phase approaches 0.0, the contribution of the red giant to the total color indices of the binary increases. However, the $U-B$ color index is at its maximum not at this phase, when the red giant is in front of the hot star, but when it covers the bluest outer parts of the disk. The size of the disk must be on the order of the size of the red giant, because the brightness rise in the U band, where the contribution of the gas to the radiation is at its maximum, begins only at phase 0.25 and is very steep. Note also that the color indices at phases 0.2 and 0.8 differ, suggesting that the disk eclipse conditions are different and that the orbit of the binary may be elliptical.

Comparing the calculated pre- and post-outburst magnitudes of the hot component, we find the outburst amplitude of the hot component in V to be $\Delta V = 1^{m}_{\cdot}8$, a value typical of most symbiotic stars. Of course, the bolometric outburst amplitude is higher, but the estimates of the post-outburst temperature for the hot star by different authors differ significantly, and the uncertainty in the estimates of the bolometric luminosity at the maximum and outside of the outburst reduces to uncertain knowledge of the bolometric corrections for very hot ($T > 3 \times 10^4$ K) stars. In any case, the radiation from the hot subdwarf increased during the outburst by a factor of 5 to 10.

Several years after the outburst, according to determinations by different authors (Iijima 1981; Tamura 1981), the temperature of the subdwarf was very high and could have exceeded 10^5 K. We reestimated its temperature by the Zanstra method, as applied to the He(II) λ1640 Å line. The flux in this line at phases 0.5–0.6 is $F(\lambda 1640) = 4.5 \times 10^{-12}$ erg cm^{-2} s^{-1} (Nussbaumer and Schmutz 1983).

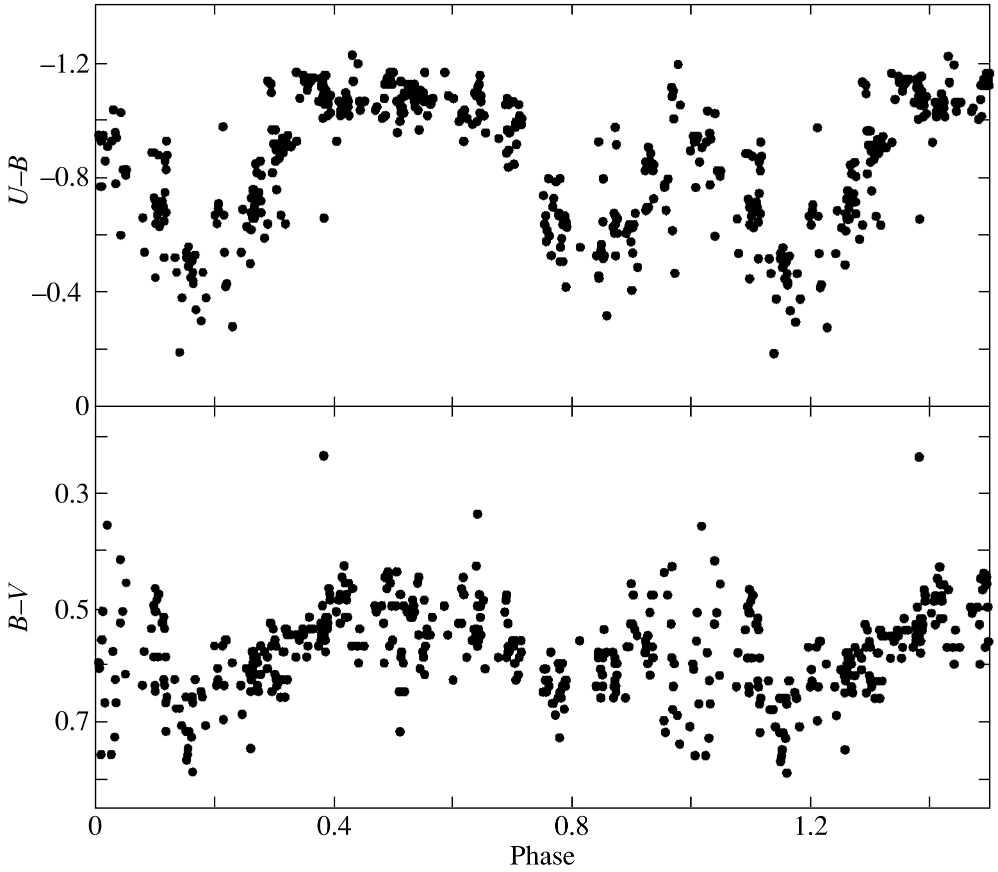

Fig. 2. $U-B$ and $B-V$ phase color curves of V1329 Cyg (the period is $954^{\mathrm{d}}.5$).

Since the stellar continuum under the line is very weak and is measured unreliably, we used the continuum measurements at a wavelength $\lambda = 3250$ Å. Nussbaumer and Schmutz (1983) obtained $F(\lambda3250) = 1.7 \times 10^{-14}$ erg cm^{-2} s^{-1} Å^{-1}. However, after reprocessing the IUE observations, Mueller *et al.* (1986) obtained a new flux estimate, $F(\lambda3250) = 3.5 \times 10^{-14}$ erg cm^{-2} s^{-1} Å^{-1}, at a photometric phase near the brightness maximum. Assuming the total absorption of the photons ionizing He II in the gaseous envelope of the hot component and taking the electron temperature of the gas to be $T_{\mathrm{e}} = 15\,000$ K, we excluded the nebular component of the continuum at $\lambda3250$ Å (for the above parameters of the gas and distance to the star, it is equal to $F_{\mathrm{n}}(\lambda3250) = 2.0 \times 10^{-14}$ erg cm^{-2} s^{-1}Å^{-1}) and obtained the temperature of the hot component $T(\mathrm{HeII}) = 1.5 \times 10^5$ K, in good agreement with the estimates by other authors. At this value of T, the bolometric correction is $>4^m$, and the post-outburst bolometric magnitude of the subdwarf is $M_{\mathrm{bol}} < -5^m.9$, $\log L/L_\odot > 4$, which gives the star's radius $R(\mathrm{hot}) > 0.2R_\odot$. During the maximum of the outburst in 1964–1969, the temperature of the star was appreciably lower (as suggested by the low excitation of the emission-line spectrum), and its radius was probably much larger.

The final parameters for the components of V1329 Cyg, including those that we obtained here, are given in Table 3.

CONCLUSIONS

Our long-term photometric UBV observations of the symbiotic nova V1329 Cyg as well as the IUE and near-infrared observations by other authors have led us the following conclusions regarding the parameters of the binary:

(1) The cool M5.5 III giant of constant brightness ($V = 15^m.05$ and $m_{\mathrm{pg}} = 17^m$) has a luminosity $M_V = 0^m.0$ and a mass $M \sim 2M_\odot$.

(2) The hot variable subdwarf with a mass $M \sim 0.7M_\odot$ had a pre-outburst luminosity $M_V \sim -0^m.1$. Its mean V magnitude was $14^m.9$, and its nonstationary behavior determined the significant brightness

Table 3. Parameters for the components of the binary V1329 Cyg

Cool component	Hot component	Gaseous component
M5.5 III Constant brightness	Variable subdwarf	Appeared after 1964 outburst
$V(\text{cool}) = 15^{m}.1$	Before outburst: $\langle V(\text{hot})\rangle = 14^{m}.9$	$V(\text{gas}) = 14^{m}.1$
$m_{\text{pg}}(\text{cool}) = 17^{m}.1$	$\langle m_{\text{pg}}(\text{hot})\rangle = 15^{m}.1$	Continuum:
$H = 7^{m}.40$	During outburst: $V(\text{hot}) = 13^{m}.2$	$(U-B)_0 = -1.75$,
$M_V(\text{cool}) = 0^{m}.0$	Before outburst: $M_V(\text{hot}) = -0^{m}.1$	$(B-V)_0 = +0.56$,
$m(\text{cool}) = 2.1M_\odot$	During outburst: $M_V(\text{hot}) = -1^{m}.9$	$N_{\text{e}} \sim 10^6$, $T_{\text{e}} \approx 15\,000$ K
$R(\text{cool}) = 100R_\odot$	$m(\text{hot}) \sim 0.7M_\odot$	
$T(\text{cool}) = 3500$ K		

fluctuations between eclipses (up to 2^m in the photographic band). The outburst of the hot component in 1964 had an amplitude of $\sim 1^{m}.8$ in V, typical of ordinary symbiotic stars; its bolometric luminosity during the outburst exceeded $10^4 L_\odot$, and its radius was $>0.2R_\odot$.

(3) The ionized gaseous disk that appeared in the binary after the outburst and that was responsible for the unusual phase $U-B$ color curve with two maxima near the inferior conjunction is comparable in size to the M giant, and its continuum radiation in V is weaker than the radiation from the hot component during the outburst by only 1^m.

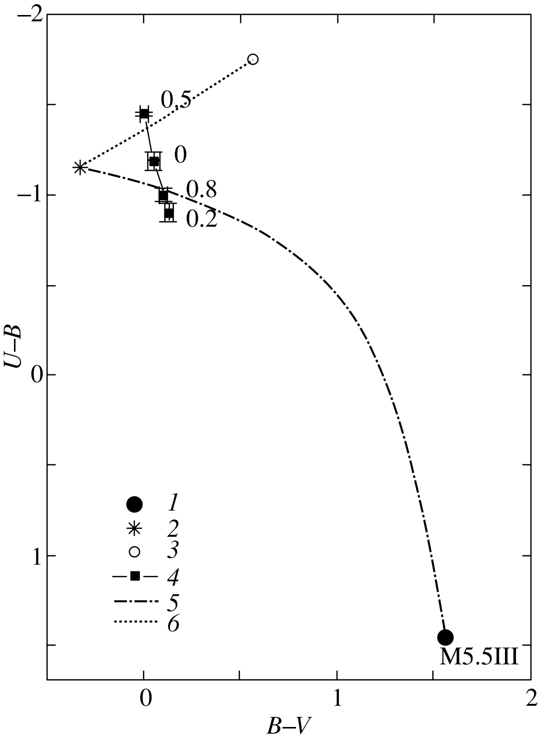

Fig. 3. Two-color $U-B$, $B-V$ diagram: *1*—the cool M5.5 III star; *2*—the hot star; *3*—the radiation of the gas continuum with $T_{\text{e}} = 15\,000$ K and $N_{\text{e}} \gg 10^6$; *4*—the mean color indices of V1329 Cyg and their dispersions for various orbital phases; *5*—the total radiation from the hot star and the M5.5 III giant; *6*—the total radiation from the hot star and the gas continuum with $T_{\text{e}} = 15\,000$ K.

Note that the mean U brightness of the binary V1329 Cyg decreased by $\sim 0^{m}.4$ during our UBV observations from 1973 until 2002, which is most likely attributable to the decrease in the luminosity of the hot component.

ACKNOWLEDGMENTS

This study was supported by the Federal Science and Technology Program for Astronomy (project no. 40.022.1.1.1103).

REFERENCES

1. D. Allen and I. S. Glass, Mon. Not. R. Astron. Soc. **168**, 1 (1974).
2. V. P. Arkhipova, Perem. Zvezdy **20**, 345 (1977).
3. V. P. Arkhipova and T. A. Belyakina, Izv. Krymsk. Astrofiz. Obs. **69**, 30 (1984).
4. V. P. Arkhipova and N. P. Ikonnikova, Pis'ma Astron. Zh. **15**, 140 (1989) [Sov. Astron. Lett. **15**, 60 (1989)].
5. V. P. Arkhipova and O. E. Mandel', Inf. Bull. Var. Stars, No. 722 (1973).
6. V. P. Arkhipova and O. E. Mandel', Pis'ma Astron. Zh. **17**, 359 (1991) [Sov. Astron. Lett. **17**, 151 (1991)].
7. G. B. Baratta and R. Viotti, Astron. Astrophys. **229**, 104 (1990).
8. D. Chochol, I. L. Andronov, V. P. Arkhipova, *et al.*, Contrib. Scalnate Pleso Astron. Soc. **29**, 31 (1999).
9. F. Fekel, K. Hinkle, R. Joyce, and M. Skrutskie, Astron. J. **121**, 2219 (2001).
10. P. J. Flower, Astrophys. J. **469**, 355 (1996).
11. J. Grygar, L. Hric, D. Chochol, and A. Mammano, Bull. Astron. Inst. Czech. **30**, 308 (1979).
12. Y. Ikeda and S. Tamura, Publ. Astron. Soc. Jpn. **52**, 589 (2000).
13. T. Iijima, in *Photometric and Spectroscopic Binary Systems, NATO Advanced Study Institute,* Ed. by E. B. Carling and Z. Copal (Reidel, Dordrecht, 1981), p. 517.
14. T. Jijima, A. Mammano, and R. Margoni, Astrophys. Space Sci. **75**, 237 (1981).

15. S. H. Kenyon, Astron. J. **96**, 337 (1988).
16. M. Landini, A. Natta, E. Oliva, *et al.*, Astron. Astrophys. **134**, 284 (1984).
17. U. Munari, R. Margoni, and A. Mammano, Astron. Astrophys. **202**, 83 (1988).
18. B. E. A. Mueller, H. Nussbaumer, and W. Schmutz, Astron. Astrophys. **154**, 313 (1986).
19. H. Nussbaumer and W. Schmutz, Astron. Astrophys. **126**, 59 (1983).
20. H. Nussbaumer, W. Schmutz, and M. Vogel, Astron. Astrophys. **169**, 154 (1986).
21. R. Rudy, S. Meier, G. Rossano, *et al.*, Astrophys. J., Suppl. Ser. **121**, 533 (1999).
22. R. M. Stienon, M. R. Chartrand, and C. Y. Shao, Astron. J. **79**, 47 (1974).
23. V. Straizhis, *Multicolor Stellar Photometry* (Mokslas, Vilnius, 1977) [in Russian].
24. S. Tamura, Publ. Astron. Soc. Jpn. **33**, 701 (1981).
25. S. Tamura, Publ. Astron. Soc. Jpn. **35**, 317 (1983).
26. O. G. Taranova and B. F. Yudin, Astron. Zh. **63**, 151 (1986) [Sov. Astron. **30**, 93 (1986)].
27. H. Schild and H. M. Schmid, Astron. Astrophys. **324**, 606 (1997).

Translated by N. Samus'

Astronomy Letters, Vol. 30, No. 2, 2004, pp. 124–137. Translated from Pis'ma v Astronomicheskiĭ Zhurnal, Vol. 30, No. 2, 2004, pp. 146–160.
Original Russian Text Copyright © 2004 by V. Snytnikov, Vshivkov, Kuksheva, Neupokoev, Nikitin, A. Snytnikov.

Three-Dimensional Numerical Simulation of a Nonstationary Gravitating *N*-Body System with Gas

V. N. Snytnikov[1,2*], V. A. Vshivkov[3,4], E. A. Kuksheva[1], E. V. Neupokoev[4,5], S. A. Nikitin[6], and A. V. Snytnikov[4,5]

[1]*Institute of Catalysis, Siberian Branch, Russian Academy of Sciences, Novosibirsk, Russia*
[2]*Novosibirsk State University, Novosibirsk, Russia*
[3]*Institute of Computational Technologies, Siberian Branch, Russian Academy of Sciences, Novosibirsk, Russia*
[4]*Novosibirsk State Technical University, Novosibirsk, Russia*
[5]*Institute of Computational Mathematics and Mathematical Geophysics, Siberian Branch, Russian Academy of Sciences, Novosibirsk, Russia*
[6]*Institute of Nuclear Physics, Siberian Branch, Russian Academy of Sciences, Novosibirsk, Russia*

Received April 14, 2003

Abstract—We developed a three-dimensional numerical model to investigate nonstationary processes in gravitating N-body systems with gas. We used efficient algorithms for solving the Vlasov and Poisson equations that included the evolutionary processes under consideration, which ensures rapid convergence at high accuracy. We give examples of the numerical solution of the problem on the growth of physical instability in the model of a flat rotating disk with a gaseous component and its three-dimensional dynamics under various initial conditions including a nonzero velocity dispersion along the rotation axis.

Key words: *galaxies, groups and clusters of galaxies, intergalactic gas, celestial mechanics.*

INTRODUCTION

The last three decades have been marked by rapid progress in the numerical simulation of star clusters. The stability of disk systems, the formation of a bar and a spiral pattern in them, the influence of strong external perturbations, the ratio and mutual influence of the gaseous and stellar components, the role of the central mass, accretion and protoplanetary disks, and other objects and processes have been the subjects of research by means of simulations. Even the first such studies (see, e.g., Hohl and Hockney 1969; Eneev *et al.* 1973; Miller 1976) showed that the self-consistent gravitational interaction between many bodies is the key mechanism responsible for the wide variety of structures observed in the sky. However, the demonstration stage of development of this kind of simulation has ended. Attention is now focused on the investigation of three-dimensional nonstationary problems, one of which is the problem of physical instabilities in self-gravitating N-body systems with gas. Important examples are the stellar disks of real galaxies in a quasi-steady equilibrium with slow dynamical evolution. Such disks have been considered with the aim of investigating the various mechanisms of their self-sustenance (Khoperskov *et al.* 2003). The studies of other, purely unstable structures (protoplanetary disks) are of considerable interest with regard to the formation of gas–dust clusters in them. Objects with the pronounced formation dynamics of stellar and protoplanetary clusters in such large cloud-shaped molecular complexes as Orion, Taurus–Auriga, Perseus, Ophiuchus, Chaemeleon, Vela, Cepheus, Corona Austalis, Serpens, Monoceros, Gum, and others arouse particular interest (Avedisova 1998).

A traditional problem of numerical simulation is the spirality of galactic disks. Main results and the difficulties that arose in this way were described, for example, by Miller (1976) and Sellwood (1983, 1999). Miller gave a list of critical points without a clear and comprehensive analysis of which the reliability of the numerical simulation may be called into question. In particular, these include the accuracy of tracking the paths of bodies, the observance of conservation laws, the influence of introduced numerical meshes, the

---

*E-mail: `snyt@catalysis.nsk.su`

changes in forces on small scales, and several other conditions. Some of the critical points (the number of model particles and the order of the integration scheme) depend mainly on computer performance capabilities. Others (the introduction of numerical meshes and the change in forces on certain scales) are related to the deep problems of computational physics. Only the simultaneous fulfillment of the main requirements can give us confidence that the numerical model is close to the original physical model in the principles of reproducing the forces and conservation laws on all of the space–time scales accessible in computations.

Two main approaches can be singled out in the problems of gravitational physics under study. In the first approach, the N-body problem, the pairwise interaction between gravitating bodies is considered. This approach suggests that the bodies can be scattered through large angles, which requires taking special measures in solving collisionless problems. Important results in simulating N-body dynamics were achieved after the development of tree codes for supercomputers (Barnes and Hut 1986; Makino 1990). A significant limitation of this approach is the difficulty of extending the numerical model to study the gravitational dynamics of gas, magnetic fields, and other important physical effects. In the second approach, the starting point for studies is the solution of the collisionless Vlasov–Liouville equation by the particle method and of the Poisson equation for a collective self-consistent field. This mathematical model can be easily supplemented with gas-dynamical, radiative transfer, Maxwell, and other equations, which allows the above effects to be taken into account.

In this paper, we use the second approach to consider some of the fundamentally important problems of the numerical simulation of global gravitational systems. The latter are actually rotating clusters of either stars in galaxies or large agglomerates of particles (planetesimals) in protoplanetary accretion disks in the presence of a gaseous component in both cases. The motion of stars, particles, and gas takes place in a collective self-consistent gravitational field on which the quasi-stationary fields of the central mass and other slow-moving bodies can be superimposed. We describe our numerical model for the three-dimensional simulation of nonstationary processes in gravitating systems with a self-consistent and external field. We demonstrate the efficiency of the code by solving the problem on the dynamics of massive bodies with gas in the approximation of a thin disk (a protoplanetary disk, an equatorial galactic plane) with the model choice of initial conditions and the problem with completely three-dimensional particle motion.

MAIN PROBLEMS OF NUMERICAL SIMULATIONS IN THE N-BODY PROBLEM

The main problems of numerical simulations in the N-body problem are as follows. First, the possible distortions of the force law, to the largest degree at short distances, are an important peculiarity of numerical simulations. Since the processes under consideration are nonlinear and nonstationary, these distortions can have a crucial effect on the final result. Second, this group includes the well-known problem of initial conditions for static self-consistent models, which, in turn, originates from the quiet-start problem in plasma calculations (Miller 1976; Sellwood 1999). The presence of initial, anomalously large velocity fluctuations due to the restriction on the number of particles in the model system ($\sim 10^7$, while the typical number of stars in a galaxy is $\sim 10^{10}$–10^{11}) leads to a violation of the static conditions, although the moments of the distribution function are specified in agreement with these conditions. The third example from computational experiments in plasma physics is related to self-heating. This effect arises from the error in approximating the force that acts on each particle when a mesh is introduced to compute the potential. The first manifestation of this effect is a change in the total energy of the system. This error for standard algorithms of the particle method does not decrease with decreasing spatial step (Vshivkov and Snytnikov 1998). The fourth difficulty of using the particle method in the problem under consideration is a violation of one of the fundamental conservation laws for standard algorithms. This well-known effect (Berezin and Vshyvkov 1980) is not too pronounced for problems with a wall-bounded plasma, but is the key effect in interpreting and analyzing the results of numerical simulations for such isolated systems as galactic disks.

To solve the first of the above problems, it is crucially important to ensure that there is no numerical divergence when integrating the system of many interacting particles against the growth of generally non-Jeans instabilities. The problem of divergence that arises from the strengthening of the interaction with decreasing separation between the particles is commonly solved by cutting off the gravitational forces on a length comparable to the mesh step. For this reason and because of the tabulation of the potential at mesh points, the effective force law differs from Newtonian law. Notwithstanding, it is assumed (Miller 1976) that calculations of stellar dynamics with changed forces can be used to investigate large-scale perturbations. The fact (Hohl and Hockney 1969) that the particle velocity dispersion does not increase due to the cutoff of the forces at short distances is taken as the main argument for this assumption. From our point of view, this conclusion is nevertheless controversial for the existence conditions of transient structures the basis for which is a nonsmooth distribution function with rapidly growing local perturbations. The development of perturbations (clumps of matter) leads to the growth of large-scale spatial instability with a redistribution of matter in the disk.

The correct realization of the force law in a numerical algorithm is required to resolve the existing contradictions in the theory of spiral structures. Bertin and Lin (1996) assumed the presence of long-lived quasi-stationary spiral modes. In their opinion, the observed spirals are global instabilities that grow slowly in a dynamically cold disk with a smooth density distribution function. From an alternative point of view, spiral galaxies are short-lived structures that appear in a fast sequence of particular evolutionary cycles, growing through their mutual strengthening as forced responses (Sellwood 1999).

Another example of the importance of faithfully reproducing interaction is the gravitational instability of a gas–dust protoplanetary disk in which the formation of clusters of certain sizes and densities inevitably affects the space–time scales of the processes that lead to the growth of particles through their amalgamation during collisions. The dynamics of the amalgamating condensed phase in a protoplanetary disk is an important element for the planet-formation theory (Safronov 1969) and for the physical justification of the hypothesis about the primordial synthesis of high-molecular compounds in a circumstellar disk, a global chemical reactor (Snytnikov *et al.* 2002b).

The main problem of numerical simulations in the physics of gravitating systems is the necessity of developing algorithms that are unstable in the linear approximation, because the growth of physical instabilities must be considered. This implies that there are no reliable guarantees against the manifestation of scheme instabilities and that it is necessary to ensure convergence and approximation of the algorithm as a whole. The following should be borne in mind when evaluating the required measures. First, numerical instability can be suppressed by introducing artificial damping. In this case, however, the properties of instabilities with growth rates of the same order of magnitude change radically, and the resulting space–time structures are distorted. Second, because of their nonlinear evolution, these structures depend on its entire prehistory and, hence, on the computational accuracy in each space cell and at each time step.

By now, two methods that differ by their procedure for calculating forces have been mainly used to numerically simulate self-consistent gravitating systems with the solution of the Vlasov–Liouville and Poisson equations. The first is the method of pairwise interactions. According to this method, point masses are initially distributed at spatial mesh points; then, by adding up the contributions $\propto 1/r$ from each mesh point, the distribution of the total potential is restored with subsequent interpolation at the actual particle locations. In this case, as the cell size decreases, the errors attributable to the application of the force cutoff procedure increase. In the limit, the method transforms into the method of direct (particle–particle) simulation. As a result, there is no convergence or approximation of the potential. Such limitations also arise in the second method in which the Fourier representation of the effective particle distribution at spatial mesh points is used to find the corresponding solution of the Poisson equation. An advantage over the first method is that the number of operations decreases from M^2 to $M \ln M$, where M is the number of mesh points. The cutoff of the interaction scale consists in discarding the contribution from higher spatial harmonics, which, as experience shows, is necessitated by the fact that the system of linear algebraic equations, a Fourier analogue of the Poisson equation, is ill-conditioned. Thus, direct methods, to which the above two methods belong, can give a large error when the number of mesh points increases significantly ($>10^7$–10^8).

Below, we describe our approach to simulating the gravitational self-consistent dynamics of N bodies with gas by efficiently using the combined method of solving the three-dimensional Poisson equation in finite differences (the over-relaxation method). We use peculiarities of the evolution process, i.e., take into account the known potential distribution at the preceding step. Our approach fundamentally differs from direct methods in the following: the errors related to the decrease in mesh step do not increase, a high degree of convergence can be achieved, and it can be used to develop codes for modern multiprocessor computers.

AN N-BODY MODEL FOR INVESTIGATING GRAVITATIONAL INSTABILITY

In simplified form, the numerical model of gravitational physics reduces to a gravitational N-body problem. The collisionless Vlasov kinetic equation and the Poisson equation underlie this model. The model allows us to study nonstationary processes in protoplanetary disks or star clusters under self-gravitation. The self-consistent gravitational field of a particle ensemble nonlinearly affects individual particles. Instability and stochasticity show up in the particle dynamics. The unstable dynamics of individual particles leads to the formation of their clusters and to the separation of fragments followed by their contraction into large agglomerates. In this case, the centrifugal forces and the velocity dispersion prevent the collapse of particles to the center of mass. The formation of clusters in itself must affect the agglomeration time scales when particles amalgamate through a collective multiparticle interaction. It is important to note that the growth time scales for gravitational instability can be several orders of magnitude shorter than the pair collision time scales.

The Vlasov–Liouville kinetic equation in the collisionless approximation of an averaged self-consistent field can be written as

$$\frac{\partial f}{\partial t} + \mathbf{u}\frac{\partial f}{\partial \mathbf{r}} + \mathbf{a}\frac{\partial f}{\partial \mathbf{u}} = 0, \tag{1}$$

where $f(t, \mathbf{r}, \mathbf{u})$ is a time-dependent (t) one-particle coordinate $(\mathbf{r})$ and velocity $(\mathbf{u})$ distribution function; $\mathbf{a} = -\nabla\Phi$ is the acceleration of particles of unit mass $m = 1$. The gravitational potential Φ in which the motion takes place can be divided into two parts:

$$\Phi = \Phi_1 + \Phi_2,$$

where Φ_1, depending on the simulated conditions, is either the potential of a stationary central mass (a black hole with a bulge, a protostar) or the potential of a system of stationary matter outside the disk plane (galactic halo stars, a molecular cloud). The second part of the potential, Φ_2, is determined by the total distribution of moving particles and satisfies the equation in cylindrical coordinates:

$$\frac{1}{r}\frac{\partial}{\partial r}\left(r\frac{\partial \Phi_2}{\partial r}\right) + \frac{1}{r^2}\frac{\partial^2 \Phi_2}{\partial \varphi^2} + \frac{\partial^2 \Phi_2}{\partial z^2} = 4\pi G\rho. \tag{2}$$

For an infinitely thin disk, the volume density of the moving medium, ρ, throughout the volume is equal to zero ($\rho = 0$). A discontinuity of the normal derivative of the potential takes place on the disk itself with a surface density σ. This discontinuity yields a boundary condition for determining the potential Φ_2: $\frac{\partial \Phi_2}{\partial z} = 2\pi G\sigma$.

To obtain dimensionless variables, we chose the distance R_0, the mass M_0, and the gravitational constant G as the main characteristic parameters. For example, the galactic radius and mass or the circumstellar-disk scale size and the protostar mass may be used as R_0 and M_0, respectively. The corresponding characteristic particle velocity (V_0), time (t_0), potential (Φ_0), and surface density (σ_0) are

$$V_0 = \sqrt{\frac{GM_0}{R_0}}, \quad t_0 = \frac{R_0}{V_0},$$

$$\Phi_0 = V_0^2 = \frac{GM_0}{R_0}, \quad \sigma_0 = \frac{M_0}{R_0^2}.$$

As the auxiliary parameters, we specify the following: the radius $r_{\max}$ and height $z_{\max}$ of the cylindrical computational region; the radius r_0 and mass of the disk and the radial particle velocity dispersion (for a Gaussian velocity distribution function). In addition, we specify the time step τ, the number of time steps, the total number of model particles, and the iteration and other "technical" parameters.

It is convenient to begin our analysis of the physical instabilities in systems far from a stable equilibrium with very simple models for the initial particle distribution. In our case, for disk structures, we chose the model of rigid-body rotation (see, e.g., Polyachenko and Fridman 1976) as this distribution. The initial particle velocities correspond to circular particle motion around the coordinate origin with an angular velocity Ω_0. The radial velocity dispersion δv_r is specified by a Gaussian law with a zero mean and a dispersion that is commonly characterized in units of the Toomre critical velocity (Toomre 1964), $c_{\mathrm{T}} = 3.36G\sigma_{\mathrm{c}}/æ$, where, in our case, $\sigma = \sigma_{\mathrm{c}}$ is the initial density at the center of a disk with radius r_0, and æ is the epicyclic frequency (æ $= 2\Omega_0$ in the model of rigid-body rotation). The centrifugal force $\Omega_0^2 r$ is balanced by the centripetal gravitational force $(-\partial\Phi/\partial r)$.

Thus, the system of equations in dimensionless form together with the initial and boundary conditions appears as

$$\frac{\partial f}{\partial t} + u_r\frac{\partial f}{\partial r} + \frac{u_\varphi}{r}\frac{\partial f}{\partial \varphi} + \left(\frac{u_\varphi^2}{r} - \frac{\partial \Phi}{\partial r}\right)\frac{\partial f}{\partial u_r}$$
$$- \left(\frac{u_r u_\varphi}{r^2} + \frac{1}{r^2}\frac{\partial \Phi}{\partial \varphi}\right)\frac{\partial f}{\partial\left(\frac{u_\varphi}{r}\right)}$$
$$+ u_z\frac{\partial f}{\partial z} - \frac{\partial \Phi}{\partial z}\frac{\partial f}{\partial u_z} = 0,$$

$$\frac{1}{r}\frac{\partial}{\partial r}\left(r\frac{\partial \Phi_2}{\partial r}\right) + \frac{1}{r^2}\frac{\partial^2 \Phi_2}{\partial \varphi^2} + \frac{\partial^2 \Phi_2}{\partial z^2} = 0,$$

$$z = 0: \qquad \frac{\partial \Phi_2}{\partial z} = 2\pi\sigma = 2\pi\int f du_r du_\varphi,$$

$$t = 0: \qquad \sigma(r, \varphi) = \begin{cases} 3\sqrt{1 - r^2}, & r \le 1 \\ 0, & r > 1. \end{cases}$$

THREE-DIMENSIONAL SIMULATION OF A STABLE STELLAR DISK

The initial conditions in the problem of the three-dimensional simulation of a quasi-stationary stellar disk with a halo and a bulge are more difficult to specify. We followed the description of these conditions and the notation of parameters from Khoperskov *et al.* (2003), whose goal was to establish the minimum stellar velocity dispersion level in stable disk systems. In particular, the distribution of the halo volume density corresponded to a flat rotation curve in the region where the halo dominated; the spherical bulge was specified according to the King model. The initial velocity distribution function is a Schwarzschild one with nonzero radial (c_r) and vertical (c_z) velocity dispersions. The surface density is characterized by the scale length L that determines the exponential law $\sigma \propto \exp(-r/L)$ (for $r \geq 5L$, the density is equal to zero). The initial vertical structure of the disk can be found from the equation for the disk volume density, which combines the Poisson equation and the condition for equilibrium between the effects of gravitation and thermal scatter of particles (stars). Our numerical simulations differ from the above work in that the latter uses a direct dynamical model with a pairwise Newtonian interaction between particles, while we solve the three-dimensional Poisson and Vlasov equations.

A MODEL OF A GAS–DUST DISK

The evolution of a rotating gas–dust disk with a self-consistent gravitational field can be described by the system of equations (1) and (2) with the addition of a third, gas-dynamical component. This gas-dynamical part is represented by the equations in polar coordinates:

$$\frac{\partial \rho_{\mathrm{g}}}{\partial t} + \frac{1}{r}\frac{\partial}{\partial r}(r v_r \rho_{\mathrm{g}}) + \frac{1}{r}\frac{\partial}{\partial \varphi}(v_\varphi \rho_{\mathrm{g}}) + \frac{\partial}{\partial z}(v_z \rho_{\mathrm{g}}) = 0, \tag{3}$$

$$\frac{\partial v_r}{\partial t} + v_r\frac{\partial v_r}{\partial r} + \frac{v_\varphi}{r}\frac{\partial v_r}{\partial \varphi} - \frac{v_\varphi^2}{r} + v_z\frac{\partial v_r}{\partial z} = -\frac{1}{\rho_{\mathrm{g}}}\frac{\partial p}{\partial r} - \frac{\partial \Phi}{\partial r} - \frac{F_r^{\mathrm{fr}}}{\rho_{\mathrm{g}}},$$

$$\frac{\partial v_\varphi}{\partial t} + v_r\frac{\partial v_\varphi}{\partial r} + \frac{v_\varphi}{r}\frac{\partial v_\varphi}{\partial \varphi} + \frac{v_r v_\varphi}{r} + v_z\frac{\partial v_\varphi}{\partial z} = -\frac{1}{r\rho_{\mathrm{g}}}\frac{\partial p}{\partial \varphi} - \frac{1}{r}\frac{\partial \Phi}{\partial \varphi} - \frac{F_\varphi^{\mathrm{fr}}}{\rho_{\mathrm{g}}},$$

$$\frac{\partial v_z}{\partial t} + v_r\frac{\partial v_z}{\partial r} + \frac{v_\varphi}{r}\frac{\partial v_z}{\partial \varphi} + v_z\frac{\partial v_z}{\partial z} = -\frac{1}{\rho_{\mathrm{g}}}\frac{\partial p}{\partial z} - \frac{\partial \Phi}{\partial z} - \frac{F_z^{\mathrm{fr}}}{\rho_{\mathrm{g}}},$$

where ρ_{g} is the gas density; v_r, v_φ, and v_z are the r, φ, and z velocity components of the gas; p is the gas pressure; Φ is the gravitational potential; F_r^{fr}, F_φ^{fr}, and F_z^{fr} are the r, φ, and z components of the friction force between the dust and the gas. The pressure p is assumed to be a function of the gas density: $p = p(\rho_{\mathrm{g}})$. Since the gas volume density becomes the surface density in the model of a flat disk, we express the pressure in units of $p_0 = \sigma_0 V_0^2$.

The motion of dust particles described by the collisionless Vlasov kinetic equation is modified by the change in particle acceleration:

$$\frac{\partial f}{\partial t} + \mathbf{u}\frac{\partial f}{\partial \mathbf{r}} + \mathbf{a}\frac{\partial f}{\partial \mathbf{u}} = 0, \tag{4}$$

where $f(t, \mathbf{r}, \mathbf{u})$ is the velocity ($\mathbf{u}$) distribution function of the dust particles, and $\mathbf{a} = -\nabla\Phi + \mathbf{F}^{\mathrm{fr}}/m$. The friction force $\mathbf{F}^{\mathrm{fr}} = æ m \rho_{\mathrm{g}}(\mathbf{u} - \mathbf{v})$ can be calculated from the generalized coefficient of friction between the gas and the dust, æ.

The input parameters include the sizes of the computational (cylindrical) region, the radius and total mass of the solid-phase disk, the dispersion of the radial particle velocity with a Gaussian distribution, the radius of the gaseous disk, the total mass of the gas, the central pressure, the adiabatic index, and the coefficient of friction between the solid and gaseous phases. The initial state of the gas–dust disk can be determined by various methods. In particular, of considerable interest are calculations in which particles and gas initially move in circles around the coordinate origin. In a simple case, the initial particle and gas density distributions correspond to the model of rigid-body rotation.

CONSERVATION LAWS

For an isolated gas–dust disk without stationary components (a bulge, a halo, and a central body), the laws of conservation of mass, momentum, angular momentum, and total energy follow from the system of equations (1)–(4). The last two equations can be written as

$$\mathcal{M}_z = \sum_j m_j r_j u_{\varphi j} + \int r \sigma_{\mathrm{g}} v_\varphi dS \equiv \mathrm{const}$$

and

$$E = \sum_j \left[\frac{m_j}{2}\left(u_{rj}^2 + u_{\varphi j}^2\right) + \frac{m_j}{2}\Phi_j\right] + \int \left(\frac{\sigma_{\mathrm{g}}}{2}\left(v_r^2 + v_\varphi^2\right) + \frac{\sigma_{\mathrm{g}}\Phi}{2} + \sigma_{\mathrm{g}}\xi\right) dS \equiv \mathrm{const},$$

where σ_{g} is the gas surface density,

$$\xi = \int \frac{p}{\sigma_{\mathrm{g}}^2} d\sigma_{\mathrm{g}}, \qquad p = (\gamma - 1)\sigma_{\mathrm{g}}\xi.$$

In addition, the virial theorem can play an important, but as yet inadequately studied role. This theorem shows a change in the moment of inertia (I)

of the entire system during the motion of particles in its gravitational field:

$$\frac{1}{2}\frac{d^2I}{dt^2} = 2W + U - 3PV,$$

where W is the kinetic energy, U is the potential energy, and P is the pressure at the boundary of volume V (Bertin 2000).

NUMERICAL METHODS

Solving the Vlasov Equation

The method of particles in cells is used to solve the Vlasov kinetic equation. Initially, equal-mass model particles are distributed in the region of solution in such a way that their number in a cell is proportional to the density in it and its size. The particles have a velocity equal to the velocity of the matter at the corresponding point. The equations of motion for the particles are solved by using Boris's standard scheme (Berezin and Vshyvkov 1980) The latter consists in solving the equations of motion in Cartesian coordinates followed by the transformation of the particle coordinates and velocities to cylindrical coordinates. In this case, the components of the gravitational force are interpolated from the mesh points to the particle locations. The interpolation is performed in such a way that the particle orbit in the central field in the absence of additional perturbations remains circular. The computational scheme provides for the observance of the energy and angular momentum conservation laws for a single particle.

Solving the Gas-Dynamical Equations

The large-particle method (Belotserkovskii and Davydov 1995) is used to solve the system of gas-dynamical equations (3). This method best agrees with the particle method of solving the Vlasov–Liouville kinetic equation. It allows the gas–vacuum boundary to be traced and ensures that the laws of conservation of mass and angular momentum are automatically obeyed. The implemented scheme has the first order of accuracy in spatial variables and time. In choosing a scheme for our simulations, we took into account the fact that the first-order scheme alone from this class does not yield a countable dispersion with the appearance of numerical density fluctuations, which are particularly large for abrupt changes in the functions and at the boundaries. The absence of such fluctuations is required to compute gravitational physical instabilities. In addition, complex problems at the boundaries with a vacuum arise in schemes with a higher order of accuracy.

Solving the Poison Equation

The reliability of the numerical models under consideration and their stability against unavoidable errors depend significantly on the conditionality parameter for the matrix of the system of linear equations that arise when solving the Poisson equation in finite differences. The system of linear algebraic equations that is derived when approximating the Poisson equation can be shown (Snytnikov *et al.* 2002a) to be ill-conditioned; the conditionality deteriorates with decreasing spatial mesh step h. As a result, the direct methods of solution (the Gaussian elimination method, the Fourier transform method) can generally accumulate a large uncontrollable error during computations in nonstationary problems, while the iterative methods require a large number of iterations that also depend on the conditionality of the system. Nevertheless, special, highly efficient approaches are possible. Since the initial approximation may be taken from the preceding time step when solving the evolution problem, to solve the Poisson equation we chose the iterative method of successive over-relaxation along the Z axis, the Fourier transform method in azimuthal angle, and the sweep method along the radius. The mesh has more than a million points; convergence with a relative accuracy of 10^{-6} is achieved, on average, after 3–5 iterations.

Thus, to increase the efficiency of our computations and to be able to exploit the numerical model on personal computers, we used reconciled iteration algorithms by taking into account the peculiarities of the nonstationary processes under consideration. The principal difference between our approach and the previously described approaches using the direct methods of solving the Poisson equation is the possibility of achieving rapid convergence at high accuracy under the conditions of an evolutionary change in the solutions. This property is particularly important for simulating the nonlinear growth of physical instability in a gas–dust medium with a self-consistent gravitational field. The efficiency of the algorithms can be increased further by developing methods of their concurrent implementation for multiprocessor computers.

NUMERICAL RESULTS

At present, we have developed two modifications of the numerical model. The first, better-studied model is based on the solution of the Poisson equation, provided that the particle motion is bounded by a plane. In this sense, the model may be called 3D2V, or "quasi-three-dimensional." On the one hand, this approximation is justified, because the thicknesses of real galaxies are an order of magnitude smaller than their radii, and it would be most efficient to study the main patterns of evolution of the disk by using this model. On the other hand, the presence of an additional degree of freedom leads to a change in the quantitative criteria for the behavior of a gravitational system in terms of the growth of instabilities in it (Polyachenko and Fridman 1976). This question can be explored only with the second model, which is completely three-dimensional.

From the viewpoint of specifying the boundary conditions, 3D2V is not a new model (Miller 1976). A new result may be considered to be the fact that we managed to obtain a varied spectrum of the behavior of a rotating gas–dust disk as a function of the variations in the following parameters: the mass of the gaseous component in the disk M_{g}, the total mass of the large particles in the disk M_{p}, the mass of the central body M_{s}, and the radial particle velocity dispersion δv_r. The solutions proved to be weakly sensitive to the adiabatic index in the range from 2.5 to 1.1. Below, we present the results for $\gamma = 5/3$. The coefficient of friction between the gaseous and solid phases was assumed to be zero. The central pressure for the initial state of the disk was 0.01, in units of p_0.

Instability of a Cold Disk

In the absence of gas or in the approximation of a negligible gas density from the viewpoint of its influence on the dynamics of the system, the numerical model allows us to study the collective processes of self-organization in a flat (quasi-three-dimensional) rotating disk composed of particles without pair collisions. A cold, rotating disk composed of particles is known (Polyachenko and Fridman 1976) to be unstable against the growth of Jeans perturbations in its plane. In the short-wavelength approximation (Toomre 1964), the dispersion relation for the radial modes in a rigidly rotating disk in the absence of a velocity dispersion takes the form

$$\omega^2 = 4\Omega^2 - 2\pi G\sigma_0 k,$$

where $k = 2\pi/\lambda$ is the wave number. The Toomre critical wavelength is $\lambda_{\mathrm{T}} = \pi^2 G\sigma_0/2\Omega^2$. For the central part of the disk, $\lambda_{\mathrm{T}} \sim 2R$, with the short-wavelength approximation being valid if $\lambda \ll \lambda_{\mathrm{T}}$. In the theory under consideration, the growth rates of large-scale modes ($\lambda \sim R$) cannot be determined. At the same time, it leads us to conclude that perturbations with wavelengths $\lambda \le 2R$ are unstable.

A cold disk is the limiting case of a hot disk with a velocity dispersion of its constituent particles $\sigma_V = c_r$ for $\sigma_V \to 0$. Because of the nonzero disk temperature, instability takes place for wavelengths longer than the critical (Jeans) wavelength λ_{J}. The Jeans wavelength is easiest to estimate in the hydrodynamic approximation from the model of an infinite homogeneous layer with a density $\sigma_0 = \mathrm{const}$ (Polyachenko and Fridman 1976; Bertin 2000). Plane density perturbation waves with a wavelength shorter than the critical value $\lambda_{\mathrm{J}} \sim \sigma_V^2/(G\sigma_0)$ will not be amplified in this model. For a rigidly rotating disk, this estimate is valid if the critical wavelength satisfies the condition $k^2\sigma_V^2 \gg 4\Omega^2$, which actually holds for a velocity dispersion smaller than the Toomre velocity. A more accurate dispersion relation follows from the short-wavelength approximation for a hot rotating disk (Lin *et al.* 1969), which is not considered here.

In practical calculations, a cold rotating disk can be reproduced with the model of a hot disk composed of particles with a very small velocity dispersion relative to their regular rotation. The instability region in order of magnitude of the wavelength can be estimated from the inequality $\lambda_{\mathrm{J}} < \lambda < 2R$.

Figure 1 shows the results of our calculations for a disk that consists of 3×10^5 particles and that has the following parameters, in relative units: the disk mass (there is no central body) $M_{\mathrm{p}} = 1$; the velocity dispersion is small, $c_r = 10^{-4}$; and the central density $\sigma_0 \approx 1/2$. The time parameter $t = 4$ in the model corresponds to complete disk rotation with the initial angular velocity. According to the theory of disk stability, the smallest scale of unstable perturbations in the short-wavelength approximation is $\lambda_{\mathrm{J}} \sim 2 \times 10^{-8}$.

We see from our results that a fundamental radial (azimuthally symmetric) mode in the form of a ringlike cluster develops near the center of the disk by a time $t \sim 0.3$ (in what follows, lighter regions in the figures correspond to higher densities). This perturbation owes its origin to the peculiarity of specifying the particle distribution at the very center of the disk where there is a particle-free region for the placement of a central body (a black hole) in it. The particles that fall into this region are assumed to be absorbed by the central body; the mass of the latter increases accordingly. In our case, the initial mass of the central body is equal to zero, and the distribution with a black hole is no longer a strictly equilibrium one, as in the model of rigid-body rotation. As a result, a compression wave emerges; this wave expands from the center and is significantly amplified by the end of the first rotation of the unperturbed disk ($t = 1.86$). Subsequently, its expansion velocity decreases, and clustering begins. By a time $t \approx 5$, the ring completely breaks up into several clusters. Actually, we are observing an example of the influence of initial perturbations on the growth of instability. The latter leads to a pattern of matter distribution completely different from the initial one in a very short time (on

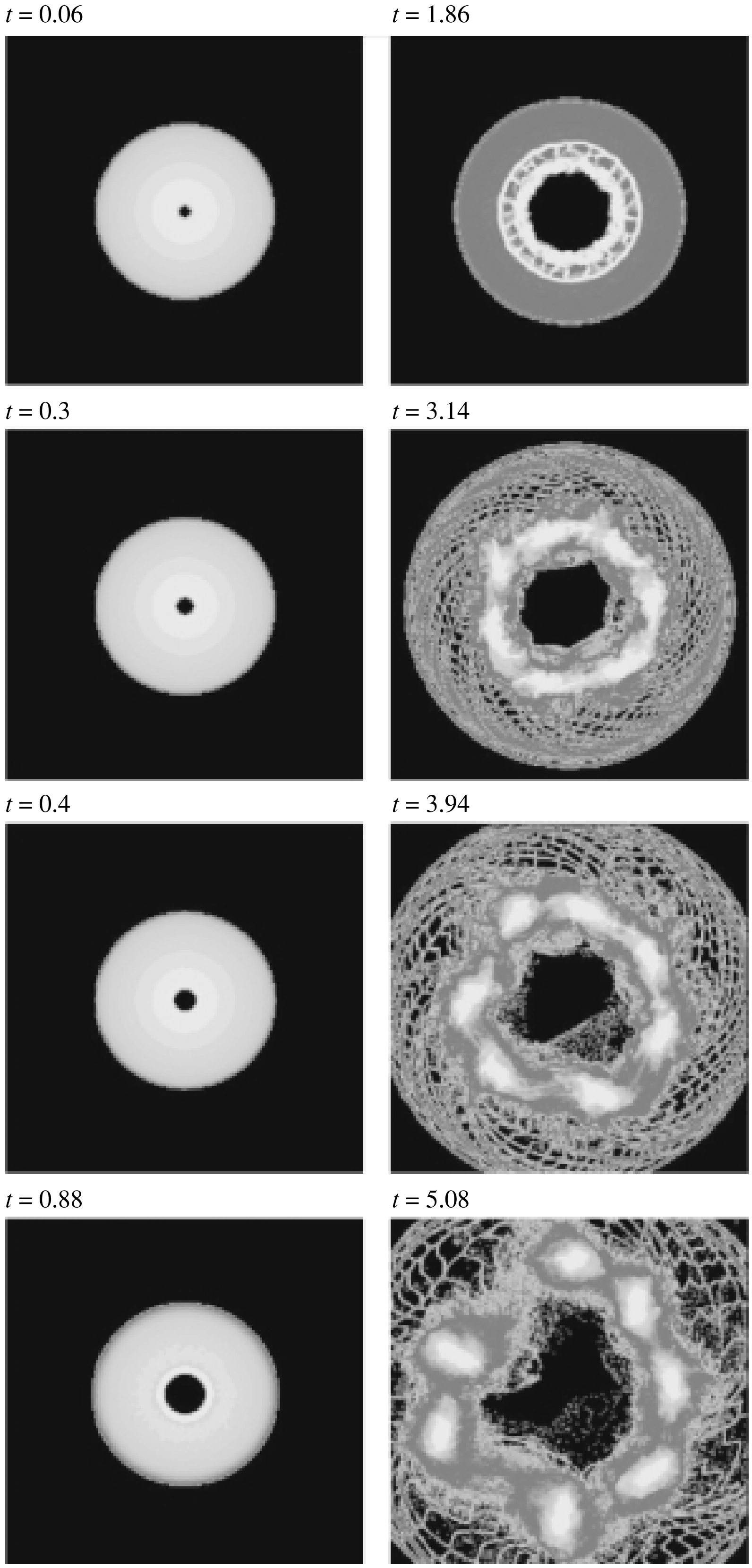

$t = 0.06$

$t = 0.3$

$t = 0.4$

$t = 0.88$

$t = 1.86$

$t = 3.14$

$t = 3.94$

$t = 5.08$

Fig. 1. Evolution of the density distribution when instability grows in a cold disk.

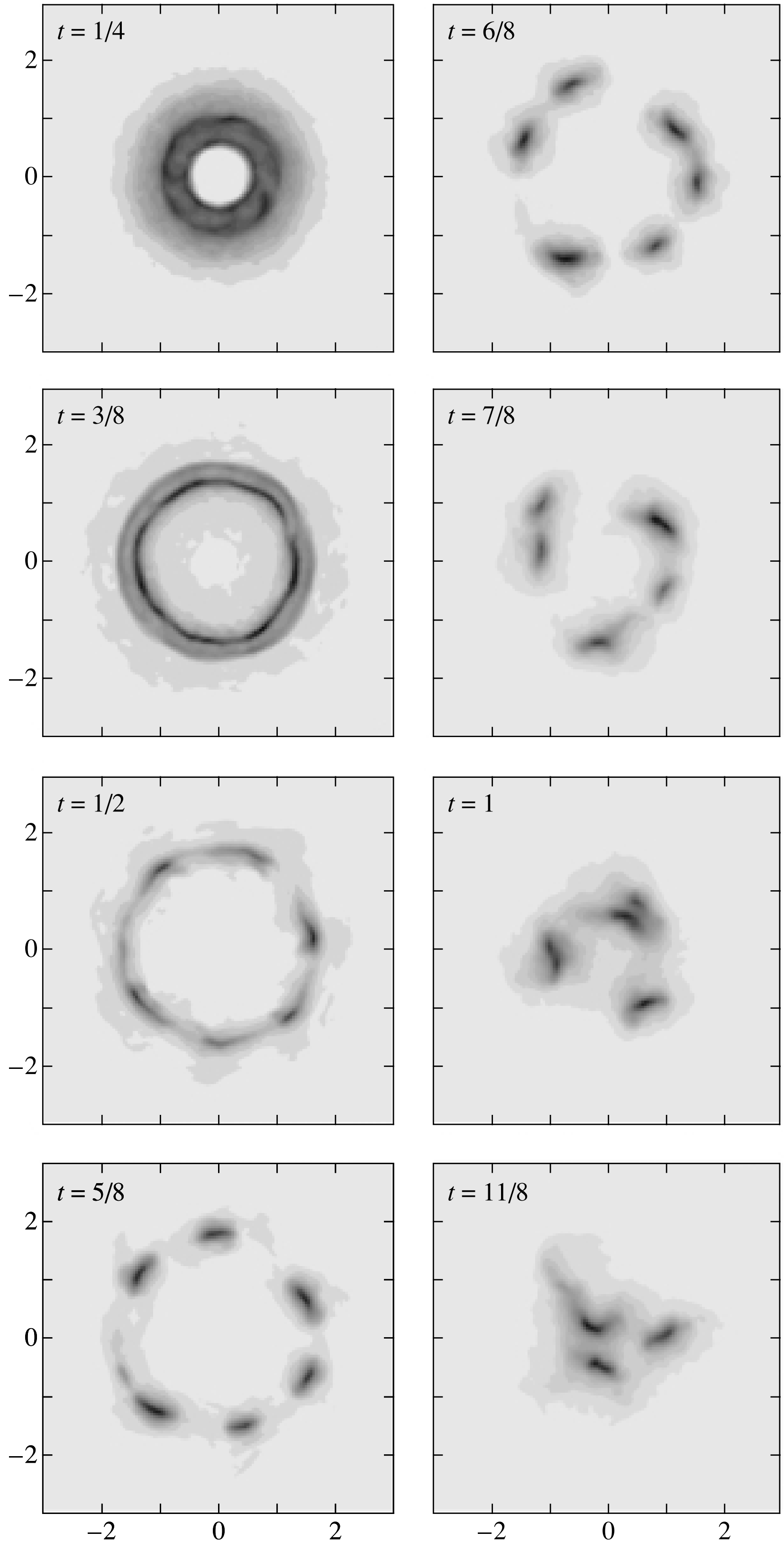

Fig. 2. Evolution of the density in a self-gravitating disk with an initial velocity dispersion $c_r = 1$.

the order of half the rotation) with a distinct self-organization.

When the azimuthally symmetric perturbation begins to cluster, the shortest-wavelength perturbations in the form of a nearly regular cellular structure become visible. The cell size is tens or hundreds of times smaller than R. The cellular structure results from the combination of radial and azimuthal wave perturbations. As the disk expands, the cell size increases; this size becomes larger as the center is approached. The internal space of the cells with a low density is not filled with shorter waves. Clearly, the density-dependent physical constraint on the wavelength of the unstable mode holds in our simulations. The radial dependence of the angular velocity that appears during the evolution leads to multiturn spirality of the structure as a whole.

The spatial step in the numerical algorithm was $h \sim 4 \times 10^{-2} \gg \lambda_{\mathrm{J}}$. The minimum scale of the perturbations reproduced in our numerical simulations by the particle method is determined by the velocity dispersion in the cell and can be on the order of or smaller than the mesh step. The minimum observed scale of $\sim 10^{-2}$ is consistent with the estimate $\lambda_{\mathrm{J}} \sim 2 \times 10^{-8}$.

The growth rate of short-wavelength perturbations with a wavelength much longer than λ_{J} must be large: $\omega \sim 2\Omega\sqrt{\lambda_{\mathrm{T}}/\lambda}$. In particular, for a wavelength on the order of the step of the numerical scheme ($\lambda/\lambda_T \sim 10^{-2}$), instability must grow in a characteristic time of $\sim 10^{-2}$ from the rotation time. We see from the above results that small-scale perturbations show up after a time on the order of one rotation, i.e., at the nonlinear stage of their evolution. The fact that the cellular structure is subsequently self-sustained for a relatively long time, with the conservation laws being satisfactorily obeyed, suggests that there are no detectable countable (nonphysical) instabilities.

A Hot Self-Gravitating Disk Composed of Solid Particles

The nonlinear instability growth stages with structuring are clearly seen for a self-gravitating flat disk composed of solid particles with an initial parameter $c_r = 1$. Figure 2 shows the particle density distributions in the plane of the disk for eight times that differ by 1/8 of the rotation. As follows from the figure, all of the disk matter is collected in several small, interacting dense clusters in times shorter than the rotation period. Increasing the velocity dispersion to $c_r = 3$ leads to disk stabilization in our computations. It should be noted that the Toomre effective parameter, which is defined via the initial density at the center of the disk, was $Q = c_r/c_{\mathrm{T}} = 1.48$ and $Q = 4.45$ for the first and second computations, respectively. According to the results by Miller (1976), the disk stabilization threshold occurs in flat disks without a central mass and a halo in the range of $Q = 3$–4. The results of our other computations of large-scale perturbations in a disk composed of particles are also consistent with Miller's main conclusions. Since the methods of solving the system of equations differ, the close agreement obtained confirms that the numerical simulation codes in these relatively simple cases are correct.

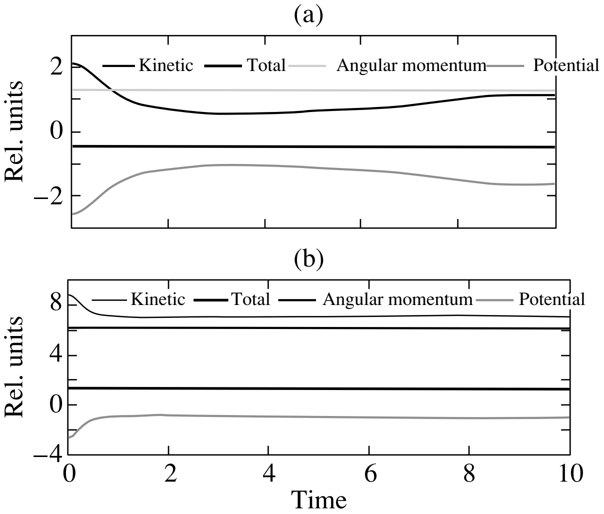

Fig. 3. Variations of the kinetic (a) and gravitational (b) particle energies and the total energy and angular momentum of the system with time.

The total integrated energy, momentum, and other parameters from the fundamental conservation laws for the system under study are known (Vshivkov and Snytnikov 1998) to have certain unremovable fluctuations. These fluctuations are primarily attributable to the discreteness of the time steps. The significant regular deviations of the conserved quantities from their mean values point to the accumulation of numerical errors in our computations. By the accuracy with which the conservation laws are obeyed, we can also judge whether the numerical algorithm is correct. Figure 3 shows variations of the total energy and angular momentum in our numerical computations with time. As we clearly see, energy is conserved at the growth stage of physical instability with an accuracy of better than 1%, while angular momentum is conserved with an accuracy of better than 0.01%.

A Gas–Dust Disk

In order of magnitude, the mass of the gaseous subsystem in the disk can account for one half of the visible mass of the galactic disk or the bulk of

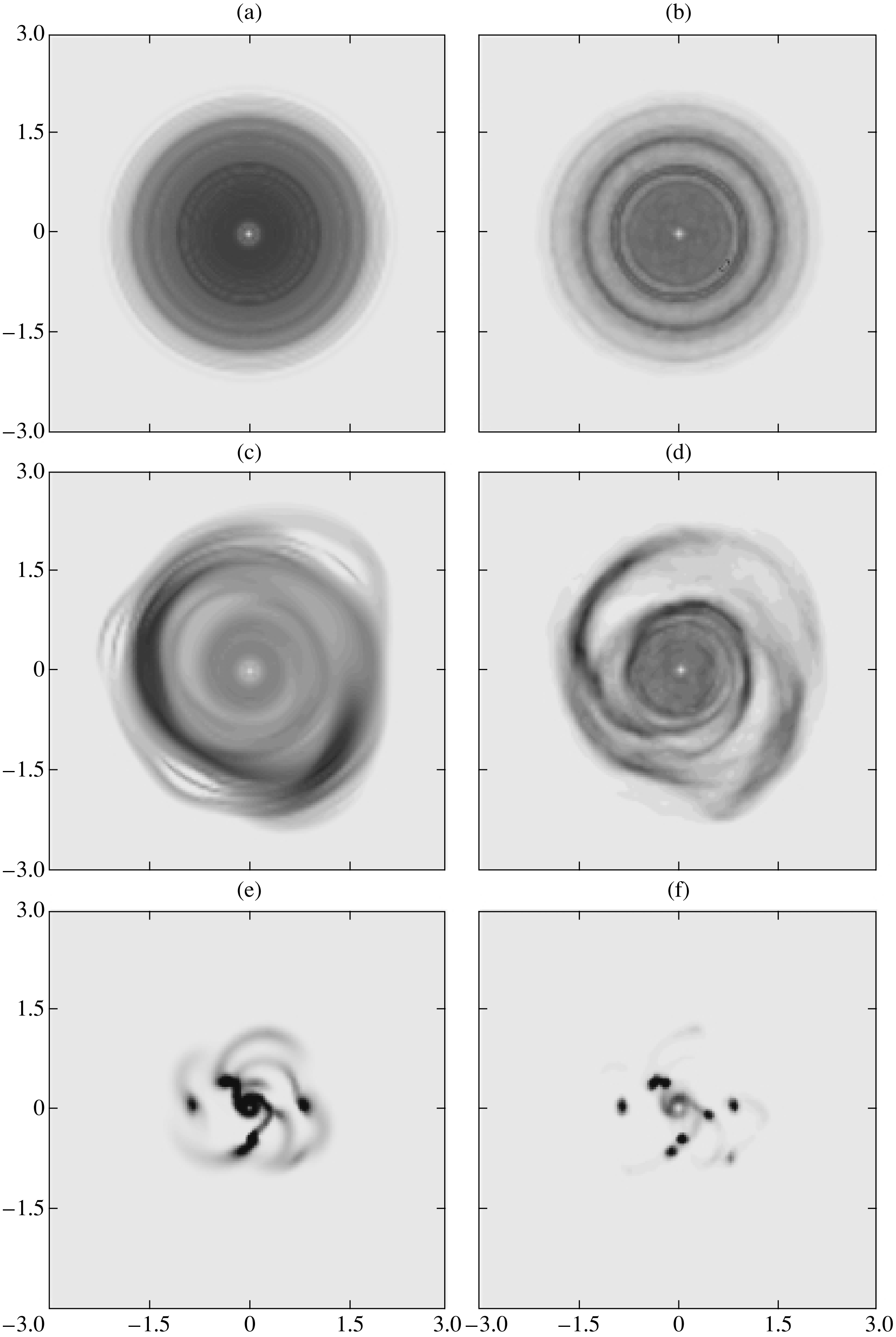

Fig. 4. Rings, spirals, and density clusters in a gas–dust disk: (a), (c), and (e) particles; (b), (d), and (f) gas.

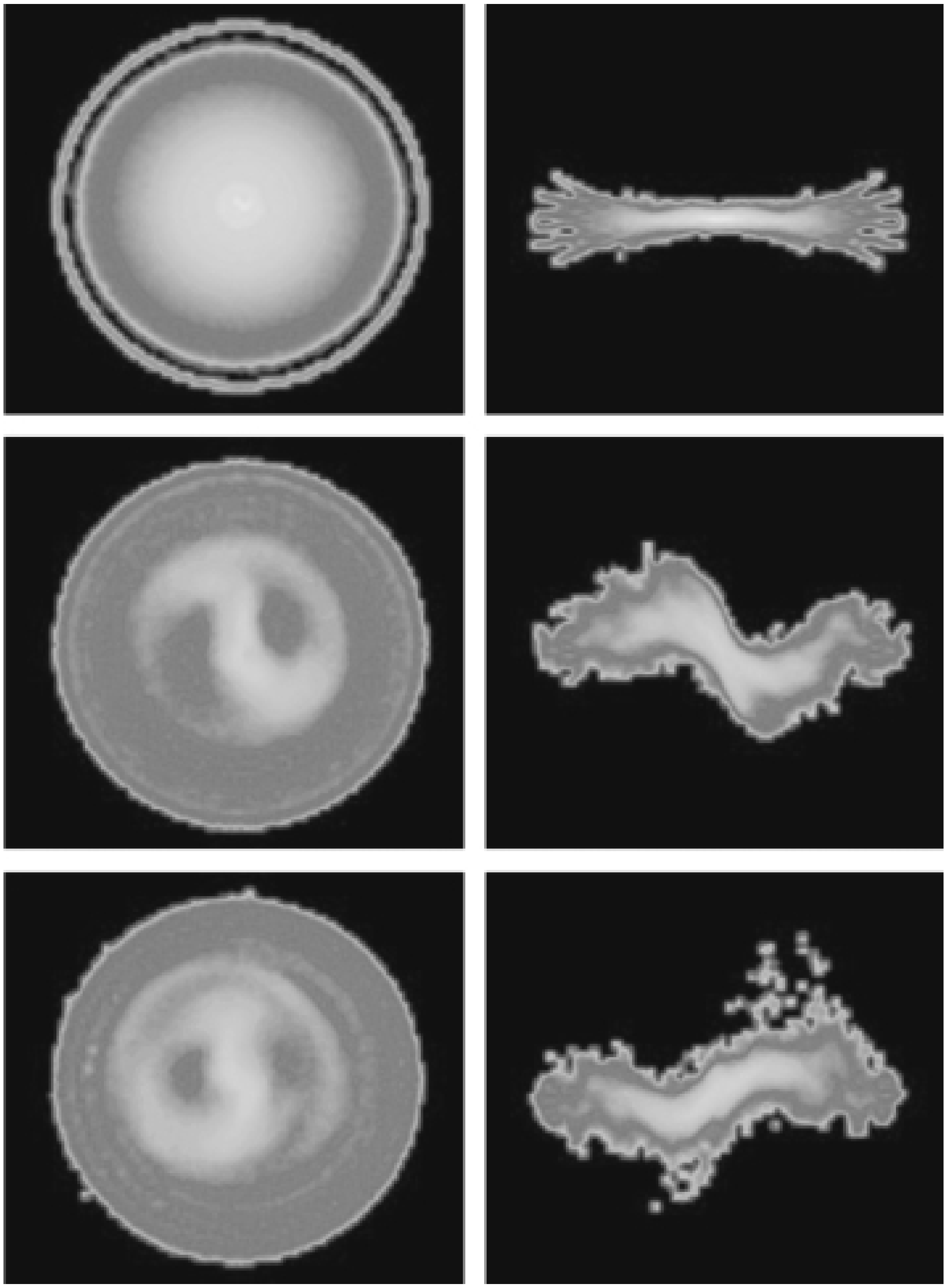

Fig. 5. Equatorial and meridional density distributions for a three-dimensional disk with $c_r/c_f = 3$.

the mass of the circumstellar disk. Therefore, the dynamics of the matter in disks depends on the parameters that describe the gaseous subsystem. As we showed in our previous computations (Snytnikov *et al.* 2002a, 2002b), an azimuthally periodic structure manifests itself in the gas distribution. This structure suggests that the evolution and self-organization in a two-component system with a self-consistent field can differ significantly from those in a one-component disk.

Figure 4 shows the types of structuring for a two-component disk by the time $t = 5$ in a quasi-three-dimensional model with a central mass. Figures 4a, 4c, and 4e refer to the subsystem of massive particles, while Figs. 4b, 4d, and 4f refer to the gas for the same parameters. We found three main types of structuring of the gas–dust disk, depending on the combination of parameters $M_{\rm s}$, $M_{\rm g}$, $M_{\rm p}$, and δv_r. The ringlike structures by the type of instability in axisymmetric models belong to the first type (Figs. 4a and 4b: $M_{\rm s} = 1$, $M_{\rm g} = 0.5$, $M_{\rm p} = 0.01$, $\delta v_r = 0.1$). The structures of the second type have the shape of spiral density waves typical of galaxies (Figs. 4c and 4d: $M_{\rm s} = 1$, $M_{\rm g} = 0.2$, $M_{\rm p} = 0.01$, $\delta v_r = 0.1$). The third type is related to the formation of a small number of relatively dense clusters of particles and gas (Figs. 4e and 4f: $M_{\rm s} = 2$, $M_{\rm g} = 1$, $M_{\rm p} = 1$, $\delta v_r = 1$), which suggests possible scenarios for the initial formation of protoplanets at the stage when there is no massive central body any longer. In these cases, the main problem of the simulations is to find similarity parameters that govern the behavior of complex gravitating systems.

A Hot Disk with Vertical Particle Motion

Our computations with the initial equilibrium conditions from Khoperskov *et al.* (2003) indicate that a disk composed mostly of a collection of particles is in a quasi-steady state. Figure 5 shows the results of our computations of the three-dimensional model with the following initial parameters of the disk:

Disk radius = 1;
Disk mass = 1;
Density scale $L = 0.2$;
Mass of central body = 0;
Halo mass = 0.1;
Halo radius = 0.1;
Spatial parameter of halo particle distribution $a = 1$;
Bulge mass = 0.1;
Bulge radius = 0.1;
Spatial parameter of bulge particle distribution $b = 1$;
Velocity dispersion ratio $c_r/c_\varphi = 3$;
Vertical velocity dispersion $c_z = 0.2$.

These parameters correspond to one of the computations by Khoperskov *et al.* (2003), except for the tripled velocity dispersion ratio c_r/c_φ. We see that the disk is quasi-stable for a certain time ($t = 17$, the density distributions in the disk plane and the vertical plane are on the left and the right, respectively). Subsequently, a large-scale membrane-type perturbation in the form of a single-wave warp of the disk plane develops ($t = 155$). Simultaneously, a bar is formed. The subsequent evolution does not lead to a breakup of the disk or to a significant change in its sizes in accordance with the assumption about its self-sustenance through the choice of initial conditions. In particular, the membrane oscillation amplitude decreases ($t = 216$). The appearance of separate microparticles that escape from the disk plane and then again return to it (the evaporation of stars) arouses considerable interest.

We also performed computations for $c_r/c_\varphi = 1$, which more closely corresponds to the conditions of stationary behavior of the system being simulated. In this case, the perturbations described for $c_r/c_\varphi = 3$ are less pronounced.

CONCLUSIONS

To study the problem of the growth of gravitational instability in a rotating two-phase medium with the achievement of nonlinear stages, it was necessary to develop an appropriate numerical method. This numerical method was developed for the fundamentally nonstationary three-dimensional problem with the gas-dynamical equations for a gaseous subsystem, with the Vlasov–Liouville equation for the phase density function of seven variables, and with the Poisson equation for a self-consistent gravitational field with free moving boundaries. The integration of the seven-dimensional Vlasov–Liouville equation was and is possible only by the method of large particles. The computational experiments aimed at studying the physical instabilities suggested the existence of unstable modes that exponentially grew with time in the linear approximation. Therefore, the fundamental Lax theorem on the numerical solution of systems of equations of mathematical physics, which requires the approximation and stability of the numerical method to ensure convergence, could not be applied to the problem under consideration, because the numerical method for studying the physical instability in the linear approximation must be fundamentally unstable. A possible way out was found through the development of a special numerical method in which the basic equations were approximated, convergence was achieved, and all of the fundamental (mass, momentum, angular momentum, energy, and phase volume) conservation laws were obeyed. However, from the viewpoint of the conservation laws, there has been the following problem for the method of large particles since the 1960s: this method in the existing form either conserved angular momentum and violated the energy conservation law or vice versa. In practice, either one or the other of its modifications was used, depending on the problem. The problem of gravitational dynamics requires that all of the conservation laws be obeyed; they are equally important. As we showed in this paper, the required numerical models can be developed. We determined approaches to the mathematical simulations of collisionless gravitational dynamics with a self-consistent field. Based on the studies, we constructed a three-dimensional numerical model designed to investigate nonstationary processes in gravitating N-body systems, including those with gas.

ACKNOWLEDGMENTS

We wish to thank V.N. Parmon and A.M. Fridman for interest, support, and discussion of the results. This work was supported in part by the Russian Foundation for Basic Research (project no. 02-01-00864), NASA JURRISS NAG-5-8717, the

Siberian Branch of the Russian Academy of Sciences (integration project no. 148, 2003), and the Program of the Presidium of the Russian Academy of Sciences (2003).

REFERENCES

1. V. S. Avedisov, http://nut.inasan.rssi.ru/Piter/May_Colloq_Abstracts.html (1998).
2. J. E. Barnes and P. Hut, Nature **324**, 446 (1986).
3. O. M. Belotserkovskii and Yu. M. Davydov, *The Large-Particle Method in Gas Dynamics* (Nauka, Moscow, 1995) [in Russian].
4. Yu. B. Berezin and V. A. Vshivkov, *The Particle Method in Rarefied-Plasma Dynamics* (Nauka, Novosibirsk, 1980) [in Russian].
5. G. Bertin, *Dynamics of Galaxies* (Cambridge Univ. Press, 2000), p. 414.
6. G. Bertin and C. C. Lin, *Spiral Structure in Galaxies: A Density Wave Theory* (MA MIT Press, Cambridge, 1996).
7. T. M. Eneev, N. N. Kozlov, and R. A. Sunjaev, Astron. Astrophys. **22**, 41 (1973).
8. F. Hohl and R. W. Hockney, J. Comput. Phys. **4**, 306 (1969).
9. A. V. Khoperskov, A. V. Zasov, and N. V. Tyurina, Astron. Zh. **80**, 387 (2003) [Astron. Rep. **47**, 357 (2003)].
10. C. C. Lin, C. Yuan, and F. H. Shu, Astrophys. J. **155**, 721 (1969).
11. J. Makino, J. Comput. Phys. **87**, 148 (1990).
12. R. H. Miller, J. Comput. Phys. **21**, 400 (1976).
13. V. L. Polyachenko and A. M. Fridman, *Equilibrium and Stability of Gravitating Systems* (Nauka, Moscow, 1976) [in Russian].
14. V. C. Safronov, *Evolution of the Protoplanetary Cloud and the Origin of Earth and Planets* (Nauka, Moscow, 1969) [in Russian].
15. J. A. Sellwood, J. Comput. Phys. **50**, 337 (1983).
16. J. A. Sellwood, Rutgers Astrophys. Preprint No. 256 (1999).
17. V. N. Snytnikov, V. A. Vshivkov, G. I. Dudnikov, *et al.*, Vychisl. Tekhnol. **7**, 72 (2002).
18. V. N. Snytnikov, G. I. Dudnikova, J. T. Gleaves, *et al.*, Adv. Space Res. **30**, 1461 (2002).
19. A. Toomre, Astrophys. J. **139**, 1217 (1964).
20. V. A. Vshivkov and V. N. Snytnikov, Zh. Vychisl. Mat. Mat. Fiz. **38**, 1877 (1998) [Comput. Math. Math. Phys. **38**, 1811 (1998)].

Translated by V. Astakhov

Astronomy Letters, Vol. 30, No. 2, 2004, pp. 65–72. Translated from Pis'ma v Astronomicheskiĭ Zhurnal, Vol. 30, No. 2, 2004, pp. 83–91.
Original Russian Text Copyright © 2004 by Chugai, Yungelson.

Type-Ia Supernovae in Dense Circumstellar Gas

N. N. Chugai* **and L. R. Yungelson****

Institute of Astronomy, Russian Academy of Sciences, ul. Pyatnitskaya 48, Moscow, 119017 Russia

Received July 16, 2003

Abstract—We propose a model for the bolometric light curve of a type-Ia supernova (SN Ia) that explodes in a dense circumstellar (CS) envelope. Our modeling of the light curves for SN 2002ic and SN 1997cy shows that the densities of the CS envelopes around both supernovae at a radius of $\sim 7 \times 10^{15}$ cm are similar, while the characteristic ejection time for this envelope around SN 1997cy does not exceed 600 yr. We analyze two possible evolutionary scenarios that could lead to the explosion of a SN Ia inside a dense CS hydrogen envelope: accretion onto a CO white dwarf in a symbiotic binary and the evolution of a single star with an initial mass of about $8M_{\odot}$. If the hypothesis of a SN Ia explosion in a dense CS envelope is correct for SN 2002ic and SN 1997cy, then we must assume that the the rapid loss of the red-supergiant envelope in several hundred years and the subsequent explosion of the CO white dwarf are synchronized by some physical mechanism. This mechanism may be related to the contraction of the white dwarf as it approaches the Chandrasekhar limit. We show that the formation of a (super-)Chandrasekhar mass due to the merger of a CO white dwarf and the CO core of a red supergiant followed by a supernovae explosion is unlikely, since this mechanism does not provide the required synchronization of the rapid mass loss and the explosion.

Key words: *supernovae and supernova remnants.*

1. INTRODUCTION

Recently, based on the spectra and light curve of the supernova SN 2002ic with narrow Hα emission, Hamuy *et al.* (2003) have concluded that this object is a type-Ia supernova (SN Ia) interacting with a dense circumstellar (CS) envelope. Moreover, these authors believe that another supernova, SN 1997cy, classified as SN IIn (i.e., a supernova with narrow Hα emission) is an analogue of SN 2002ic. The narrow unresolved Hα line originates in the photoionized dense CS gas, while the broad Hα component with a full width at half maximum ≈ 1800 km s^{-1} is identified with the emission from shocked dense CS clouds. According to Hamuy *et al.* (2003), the dense CS envelope is the result of intense mass loss from the envelope of the red supergiant. The latter may be either a member of a symbiotic binary with an accreting white dwarf or the presupernova itself if the supernova originates from a single intermediate-mass star in the SN 1.5 scenario (Iben and Renzini 1983).

The luminosity of SN 2002ic is relatively high for SN Ia and is attributed to the interaction with dense CS gas (Hamuy *et al.* 2003). Remarkably, the light curve of SN 1997cy has already been modeled in terms of the CS interaction (Turatto *et al.* 2000). However, in the latter study, SN 1997cy was assumed to be a hypernova with an enormous energy of 3×10^{52} erg and a large mass of $25M_{\odot}$. Of course, the hypernova model is in conflict with the hypothesis of the nature of SN 1997cy (Hamuy *et al.* 2003).

On the other hand, it has been shown recently that the hypernova model is by no means necessary to account for the bolometric light curve of SN 1997cy; the CS interaction of a normal supernova with a typical energy of 10^{51} erg and a low mass of $1.5M_{\odot}$ can successfully explain this phenomenon (Chugai and Danziger 2003). This result, along with the spectral evidence for the explosion of SN 1997cy as SN Ia (Hamuy *et al.* 2003), forces us to consider the explosion of SN Ia inside a dense CS envelope as a promising hypothesis.

Although it is not yet quite clear how the spectrum of SN Ia was formed in the case of strong CS interaction, it makes sense to study the density and the structure of the CS envelope using constraints imposed by the bolometric light curve. Here, we model the light curves of both supernovae by assuming that their radiation is a combination of the radioactive luminosity of SN Ia and the luminosity powered by the interaction of the supernova with the dense CS environment. Our results are then discussed in terms of the various evolutionary scenarios that presumably led to SN 2002ic and SN 1997cy.

---

*E-mail: `nchugai@inasan.rssi.ru`
**E-mail: `lry@inasan.rssi.ru`

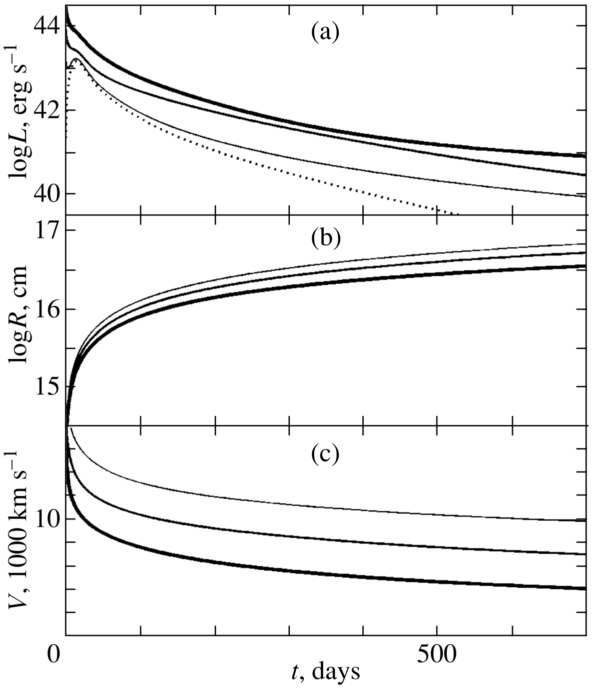

Fig. 1. Bolometric light curves (a), the radius of the thin shell (b), and its velocity (c) for the model of SN Ia expansion in the stellar wind. The light curve for SN Ia without wind is indicated by the dotted line. The thickness of the lines (from thinnest to thickest) corresponds to wind-density parameters w of 4×10^{15}, 2×10^{16}, and 10^{17} g cm^{-1}, respectively.

2. THE MODEL LIGHT CURVE

Let us assume that SN Ia explodes inside a spherically symmetric CS envelope. We are interested in the bolometric light curve produced by the superposition of the intrinsic radioactive luminosity of SN Ia and of the luminosity powered by interaction with the CS matter. To compute the light curve, we use the model that was used for the light curve of SN 1998S (Chugai 2001). In this model, the interaction dynamics is calculated in the thin-shell approximation that treats the region between the forward and reverse shock waves as an infinitely thin shell (Chevalier 1982). The supernova envelope is characterized by the mass (M), kinetic energy (E), and presupernova radius (R_0). We assume that the initial kinematics of the supernova envelope is free expansion ($v \propto r$), and that the density distribution in this envelope is exponential, $\rho \propto \exp(-v/v_0)$, where v_0 is defined by E and M. Below, we take $M = 1.4 M_\odot$, $E = 1.5 \times 10^{51}$ erg, and a ^{56}Ni mass of $0.7 M_\odot$. This choice is consistent with the SN Ia delayed detonation models with maximum ^{56}Ni mass (Höflich *et al.* 1995).

The numerical solution of the equation of motion for the thin shell yields the evolution of the shell radius and velocity. The resulting kinetic luminosities of the forward and reverse shock waves are transformed into the X-ray luminosities using the cooling rates of the post-shock gas with a normal chemical composition (Chugai 1992). The X-ray radiation of both shocks with the corresponding temperatures is partially absorbed by the supernova envelope, the thin shell, and the CS gas. The total absorbed X-ray luminosity is identified with the bolometric luminosity powered by the interaction. This simple model disregards the details of the optical spectrum formation and cannot describe the emergent spectrum in detail.

The light curve powered by the radioactive decay ^{56}Ni—^{56}Co—^{56}Fe can be calculated using the analytical theory for a homogeneous envelope (Arnett 1980). To compute the total energy deposition rate, we assume that ^{56}Ni is mixed in the inner $0.8 M_\odot$. The interaction of gamma rays with the matter is treated in the single-flight approximation by assuming an absorption coefficient of 0.03 cm^2 g^{-1}. The opacity is taken to be 0.15 cm^2 g^{-1}.

The computed bolometric curves of SN Ia with and without CS interaction, assuming a wind with a constant mass-loss rate ($\rho \propto r^{-2}$), are shown in Fig. 1. The density parameter $w = 4\pi r^2 \rho$ for the models in Fig. 1 is 4×10^{15}, 2×10^{16}, and 10^{17} g cm^{-1}, respectively. For a wind velocity of 10 km s^{-1}, these values correspond to mass-loss rates of 6×10^{-5} $M_\odot$ yr^{-1}, 3×10^{-4} $M_\odot$ yr^{-1}, and 1.5×10^{-3} $M_\odot$ yr^{-1}. Figure 1 shows that the contribution of the interaction to the SN Ia luminosity at maximum light is significant for $w > 10^{16}$ g cm^{-1}, while the contribution of the interaction with a more rarefied wind, $w \sim 10^{16}$ g cm^{-1}, can be detected only at a very late epoch ($t > 1$ yr). Amazingly, at a late epoch ($t \sim 300$ days), the interaction luminosity for a low CS density depends on w more strongly than that for a high CS density; i.e., there is a saturation effect. This is because for low w, the luminosity is determined primarily by the radiative reverse shock wave, while the contribution of the adiabatic forward shock increases with w. For high w, the forward shock wave becomes radiative and dominant, so the total luminosity turns out to be $L \propto w v_s^3$ (where v_s is the thin-shell velocity). In this case, the luminosity obviously increases less rapidly than w, since the velocity v_s decreases appreciably with increasing w.

Above, we considered only a stationary wind. However, the shape of the light curve powered by the CS interaction depends on the density distribution in the CS envelope. Below, we take into account this fact in modeling the light curves of SN 2002ic and SN 1997cy.

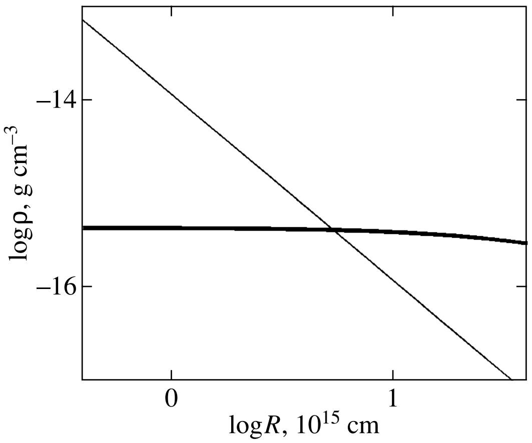

Fig. 2. Density distributions in models ic1 (thick line) and ic2 (thin line).

3. THE LIGHT CURVES OF SN 2002ic AND SN 1997cy AND THEIR CS ENVELOPES

The BVI light curves spanning a 70-day interval are available for SN 2002ic. To restore the monochromatic light curves using our model bolometric light curve requires specifying the photosphere radius (R_p). We assume that the photosphere coincides with the thin shell, i.e., $R_\mathrm{p} = R_\mathrm{s}$. This coincidence is justified for SN 1998S (SN IIn), where an opaque thin shell is formed at the SN/CSM interface (Chugai 2001). However, for SN 2002ic, this assumption should be considered as approximate, since the spectrum exhibits no smooth continuum characteristic of SN 1998S. Taking $R_\mathrm{p} = R_\mathrm{s}$ and using the computed bolometric luminosity, we derive the effective temperature and then obtain the absolute BVI magnitudes by assuming a blackbody spectrum. To compare the model with observations, we take the redshift $z = 0.067$, the reddening $E(B - V) = 0.073$ (Hamuy *et al.* 2003), and the Hubble constant $H_0 = 70$ km s^{-1} Mpc^{-1}. The K-correction related to the redshift is small and was calculated by assuming a blackbody spectrum with a temperature of $T = 10\,000$ K. We take the supernova explosion date to be 2452585 JD.

The BVI light curves for SN 2002ic are computed for a wide range of parameters. The general conclusion is that a stationary wind $\rho \propto r^{-2}$ (model ic2) results in a steep brightness decline that disagrees with observations. Better agreement is provided by model ic1 with a flat density distribution (Fig. 2). The light curves for both models are shown in Fig. 3. Although we focus our attention on modeling the V light curve, which has pre-maximum observational points, the agreement in the other bands is also satisfactory. In the I band, the accuracy of the fit for model ic2 is better than 0.2 mag. The deviations are largest in the B band, although the general behavior of the observed flux is reproduced quite satisfactorily. The bolometric light curves for both models are shown in Fig. 4. It shows that the CS interaction contributes about 50% at maximum light and dominates after the maximum. This conclusion is qualitatively consistent with the decomposition of the light curve for SN 2002ic by Hamuy *et al.* (2003). For the interaction to be prominent at maximum light, the CS envelope must be dense at a radius of $r \sim 2 \times 10^{15}$ cm. At an expansion velocity of $u \sim 10$ km s^{-1}, the age of this matter is $r/u \sim 70$ yr; i.e., the supernova must explode no later than $\sim 10^2$ yr after the termination of the major mass-loss episode.

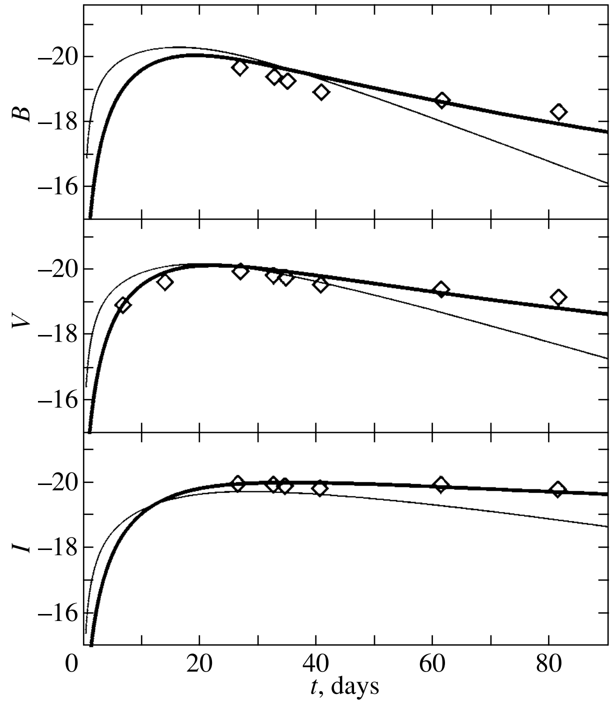

Fig. 3. BVI light curves for SN 2002ic. The thick and thin lines represent models ic1 and ic2, respectively. The observational data (Hamuy *et al.* 2003) are indicated by diamonds.

Some uncertainty in choosing the photospheric radius may affect the derived CS density. To check the effect of this uncertainty, we calculated the monochromatic light curves of SN 2002ic by assuming that $R_\mathrm{p} = 0.8R_\mathrm{s}$. The best fit is obtained for a CS density that is 10% higher than that for model ic1. This shows that the derived CS density is not very sensitive to the assumed photospheric radius.

The lack of photometric data for SN 2002ic at a late epoch (>70 days) does not allow us to derive the CS density at distances larger than $\approx 7 \times 10^{15}$ cm. Within this radius, the total mass of the CS envelope is $\approx 0.4 M_\odot$.

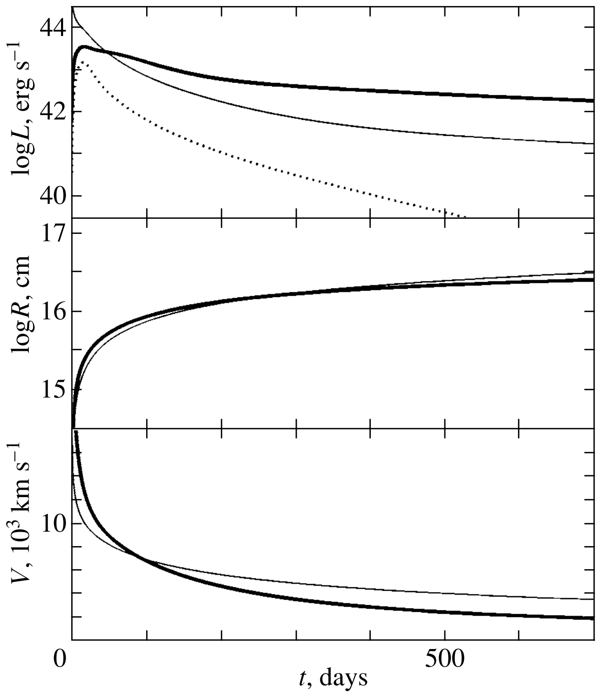

Fig. 4. Bolometric light curves, radius, and velocity of the thin shell for models ic1 (thick line) and ic2 (thin line). The dotted line indicates the light curve of SN Ia in the absence of CS gas.

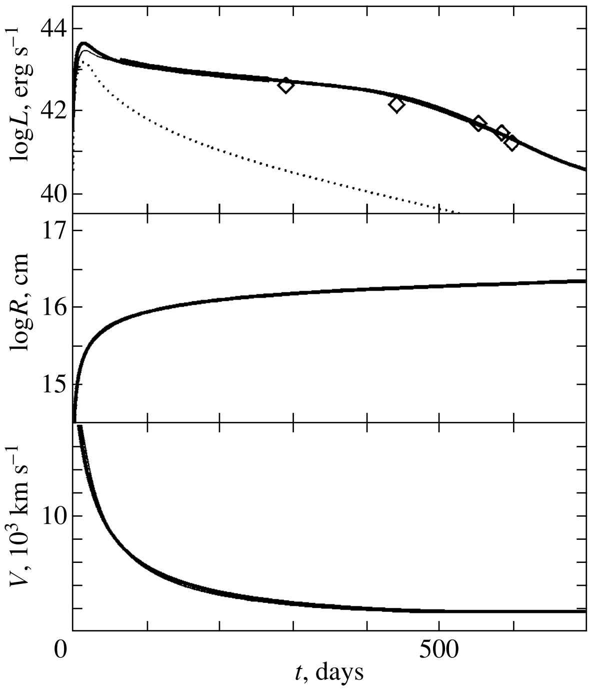

Fig. 5. Bolometric light curves, radius, and velocity of the thin shell for models cy3 (thick line) and cy4 (thin line). The dashed line indicates the light curve of SN Ia without CS gas. In the upper panel, the diamonds and the thick line indicate the empirical light curve (Turatto *et al.* 2000) assuming $H_0 = 70$ km s^{-1} Mpc^{-1}.

For SN 1997cy, the light curve was observed over 600 days after the outburst (Turatto *et al.* 2000). The bolometric light curve of SN 1997cy published by Turatto *et al.* (corrected for our assumed $H_0 = 70$ km s^{-1} Mpc^{-1}) is shown in Fig. 5. This figure also presents our simulated light curves for models cy3 and cy4 with the CS density profiles shown in Fig. 6. Model cy3 has the same density distribution as model ic1 for SN 2002ic, except that the density is 10% higher in model cy3. Model cy4 with an inner density minimum shows a similar fit to the light curve as does model cy3, thereby demonstrating the uncertainty in choosing the CS density distribution in the inner region. Nevertheless, we note that the CS densities around SN 1997cy and SN 2002ic are roughly similar at radii of $\sim$7 $\times 10^{15}$ cm.

The steepening of the light curve after day 500 indicates a drop in CS density at a radius of $r = R_{\rm b} \approx 2 \times 10^{16}$ cm (Fig. 6). The total mass of the CS envelope is $M_{\rm cs} = 5.4\ M_\odot$ for model cy3 and $5.9 M_\odot$ for model cy4. The derived CS mass for SN 1997cy is close to that found previously in the low-mass supernova model (Chugai and Danziger 2003). More remarkably, the mass of the CS envelope obtained by Turatto *et al.* (2000) in their hypernova model is also virtually the same ($\approx 5\ M_\odot$).

The age of the dense CS envelope around SN 1997cy is $t_{\rm cs} = R_{\rm b}/u = 630/u_1$ yr, where u_1 is the flow velocity in units of 10 km s^{-1}. Therefore, the average mass-loss rate is

$$\dot{M} = M_{\rm cs}/t_{\rm cs} = 8 \times 10^{-3} \left(\frac{M_{\rm cs}}{5\ M_\odot}\right) u_1 \quad M_\odot\ {\rm yr}^{-1}. \tag{1}$$

Since the velocity of the superwind is generally 10–20 km s^{-1} (Wood 1993), the average mass-loss rate for the presupernova of SN 1997cy assuming a CS mass of $5 M_\odot$ is $\dot{M} \sim 10^{-2}\ M_\odot$ yr^{-1}. Remarkably, given the similar density of the CS envelope around SN 2002ic, the estimated average mass-loss rate is also characteristic of this event.

Let us now check whether the derived CS density distribution around SN 1997cy agrees with the luminosity of this supernova in narrow Hα emission. The emission measure of the CS envelope in model cy3 on day 70 is $6.4 \times 10^{65} x^2$ cm^{-3} (where x is the degree of hydrogen ionization). Taking an electron temperature of 10^4 K, the predicted Hα recombination luminosity in the Menzel case B is $\approx$2 $\times 10^{41} x^2$ erg s^{-1}. Turatto *et al.* (2000) distinguished three components—narrow, intermediate, and broad—in the Hα profile on day 70. However, the relative contribution of each component was not reported. To minimize the uncertainty related to the broad component, which is affected by the blend of Fe II lines, we consider only the intermediate and narrow components within the range of radial velocities $|v_r| < 2000$ km s^{-1}. The latter is also the velocity range of the broad Hα component in SN 2002ic (Hamuy *et al.* 2003). The spectrum of SN 1997cy on day 70 (Turatto *et al.* 2000) provides a rough luminosity estimate for these two components, $L \sim 5 \times 10^{40}$ erg s^{-1}. According to the data on SN 2002ic obtained by Hamuy *et al.* (2003), we assume that the contributions of the narrow and intermediate (i.e., broad in SN 2002ic) components are comparable. Under this assumption, the luminosity of the narrow component in SN 1997cy is $\sim$2.5 $\times 10^{40}$ erg s^{-1}. Taking into account the above luminosity estimated from the emission measure, we conclude that the average degree of ionization in the CS envelope is $x \sim 0.35$. This value suggests that the Thomson optical depth of the CS envelope is $\tau_{\rm T} \approx 0.5$.

The luminosity of SN 2002ic in the narrow Hα line during the entire observed period ($t \leq 70$ days) is virtually constant and equal to $\approx$2 $\times 10^{40}$ erg s^{-1} (Hamuy *et al.* 2003). Thus, the luminosities of both supernovae in this line are approximately equal at the epoch of 70 days. This fact along with the similarity between the CS densities at $r \sim 7 \times 10^{15}$ cm strongly suggests that for SN 2002ic the structure of the CS envelope and its total mass are approximately the same as those of SN 1997cy; i.e., the mass of the CS envelope of SN 2002ic is probably also several solar masses.

4. THE NATURE OF THE PRESUPERNOVA

An important common property of the progenitors of both SN 2002ic and SN 1997cy is the unusually high mass-loss rate, $\dot{M} \sim 10^{-2}\ M_\odot$ yr^{-1}, for several hundred years before the explosion. This points to the existence of a mechanism that synchronizes the phase of violent mass loss with the epoch of supernova explosion. If SN 2002ic and SN 1997cy are actually SNe Ia, then it would be natural to assume that the violent mass loss is related to the epoch when the CO white dwarf reaches the Chandrasekhar mass ($M_{\rm Ch}$).

Following the hypothesis of Hamuy *et al.* (2003), we consider two scenarios that can, in principle, lead to the explosion of SNe Ia inside a hydrogen-rich circumstellar envelope: (i) the explosion of an accreting white dwarf in a binary system with a red supergiant companion to the white dwarf (Whelan and Iben 1973) and (ii) the explosion of the degenerate CO core of a single star (Arnett 1969; Iben and Renzini 1983).

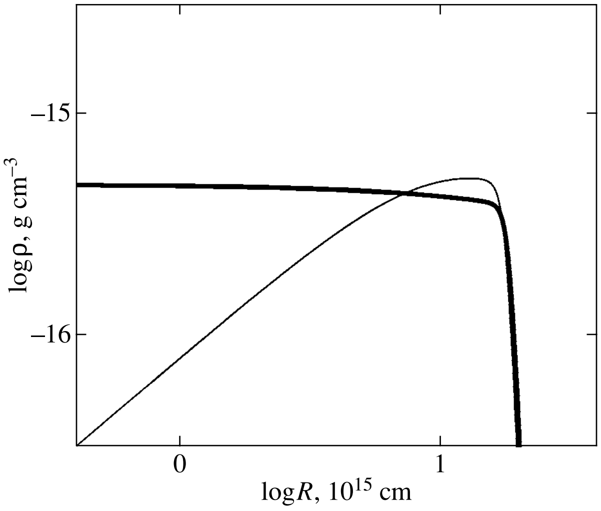

Fig. 6. Density distributions in models cy3 (thick line) and cy4 (thin line).

4.1. A Binary System

The model of a binary system suggests that a CO white dwarf reaches the Chandrasekhar mass through accretion from a red giant or supergiant companion. Since the red-supergiant mass-loss rate through the superwind does not exceed $3 \times 10^{-4}\ M_\odot$ yr^{-1} (Wood 1994), very unusual conditions are required for the mass-loss rate to reach $10^{-2}\ M_\odot$ yr^{-1}. The required mass-loss rate, as well as the synchronization of the explosion with the stage of intense mass loss, could be qualitatively explained in terms of the following two possible scenarios of events in a binary.

In the first scenario, the mass–radius relation for white dwarfs steepens as the Chandrasekhar limit is approached. For $M \approx M_{\rm Ch}$, a small increase in the mass of the dwarf is accompanied by a significant decrease in its radius. Moreover, a considerable fraction of the outer layers of a CO dwarf may burn into ^{22}Ne through nuclear burning in the vicinity of the temperature maximum; this may also lead to a decrease in the radius of the dwarf immediately before the explosion on a time scale of several hundred years. The decrease in the radius of the white dwarf will result in its spin-up. The rapid rotation and the strengthening of the magnetic field due to the differential rotation in combination with the increase in gravitational potential at the surface of the white dwarf will cause an increase in the kinetic luminosity of the wind from the innermost parts of the accretion disk. We assume that, by analogy with the winds from white dwarfs (Hachisu *et al.* 1999), the interaction of this wind with the envelope of the red supergiant may cause an intense mass loss by the latter. This effect was considered by Hachisu *et al.* (1999) as a mechanism for the loss of orbital angular momentum. Here, we are interested in the supergiant mass loss alone.

Let the mass and radius of the white dwarf be M_1 and R_1 and those of the red supergiant be M_2 and R_2, respectively. Assuming that the velocity of the white-dwarf stellar wind is on the order of the escape velocity (maximum estimate) and that the velocity of the gas lost by the red supergiant is also on the order of the escape velocity, we obtain an estimate for the typical mass-loss rate by the red supergiant from the condition of balance between the energy fluxes (ablation):

$$\dot{m}_2 = f(q)\dot{m}_1 \left(\frac{M_1}{M_2}\right) \left(\frac{R_2}{R_1}\right), \tag{2}$$

where $\dot{m}_1$ is the mass-loss rate via the fast wind of the white dwarf, $f(q)$ is the geometrical factor calculated by Hachisu *et al.* (1999), and $q = M_2/M_1$. Given the estimated mass of the CS envelope, we take $q \approx 4$. For $f(q)$, we take $f \approx 0.033$ by assuming that the red giant fills its Roche lobe (Hachisu *et al.* 1999). Substituting these values into Eq. (2) and adopting $R_2 = 1000\ R_\odot$, $R_1 = 3 \times 10^{-3}\ R_\odot$, and $\dot{m}_1 = 10^{-5}\ M_\odot\ \mathrm{yr}^{-1}$ (which corresponds to the Eddington limit of the accretion luminosity), we obtain $\dot{m}_2 \approx 10^{-2}\ M_\odot\ \mathrm{yr}^{-1}$. Thus, the model is capable of providing the required red giant mass-loss rate. However, it should be noted that this value was obtained under extreme assumptions about the white dwarf mass-loss rate and the wind velocity and assuming a 100% efficiency of the ablation mechanism.

A modification of the scenario of rapid mass loss in a symbiotic binary with a white-dwarf mass approaching M_{Ch} could be the formation of a common envelope. This might happen due to the expansion of the red-supergiant envelope induced by the white-dwarf wind and the subsequent Roche-lobe overflow. The common envelope could also result in the loss of the envelope by the red supergiant on a time scale of several hundred years.

A drawback of the mechanisms of rapid mass loss induced by the white dwarf contraction at the mass $M \approx M_{\mathrm{Ch}}$ is the relatively weak dependence of the kinetic luminosity of the white dwarf wind on the dwarf radius. This leaves the following troublesome question unsolved: Why is the envelope lost at the right time, but not, say, $\sim 10^3$ before the supernova explosion?

The alternative scenario for the evolution of a symbiotic star suggests the formation and loss of a common envelope with the subsequent merger of a sub-Chandrasekhar CO white dwarf and the degenerate CO core of a red supergiant. The formation of a super-Chandrasekhar mass object followed by a SN Ia explosion would then explain the synchronization of the violent loss of the hydrogen envelope and the SN Ia event. However, this, at first glance, natural synchronization mechanism runs into the following serious difficulty:

For the merger of a dwarf and a core due to gravitational-wave radiation to occur shortly after the termination of the common-envelope stage, they must come close together. For the merger to occur in t_0 years, the initial semimajor axis of the dwarf–core system must be (Landau and Lifshitz 1973)

$$a = 2 \times 10^9 \left(\frac{t_0}{100\ \mathrm{yr}}\right)^{0.25} \left(\frac{M}{M_\odot}\right)^{0.5} \left(\frac{\mu}{M_\odot}\right)^{0.25}\ \mathrm{cm}, \tag{3}$$

where M is the total mass of the system, and μ is its reduced mass. For example, for equal masses of components ($0.8M_\odot$) and $t_0 = 100$ yr, the separation between the components after the common-envelope stage must be $a = 2 \times 10^9$ cm. Such a close approach is accompanied by the release of 8.6×10^{49} erg of the binding energy with 4.3×10^{49} erg deposited onto the envelope in the form of hydrodynamic motions. This estimate depends weakly on the masses of the dwarf and the core. If all this energy is spent on the ejection of the envelope, then, given the low binding energy of the red-giant envelope ($<10^{48}$ erg), the kinetic energy of the circumstellar envelope must be $\sim 4 \times 10^{49}$ erg. In reality, for a mass of the CS envelope of $5M_\odot$ and its expansion velocity <300 km s^{-1} (Hamuy *et al.* 2003), the kinetic energy of the envelope is only $<5 \times 10^{48}$ erg, i.e., at least an order of magnitude lower. Thus, the energy released during the spiral-in cannot be spent entirely on the ejection of the envelope. On the other hand, such a huge energy cannot be radiated away in several hundred years either. Actually, the maximum average luminosity of a gravitationally bound red supergiant with an initial mass of $<10M_\odot$ does not exceed $10^5 L_\odot$ (Iben and Renzini 1983). Even in the case of a maximum luminosity, the total energy radiated away in 600 yr does not exceed 8×10^{48} erg. The rate of energy generation during the spiral-in that exceeds the rate of radiation by a hydrostatic configuration would result in a rapid expansion of the envelope and in the termination of the spiral-in process.

In other words, at the stage of intense mass loss from the common envelope, the dwarf and the core cannot come closer together than allowed by the energy loss via radiation and mass loss ($\sim 10^{49}$ erg). In this case, the minimum final separation between the objects after the common-envelope phase must be $\sim 10^{10}$ cm with an unacceptably long merger time, $\sim 6 \times 10^4$ yr. Thus, the model of a merger in a common envelope cannot explain the synchronization of violent mass loss and the supernova explosion within several hundred years. Therefore, the merger scenario for SN 2002ic and SN 1997cy is unlikely.

The model of a white-dwarf explosion in a system with a red supergiant component predicts an interesting effect. If the hydrogen-rich envelope of the giant is not lost completely prior to the explosion, several tenths of a solar mass will then be lost due to the interaction of the supernova envelope and the red supergiant. The bulk of this matter acquires a low velocity ($\sim 10^3$ km s^{-1}) and, thus, must reside in the inner part of the expanding supernova envelope (Chugai 1986; Livne *et al.* 1992). Detection of a narrow Hα line from the "inner" hydrogen in the SN Ia spectrum would indicate an explosion in a system with a red supergiant. Of course, the presence of a narrow Hα line from circumstellar gas makes it much more difficult to detect Hα from the central region of SN Ia.

4.2. A Single Star

Following the pioneering paper by Becker and Iben (1979), it is commonly assumed that Chandrasekhar-mass CO cores cannot be formed in single stars. For example, according to Gil-Pons *et al.* (2003), stars with an initial mass of $(8.7-11)M_\odot$ ignite carbon in their weakly degenerate cores, and the burning extends to the formation of Ne and Mg. The envelopes of the stars are lost by stellar (super)wind. However, uncertainties in the models of intermediate-mass stars do not completely rule out the possibility that exploding Chandrasekhar-mass CO cores are formed in these stars (Iben and Renzini 1983). Such hypothetical supernovae were called SN 1.5 to emphasize their intermediate status between SN Ia and SN II.

One of the uncertainties in the evolutionary computations of the limiting mass of CO cores is related to the usually disregarded rotation. Dominguez *et al.* (1996) roughly took into account the rotation in a one-dimensional model and showed that the lifting effect allows a star with an initial mass of $6.5M_\odot$ to form a Chandrasekhar-mass CO core.

Another obstacle to the SN 1.5-type supernova scenario is probably a complete loss of the envelope via superwind before the mass of the core reaches $M_{\rm Ch}$. Remarkably, SN 1997cy exploded in a dwarf galaxy (Turatto *et al.* 2000), presumably like SN 2000ic (Hamuy *et al.* 2003). A common property of the dwarf galaxies is the low metallicity that favors a low mass-loss rate. This could explain why the envelopes of presupernovae have not been lost by the AGB superwind prematurely.

Let the combination of a low metallicity and rotation eventually lead to the formation of a Chandrasekhar-mass CO core in a single star. What can then cause an intense mass loss by a supergiant ~ 600 yr before the explosion? We may assume that the contraction of the core as it approaches the Chandrasekhar mass can lead to intense mass loss. For instance, an increase in gravitational potential and, hence, a rise in temperature and density may result in more intense energy release in the double burning shell source at the core boundary. Another possibility may be related to C-burning flashes in the CO core.

The absence of a smooth continuum in the early spectra of SN 2002ic implies that the mass of the hydrogen in the supernova envelope is much smaller than 1 $M_\odot$. Thus, the scenario of a single-star explosion suggests that the hydrogen envelope must be almost completely lost prior to the explosion.

5. CONCLUSIONS

Our simulations of the light curves for SN 2002ic and SN 1997cy in the model of SN Ia expansion in a dense circumstellar envelope led us to conclude that (i) the densities of the CS envelope for both supernovae are virtually equal and the corresponding mass loss prior to the SN explosion occurred on a time scale of several hundred years with a rate of $\sim 10^{-2}$ $M_\odot$ yr^{-1}; the formation time scale of the CS envelope of SN 1997cy did not exceed 600 yr.

If SN 2002ic and SN 1997cy are actually type-Ia supernovae that exploded in dense circumstellar envelopes, there must be a mechanism that synchronized the intense outflow of a huge amount of matter in several hundred years and the SN Ia explosion event. Our analysis of the two possible scenarios that could lead the explosions of SN 2002ic and SN 1997cy—accretion onto a white dwarf in a symbiotic system and SN 1.5 scenario—does not allow us to reliably identify the mechanism of the synchronization of intense mass loss and CO—dwarf explosion. We believe that the most natural mechanism must involve the contraction of the CO white dwarf (in the binary star scenario) or the CO core (in the SN 1.5 scenario) as the Chandrasekhar limit is approached. However, the details of the process that must turn on violent mass loss by the supergiant several hundred years before the SN Ia explosion are yet to be understood. It should be emphasized that we rule out, at first glance, the natural scenario of the merger of a CO white dwarf and the CO core of a red supergiant due to the angular momentum loss via gravitational-wave radiation after the ejection of the common envelope.

Both scenarios have interesting predictions that may turn out to be crucial for their verification. The scenario of a symbiotic star predicts a wide range of masses for the CS envelopes—from several tenths of $M_\odot$ to about $6\,M_\odot$; the low masses are dominant, since low-mass giants prevail in symbiotic systems. In the single-star scenario, the initial mass is close to $8\,M_\odot$; therefore, the CS envelopes must be similar and massive. If future observations reveal a relatively large number of SN 2002ic-type events with a mass of the CS envelope larger than one solar mass, then the single-star model must be preferred. At present, with only two detected SN 2002ic-like events, both indicating high-mass CS envelopes, the SN 1.5 scenario is favored.

Note that SN 2002ic-subtype events are extremely rare. The fact that, although their luminosities exceed the luminosity of a typical SN Ia, only two such supernovae have been discovered to date, implies that their relative rate of occurrence among all SNe Ia is less than 1%.

When taking into account the deviations of the chemical composition of the envelope around SN Ia from the solar one, the mass of the circumstellar envelope of SN 1997cy is close to $2M_\odot$, inslead of $5M_\odot$, while the density distribution in the CS envelope is close to $\rho \propto r^{-2}$. However, this does not change our conclusions[1].

ACKNOWLEDGMENTS

This work was supported in part by the Russian Foundation for Basic Research (project nos. 01-02-16295 and 03-02-16254) and the Federal Science and Technology Program for Astronomy.

REFERENCES

1. W. D. Arnett, Astrophys. Space Sci. **5**, 180 (1969).
2. W. D. Arnett, Astrophys. J. **237**, 541 (1980).
3. S. A. Becker and I. Iben, Jr., Astrophys. J. **232**, 831 (1979).
4. R. A. Chevalier, Astrophys. J. **259**, 302 (1982).
5. N. N. Chugai, Astron. Zh. **63**, 951 (1986) [Sov. Astron. **30**, 563 (1986)].
6. N. N. Chugai, Astron. Zh. **69**, 125 (1992) [Sov. Astron. **36**, 63 (1992)].
7. N. N. Chugai, Mon. Not. R. Astron. Soc. **326**, 1448 (2001).
8. N. N. Chugai and I. D. Dantsiger, Pis'ma Astron. Zh. **29**, 732 (2003) [Astron. Lett. **29**, 649 (2003)].
9. I. Dominguez, O. Straniero, and A. Tornambe, Astrophys. J. **472**, 783 (1996).
10. P. Gil-Pons, E. Garcia-Berro, J. Jose, M. Hernanz, and J. W. Truran, astro-ph/0306197 (2003).
11. I. Hachisu, M. Kato, and K. Nomoto, Astrophys. J. **522**, 487 (1999).
12. M. Hamuy, M. M. Phillips, N. B. Suntzeff, *et al.*, Nature **424**, 651 (2003).
13. P. Höflich, A. M. Khokhlov, and J. C. Wheeler, Astrophys. J. **444**, 831 (1995).
14. I. Iben, Jr. and A. Renzini, Ann. Rev. Astron. Astrophys. **21**, 271 (1983).
15. L. D. Landau and E. M. Lifshitz, *Field Theory* (Nauka, Moscow, 1973) [in Russian].
16. E. Livne, Y. Tuchman, and J. C. Wheeler, Astrophys. J. **399**, 665 (1992).
17. M. Turatto, T. Suzuki, P. Mazzali, *et al.*, Astrophys. J. Lett. **534**, L57 (2000).
18. J. Whelan and I. Iben, Jr., Astrophys. J. **186**, 1007 (1973).
19. P. R. Wood, *Circumstellar Media in the Late Stages of Stellar Evolution,* Ed. by R. E. S. Clegg, I. R. Stevens, and W. P. S. Meikle (Cambridge Univ. Press, Cambridge, 1994), p. 15.

Translated by N. Chugai

---

[1] After the paper was accepted for publication, a preprint by M. Livio and A. Riess appeared, astro-ph/0308018, in which they independently suggested the scenario for the merging of a CO white dwarf and a CO red giant core considered here.

Astronomy Letters, Vol. 30, No. 2, 2004, pp. 73–85. Translated from Pis'ma v Astronomicheskiĭ Zhurnal, Vol. 30, No. 2, 2004, pp. 92–104.
Original Russian Text Copyright © 2004 by Fedorova, Tutukov, Yungelson.

Type-Ia Supernovae in Semidetached Binaries

A. V. Fedorova, A. V. Tutukov, and L. R. Yungelson[*]

Institute of Astronomy, Russian Academy of Sciences, ul. Pyatnitskaya 48, Moscow, 119017 Russia

Received June 19, 2003

Abstract—We consider the evolutionary scenarios for close binaries that lead to the formation of semidetached systems in which a white dwarf can accumulate the Chandrasekhar mass through mass accretion from its companion, a main sequence star or a subgiant of mass $M \sim 2M_\odot$. Such dwarfs probably explode as type-Ia supernovae or collapse to form a neutron star. The population synthesis method is used to analyze the dependence of the model rate of these events in the Galaxy on the common envelope parameter, the mass transfer rate, and the response of a main-sequence star to helium accretion at an intermediate evolutionary stage. The rate of explosions in semidetached systems of this type in the Galaxy was found to be no higher than $\simeq 0.2 \times 10^{-3}$ yr^{-1}, which is less than 10% of the lower level for the empirically estimated SNe Ia rate. *© 2004 MAIK "Nauka/Interperiodica".*

Key words: *stars—structure and evolution, binaries, accretion, supernovae.*

INTRODUCTION

The problem of the progenitors of type Ia supernovae is not yet resolved. The relatively high fraction of the so-called "peculiar" SNe Ia (which may be as high as $\simeq$40% (Li *et al.* 2001)) may indicate that progenitors of SNe Ia do not form a homogeneous group. Researchers usually consider three possibilities: (a) explosion of a white dwarf that has grown to Chandrasekhar mass $M_{\rm Ch}$ by accreting mass from its companion in a semidetached (Whelan and Iben 1973; Iben and Tutukov 1984) or detached (Tutukov and Yungelson 1976; Munari and Renzini 1992) binary; (b) explosion during the coalescence of two white dwarfs whose total mass is greater than or equal to the Chandrasekhar limit (Tutukov and Yungelson 1981; Webbink 1984; Iben and Tutukov 1984); and (c) explosion of a (sub)Chandrasekhar-mass dwarf triggered by the detonation of accreted helium in a semidetached binary with a helium donor (Livne 1990).

In this paper we use population synthesis to estimate the possible occurrence rate of SNe Ia explosions and accretion-induced collapse events resulting from the growth of white dwarfs to the Chandrasekhar limit in close binary systems with hydrogen/helium companions to white dwarfs. We analyze in detail how the potential SNe Ia occurrence rate depends on the parameters of the computations and find that this channel may account for $\lesssim$10% of all SN+ Ia progenitors.

SCENARIOS OF EVOLUTION TOWARD SN IA

Figures 1 and 2 show schematically (not to scale) the scenarios of the evolution of stars toward SN Ia via the channel of semidetached binaries (hereafter called scenarios I and II, respectively). In both scenarios, the initial mass of the primary, M_{10}, is approximately equal to $5-11M_\odot$, and the mass of the companion, $M_{20} \approx 0.8-3.5M_\odot$. In scenario I the semimajor axis of the orbit corresponds to the primary filling its Roche lobe at the stage of hydrogen burning in the shell (the Case B of mass transfer). The loss of mass by the donor results in the formation of a common envelope inside which the components approach each other. The remnant of the primary component in this case is a helium star of mass $\simeq 0.8-2.5M_\odot$. Helium remnants of stars in this mass interval expand after the formation of the CO core (Iben and Tutukov 1985; Bitzaraki *et al.* 2002); this results in the second Roche lobe overflow by them and the accretion of helium-enriched matter by the companion. The mass loss rate of the star with a CO-core and expanding helium shell is determined by the thermal time scale of the star ($\sim 10^5$ yr). The results of evolutionary computations (Iben and Tutukov 1985) make it possible to estimate the amount of mass lost by the remnants of primary components with initial masses $5-11M_\odot$ during the second mass-transfer phase:

$$\frac{\Delta M}{M_\odot} \approx 0.2 \left(\frac{M_{10}}{7M_\odot}\right)^4, \qquad (1)$$

---

[*] E-mail: `lry@inasan.rssi.ru`

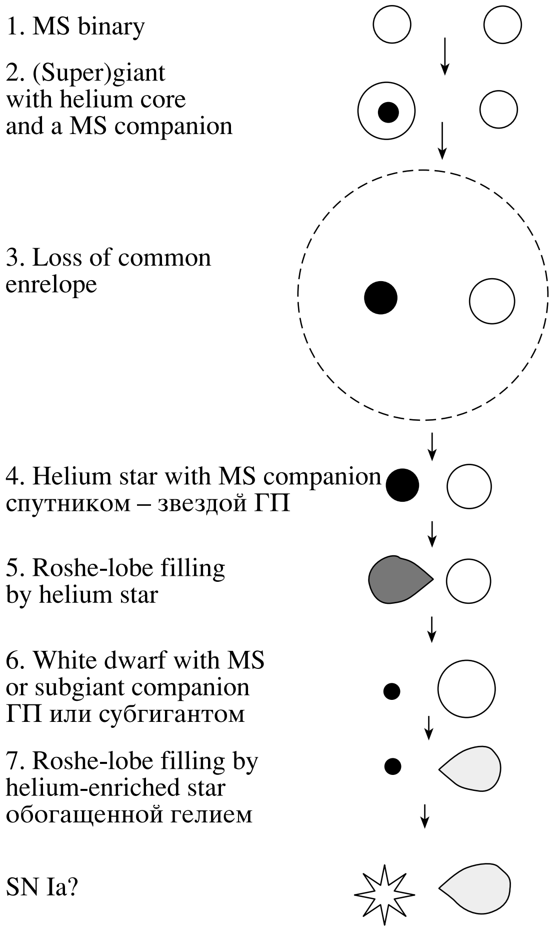

Fig. 1. Evolutionary scenario that results in the formation of a potential type-Ia presupernova in the case B of mass transfer (the "channel of helium-rich supersoft X-ray sources," scenario I).

and the mass-loss rate:

$$\dot{M}_{\rm He} \approx 6.3 \times 10^{-13} \left(\frac{M_{10}}{M_\odot}\right)^{7.5} M_\odot\ {\rm yr}^{-1}. \quad (2)$$

As a result of mass loss, the helium star transforms into a CO dwarf. Accretion most likely results in the total mixing of matter in the companion (see below), which becomes somewhat overabundant in helium: $Y \sim 0.4$ (Hachisu *et al.* (1999) called this scenario the "Helium-rich Supersoft X-ray Source Channel"). The companion, in turn, fills its Roche lobe at the main sequence or soon after leaving it. In the case of stable mass transfer the accreting dwarf may grow to the Chandrasekhar mass.

Scenario II differs from scenario I by greater initial separation between the components. Correspondingly, the primary fills the Roche lobe at the stage of asymptotic giant branch, and evolves into a white dwarf bypassing the helium-star stage. In both scenarios, the binary at the stage of accretion onto the white dwarf can manifest itself as a supersoft X-ray source (Kylafis and Lamb 1982; van den Heuvel 1992).

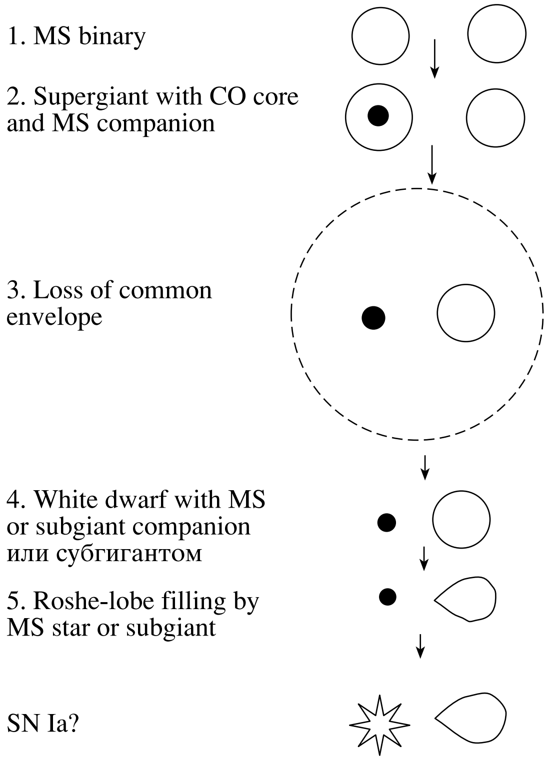

Fig. 2. Evolutionary scenario that results in the formation of a potential type Ia presupernova in case C of mass transfer (scenario II).

One of the evolutionary stages in scenario I is the stage of the accretion by the main-sequence star of helium from the remnant of the primary component (Fig. 1, stage 5). In our previous papers we assumed that due to the high accretion rate determined by Eq. (2) this process is accompanied by the formation of a common envelope whose matter is totally lost by the system. On the other hand, Hachisu et al. (1999), e.g., assumed that the system does not develop a common envelope and that mass transfer remains strictly conservative. In reality, the possibility of the formation of a common envelope depends on the change of star's radius during accretion, which thus becomes an additional parameter whose effect on the results of scenario modeling of the potential SNe Ia occurrence rate is to be analyzed. Let us consider this issue in more detail.

HELIUM ACCRETION BY A MAIN-SEQUENCE STAR WITH AN INITIAL MASS OF $2M_\odot$

Stothers and Simon (1969) long ago pointed out that one of the components of the binary—a main

Table 1. Parameters of evolutionary tracks with accretion of helium

Number of track	$\dot{M}_\mathrm{a}$, $M_\odot$/yr	Mixing	R_max/R_0	R_min/R_0
1	2×10^{-5}	Diffusion	1.00	0.73
2	10^{-5}	Diffusion	1.00	0.64
3	10^{-6}	Diffusion	1.00	0.56
4	2×10^{-5}	Instantaneous	2.84	1.00
5	10^{-5}	Instantaneous	1.91	1.00
6	10^{-6}	Instantaneous	1.17	1.00

Notes: $\dot{M}_\mathrm{a}$—accretion rate, R_max/R_0 and R_min/R_0 are the ratios of the maximum and minimum radius of the star to its initial radius, R_0, respectively.

sequence star—may accrete helium whose molecular weight exceeds the molecular weight of the matter at the surface of the accretor. So far, however, no evolutionary computations with allowance for helium accretion have been performed for low- and intermediate-mass stars.

We analyzed the evolution of a main sequence star with an initial mass of $2M_\odot$, which accretes $\Delta M = 0.5M_\odot$ of helium-rich matter at a constant rate of $\dot{M}_\mathrm{a}$. This combination of masses corresponds to a rather typical binary progenitor of a potential SNe Ia with the initial component masses equal to 9 and $2M_\odot$ [see Eq. (1) and Fig. 5 below].

We performed our computations for several $\dot{M}_a$ (Table 1) that can be realized in the scenarios of the evolution of close binaries leading to SNe Ia (see Eq. (2) and Fig. 5). For our computations, we used a program oriented toward analyzing the evolution of low-mass stars (Tutukov and Fedorova 2001). We adopted the following initial chemical composition for the accreting star: $X = 0.70$, $Y = 0.28$, and $Z = 0.02$. The adopted chemical composition of the accreted matter is: $Y = 0.98$ and $Z = 0.02$.

We considered two variants of the possible evolution of the accreting star:

The inverse gradient of molecular weight must result in the instability and mixing of matter at the boundary of the helium layer (see, e.g., Ulrich 1972). Kippenhahn *et al.* (1980) showed that mixing in a spherically-symmetric nonrotating star can be treated as the formation of helium "bubbles" and their diffusion inside the hydrogen base. As the bubbles sink, they disintegrate and mix with the surrounding medium. In this model the diffusion coefficient D is equal to:

$$D = \frac{H_p}{\nabla_\mathrm{ad} - \nabla}\frac{4acT^3}{C_p\kappa\rho^2}\left|\frac{d\mu}{dr}\right|\frac{1}{\bar{\mu}}. \qquad (3)$$

Here we use the conventional designations for physical quantities; κ is the opacity and $\bar{\mu}$ the mean molecular weight in the region of the gradient of chemical composition. The time scale τ, during which the width W of the transition layer with chemical composition gradient increases by a factor of two, is determined as (Kippenhahn *et al.* 1980)

$$\tau \approx W^2/D. \qquad (4)$$

In the first variant of computations we used formulas (3) and (4) to determine the variations of the helium distribution in the star during accretion.

In the second variant we assumed the faster mixing of the accreted matter that was found by Kippenhahn *et al.* (1980). This assumption is based on the time-scale estimates for the processes that accompany the sinking of turbulent elements, which, at least in one-dimensional approximation, prove to be much shorter than the accretion time scale of $\sim(10^5\text{–}10^6)$ yr (see Appendix). We therefore performed a series of computations for the limiting case with the "instantaneous" total mixing of the accreted matter.

Table 1 lists the parameters of the evolutionary tracks. Figure 3 shows the tracks of accreting stars in the Hertzsprung–Russell diagram and the variation of stellar radius as a function of mass. Figure 4a shows the time variation of the helium density profile for Track *2*; it partially includes the stage of the post-accretion evolution. Computations showed that under the assumption of diffusion (Tracks *1–3*), the stellar radius decreases because of the decreasing opacity of the matter of the envelope in the course of helium accretion.

The expansion of the star, which is typical for high accretion rates, takes place if we assume the total "instantaneous" mixing of the accreted helium (Tracks *4–6*). If the accretion rate is $2\times 10^{-5}M_\odot\,\mathrm{yr}^{-1}$, the maximum stellar radius is three

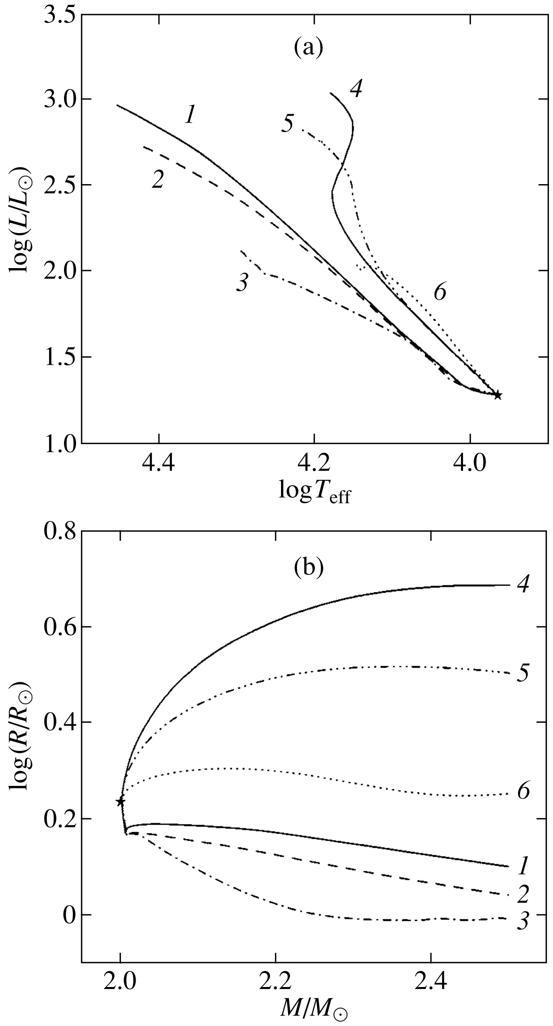

Fig. 3. Variation of the parameters of accreting stars as a function of accretion rate and mixing method: (a) star tracks in the Hertzsprung–Russell diagram; (b) dependence of the radii of accreting stars on mass. Numbers correspond to track numbers in Table 1. Asterisk indicates the position of the initial model.

times greater than the initial radius, and this ratio is smaller for lower accretion rates (Table 1). The increase in the stellar radii is due to the release of internal energy as a result of the increase in the mean molecular weight of stellar matter.

After the end of the accretion stage, all models relax toward almost the same radius over a close-to-thermal time scale independently of the mixing mode (Fig. 4b).

Thus, so far, the computations do not make it possible to unambiguously determine the pattern of the variation of the radii of stars with initial masses of $1-3M_{\odot}$ accreting helium with evolution-determined rates. It is nevertheless clear that the hypothesis that this process is accompanied by the formation of common envelopes is by no means the only possible one.

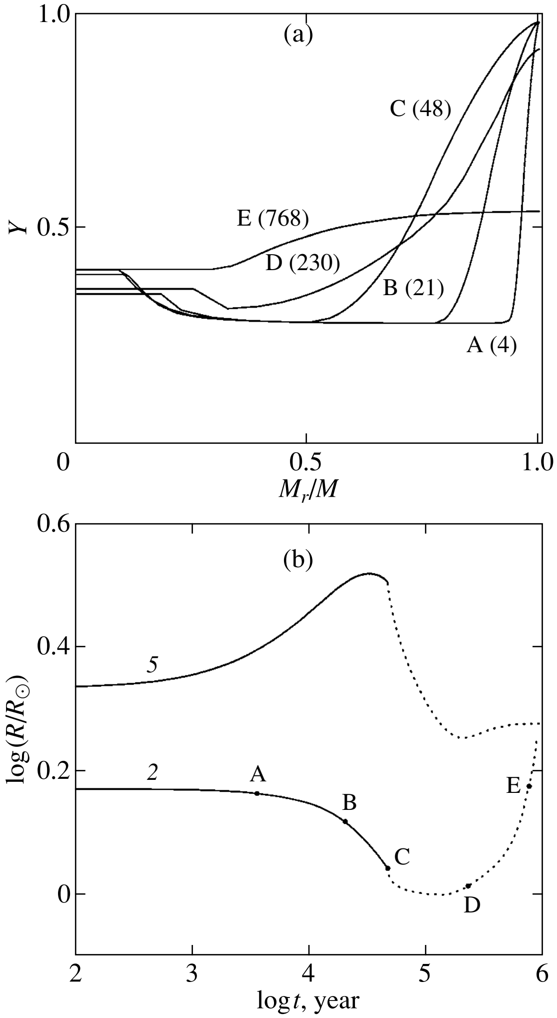

Fig. 4. (a) Time variation of the helium density profile for Track 2 (including the post-accretion stage). Numbers indicate the time elapsed since the onset of accretion, in in the units of 10^3 yr. (b) Time variation of the stellar radius for Tracks *2* and *5* at the accretion (solid line) and post-accretion (dashed line) stages. Letters indicate the positions of the models whose helium distribution profiles are shown in Fig. 4a.

POPULATION SYNTHESIS FOR PROGENITORS OF SN IA IN SEMIDETACHED SYSTEMS

In our previous works, we analyzed the accumulation of the Chandrasekhar mass by dwarfs in cataclysmic variables evolving on the thermal time scale of the donor or on the time scale of the loss of angular momentum by the donor that is due to magnetic stellar wind (Yungelson *et al.* 1996) and in systems with subgiant donors with degenerate helium cores, which evolve on the thermal or nuclear time scale of the donor (Yungelson *et al.* 1996; Yungelson and Livio 1998, 2000). Donor masses were limited by $1.5M_{\odot}$ and $2.5M_{\odot}$ in the first and second cases, respectively. Our estimates of the occurrence rate of potential SNe Ia in semidetached systems did not exceed $\sim$10% of the empirical estimate of the total SNe Ia occurrence rate in the Galaxy, which is equal to $(4 \pm 2) \times 10^{-3}$ yr^{-1} (Cappellaro and Turrato 2001). On the other hand, Hachisu *et al.* (1996, 1999) and Li and van den Heuvel (1997) found that this frequency may be comparable to the empirical estimate of the SNe Ia occurrence rate in the Galaxy. Note, however, that the computations reported in the latter works used as a "starting point" systems consisting of a white dwarf and a main-sequence or subgiant companion. The authors of these papers did not determine the formation frequency of such systems via detailed population synthesis, and this may partly explain the discrepancy mentioned above (Yungelson and Livio 1998).

In this paper we analyzed the possibilities for the white dwarfs to reach Chandrasekhar masses, in systems evolving according to scenarios I and II, under uniform assumptions about mass loss by the donors and accumulation of mass by the accretors.

It is evident that potential SNe Ia accumulate most of their mass during the accretion on thermal time scale when hydrogen burns steadily and the rate of its accumulation is equal to $\dot{M}_{\rm st} \simeq 10^{-7}$–$10^{-6} M_\odot$ yr^{-1}. In addition to the binaries considered above, we also computed the evolution of stars with main-sequence donors, limiting their mass only by the condition of dynamically stable mass transfer: $q = M_2/M_1 \lesssim 2.5$ (Tutukov *et al.* 1982; Hjellming and Webbink 1987). At $1.2 \lesssim q \lesssim 2.5$, mass transfer in these systems proceeds on a time scale close to the thermal time scale of the donor until the time when the component masses become equal to each other. The accretion rate $\dot{M}_{\rm a}$ in this case may exceed the maximum rate of stationary hydrogen burning $\dot{M}_{\rm st}$. Following Kato and coauthors (Kato and Iben 1992; Kato and Hachisu 1994; Hachisu *et al.* 1996), we assumed that stationary hydrogen burning may produce optically thick wind, which allows excess mass to leave the system. Specific angular momentum of the wind is equal to that of the dwarf. Mass loss in this mode stabilizes mass transfer in the system. Optically thick wind is possible only at accretion rates $\dot{M}_{\rm a} \lesssim 10^{-4} M_\odot$ yr^{-1}. Higher $\dot{M}_{\rm a}$ must result in the formation of common envelopes.

To compute the possible occurrence rate of SNe Ia in semidetached systems, we refined the treatment of the efficiency of mass accumulation by the dwarf, the mass loss of the system, and the possible variants of the behavior of the radius of the accreting star in the population synthesis program we used in our earlier papers (Yungelson *et al.* 1996; Yungelson and Livio 1998, 2000). Here we point out only that we assume that all stars in the Galaxy form in binary systems, and adopt the star-formation function for binaries in the form (Iben and Tutukov 1984)

$$\frac{dN}{dt} = 0.2d(\log a)\frac{dM_{10}}{M_{10}^{2.5}}f(q_0)dq_0, \qquad (5)$$

where a is the separation between the components; $f(q_0)$, the distribution of component mass ratios, $q_0 = M_{20}/M_{10}$, normalized to unity. Function (5) is normalized to the formation of one binary with $M_{10} \geq 0.8M_\odot$ per year. The mass of white dwarf progenitors is equal to $(0.8$–$11.4)M_\odot$ (Iben and Tutukov 1985). We assumed that star formation rate was constant over 13×10^9 yr.[1] We further assume that component mass ratios of close binaries have a flat distribution and approximate the space of the initial parameters of binaries by a rectangular grid with a step of 0.0125, 0.0125, and 0.025 in $\log M_{10}$, $\log a$, and component mass ratio, respectively.

The number of binaries where mass transfer may result in the accumulation of $M_{\rm Ch}$ is determined mostly by the common envelope parameter, $\alpha_{\rm ce}$. We adopted the "common envelope equation" in the form

$$\frac{(M_{\rm a0} + M_{d0})\Delta M}{a_0} = \alpha_{\rm ce}\left[\frac{M_{\rm df}M_{\rm af}}{a_{\rm f}} - \frac{M_{a0}M_{d0}}{a_0}\right], \qquad (6)$$

where subscripts 0 and f indicate the initial and final values, respectively, of the accretor and donor masses and separations between the components, and ΔM is the mass of the ejected envelope. Here $\alpha_{\rm ce}$ is a measure of the comparison of the orbital energy of the binary and the binding energy of the common envelope. So far, $\alpha_{\rm ce}$ cannot be confidently constrained by either theory or observations. We choose $\alpha_{\rm ce}$ values based on the results of an analysis of observational data that are indicative of the high efficiency of the deposition of the orbital energy into common envelopes, and of the loss of a substantial fraction of donor envelopes before the common-envelope stage, which is equivalent to high $\alpha_{\rm ce}$ (Iben 2000; Nelemans *et al.* 2000; Soker 2002). For this reason, we varied $\alpha_{\rm ce}$ from 0.5 to 5. The use of $\alpha_{\rm ce} > 1$ is justified, because Eq. (6) is only a formal order-of-magnitude comparison of energies. Note, of course, that the use of the same $\alpha_{\rm ce}$ for all common envelopes irrespective of the evolutionary stage of the donor and accretor is a forced simplification (see Dewi and Tauris (2000) and Tauris and Dewi (2001), who estimated the binding energies of the envelopes for stars of various masses as a function of the evolutionary stage).

For each system that forms in the course of evolution with a main sequence donor, we assumed that the

---

[1] This assumption is justified, since we analyze only short-lived ($\lesssim 10^9$ yr) stars with $M \gtrsim 1.6M_\odot$ (see Fig. 5).

mass-loss rate of the latter is constant and equal to $\dot{M}_{\rm d} = \alpha_{\rm th}\dot{M}_{\rm KH}$, where $\dot{M}_{\rm KH}$ is the rate corresponding to the thermal time scale of the donor. It is evident that in real systems, $\dot{M}_{\rm d}$ depends on the component mass ratio (it decreases with decreasing q) and the evolutionary state of the donor at the time of the Roche-lobe filling, and changes in the course of evolution. The quantity $\alpha_{\rm th}$ is another parameter of the problem, which we varied from 0.2 to 1. We limited the duration of the mass-loss stage by either the time when the mass of the dwarf reached $M_{\rm Ch}$, or the time of the equalization of component masses. In systems with subgiant donors, the mass-loss rate first corresponded to thermal time scale, and then to the time scale determined by the growth rate of the helium core (see Yungelson and Livio 1998). In these systems, the mass-transfer stage was limited by either the time when the dwarf mass reached $M_{\rm Ch}$ or by the time of the total loss of the hydrogen shell by the donor.

We allowed for the efficiency of the accumulation of hydrogen by dwarfs (or their erosion as a result of nova explosions at accretion rates $\dot{M}_{\rm a} \lesssim 1.5 \times 10^{-8} M_\odot\ {\rm yr}^{-1}$) in accordance to the grids of Prialnik and Kovetz (1995). We estimated the loss of helium as a result of thermal outbursts in the layer accumulated as a result of hydrogen burning (for $\dot{M}_{\rm a} \simeq 10^{-8}$–$10^{-6} M_\odot\ {\rm yr}^{-1}$) in accordance with Kato and Hachisu.

In accordance with the results of our accretion computations, we analyzed two limiting cases of the response of the future main-sequence donor in the system with a white dwarf to the accretion of helium-enriched matter: conservative mass transfer where the radius of the accretor varies only in accordance with the mass-radius relation, and conservative mass transfer accompanied by a triple increase of the accretor's radius. For comparison, we also computed the SNe Ia occurrence rate assuming that accretion is accompanied by the formation of a common envelope, similarly to our previous computations.

Table 2 summarizes the results of our computations. For each combination of $\alpha_{\rm ce}$ and $\alpha_{\rm th}$, the table gives the occurrence rates for the supernovae that accumulate $M_{\rm Ch}$ via scenario I under various assumptions about the response of the main-sequence star to accretion of He (the upper three rows), and via scenario II (the fourth row). As AIC we give separately results for white dwarfs with initial masses $\gtrsim 1.19 M_\odot$, which, as we assume, consist of a mixture of oxygen, neon, and magnesium, and in the case of accretion rates exceeding $\simeq 10^{-8} M_\odot\ {\rm yr}^{-1}$, apparently do not explode as SNe Ia having accumulated $M_{\rm Ch}$, but collapse producing neutron stars (Nomoto and Kondo 1991). Figure 5 shows the position of progenitors of systems where the dwarf can accumulate the mass of $M_{\rm Ch}$ on the "initial mass of the primary—separation between the components" diagram for one of the most "productive" variants (number 13 in Table 2). The same figure shows the relation between the masses of donors—main sequence or subgiant stars—and accretors—white dwarfs whose mass reaches $M_{\rm Ch}$ during the subsequent evolution, at the time when the donor fills its Roche lobe. The two groups of objects in Fig. 5b are systems where the donor fills its Roche lobe during the main-sequence stage ($M_{\rm d} \geq 2.5 M_\odot$) and systems with subgiant donors ($M_{\rm d} = 1.5$–$2.2 M_\odot$). The "gap" between the two groups is due to the fact that stars with masses $\gtrsim 2.2 M_\odot$ develop deep convective envelopes immediately after leaving the main sequence, and this process results in mass transfer on the dynamic time scale and formation of common envelopes.

Interestingly, a majority of the "presupernova" degenerate dwarfs are not very massive initially ($M_{\rm a} \lesssim 1 M_\odot$) and have rather low-mass companions: $M_{\rm d} \lesssim 2 M_\odot$. The fact that these very systems combine rates of stationary hydrogen burning and mass transfer that are favorable for growing to the Chandrasekhar mass, with the results of Langer *et al.* (2000) and Sarna *et al.* (2002), who performed detailed computations of the evolution of binary systems consisting of main sequence and dwarf stars.

The dependence of the results on the parameters of population synthesis can be summarized as follows:

(1) The number of systems where the white dwarf may grow to the Chandrasekhar mass, is determined mostly by $\alpha_{\rm ce}$. At $\alpha_{\rm ce} > 1$, the number of systems that evolve in accordance with scenario II decreases and such systems virtually disappear at $\alpha_{\rm ce} = 2$, because the effective energy deposition into common envelopes limits the separation of components from below. Scenario I dominates in most of the cases (see Fig. 5, which shows the "dividing line" between the systems evolving in accordance with scenarios I and II, and which depends only slightly on M_{20}).

(2) The decrease of $\alpha_{\rm th}$ from 1 to 0.5 results in an increase of the number of potential supernovae. At high $\alpha_{\rm th}$, a major part of the mass is accreted at a rate exceeding substantially the rate of stationary hydrogen burning, and is lost by the system via stellar wind. At low $\alpha_{\rm th} = 0.2$, the efficiency of the accumulation of helium is also low because of recurrent Novae explosions, which decrease the number of systems where the dwarf can grow to the Chandrasekhar mass.

(3) The assumption that during the accretion of helium-enriched matter the system has a common envelope increases the number of potential SNe Ia in scenario I at $\alpha_{\rm ce} \geq 1$ and $\alpha_{\rm th} \geq 0.5$, because of the increase of the number of systems where the Roche lobe can be filled. At $\alpha_{\rm ce} < 1$, in contrast, component

Table 2. Occurrence rate of potential supernovae and accretion-induced collapses of white dwarfs in semidetached binaries as a function of the parameters of the computations. The observational estimate of the SNe Ia rate in the Galaxy is equal to $(4 \pm 2) \times 10^{-3}$ yr^{-1} (Cappellaro and Turrato 2001).

No.	α_{ce}	α_{th}	SN Ia, 10^{-3} yr^{-1}	AIC, 10^{-3} yr^{-1}	N_{SSS}	No.	α_{ce}	α_{th}	SN Ia, 10^{-3} yr^{-1}	AIC, 10^{-3} yr^{-1}	N_{SSS}
1	1	1.0	0.065	0.088	6080	19	2	0.5	0.210	0.120	4960
2	1	1.0	0.091	0.086	6050	20	2	0.5	0.220	0.150	4980
3	1	1.0	0.050	0.021	6010	21	2	0.5	0.150	0.068	4900
			0.001	0.010					0.0	0.003	
4	2	1.0	0.067	0.002	3850	22	2	0.2	0.120	0.094	5240
5	2	1.0	0.098	0.140	3890	23	2	0.2	0.080	0.095	5210
6	2	1.0	0.073	0.054	3800	24	2	0.2	0.077	0.066	5190
			0.0	0.003					0.0	0.021	
7	5	1.0	0.068	0.011	2650	25	5	0.5	0.210	0.130	3150
8	5	1.0	0.097	0.016	2710	26	5	0.5	0.220	0.170	3270
9	5	1.0	0.085	0.099	2640	27	5	0.5	0.180	0.110	3120
			0.0	0.0					0.0	0.002	
10	0.5	1.0	0.053	0.057	7660	28	5	0.2	0.110	0.130	3250
11	0.5	1.0	0.004	0.004	7580	29	5	0.2	0.110	0.150	3270
12	0.5	1.0	0.0	0.006	7580	30	5	0.2	0.091	0.110	3220
			0.020	0.032					0.0	0.005	
13	1	0.5	0.216	0.110	7100	31	0.5	0.5	0.070	0.050	8630
14	1	0.5	0.140	0.075	7050	32	0.5	0.5	0.005	0.004	8560
15	1	0.5	0.097	0.033	7010	33	0.5	0.5	0.004	0.007	8560
			0.040	0.024					0.120	0.046	
16	1	0.2	0.046	0.063	6750	34	0.5	0.2	0.019	0.033	7870
17	1	0.2	0.021	0.038	6700	35	0.5	0.2	0.0	0.001	7840
18	1	0.2	0.023	0.034	6700	36	0.5	0.2	0.003	0.007	7840
			0.054	0.033					0.066	0.030	

Notes: For each combination of α_{ce} and α_{th}, the table gives the occurrence rate of potential supernovae that accumulate M_{Ch} via scenario I under various assumptions about the response of the main-sequence star to accretion of He: conservative mass transfer (first line); common envelope during accretion of He (second line); triple increase of the radius (third line); and according to scenario II (fourth line).

mergers usually decrease the number of potential SNe Ia.

(4) The effect of the triple increase in the radius of the accreting star, compared to the case of mass transfer without additional expansion, is similar to that of common envelopes, but is somewhat less pronounced. The similarity is due to the narrow the

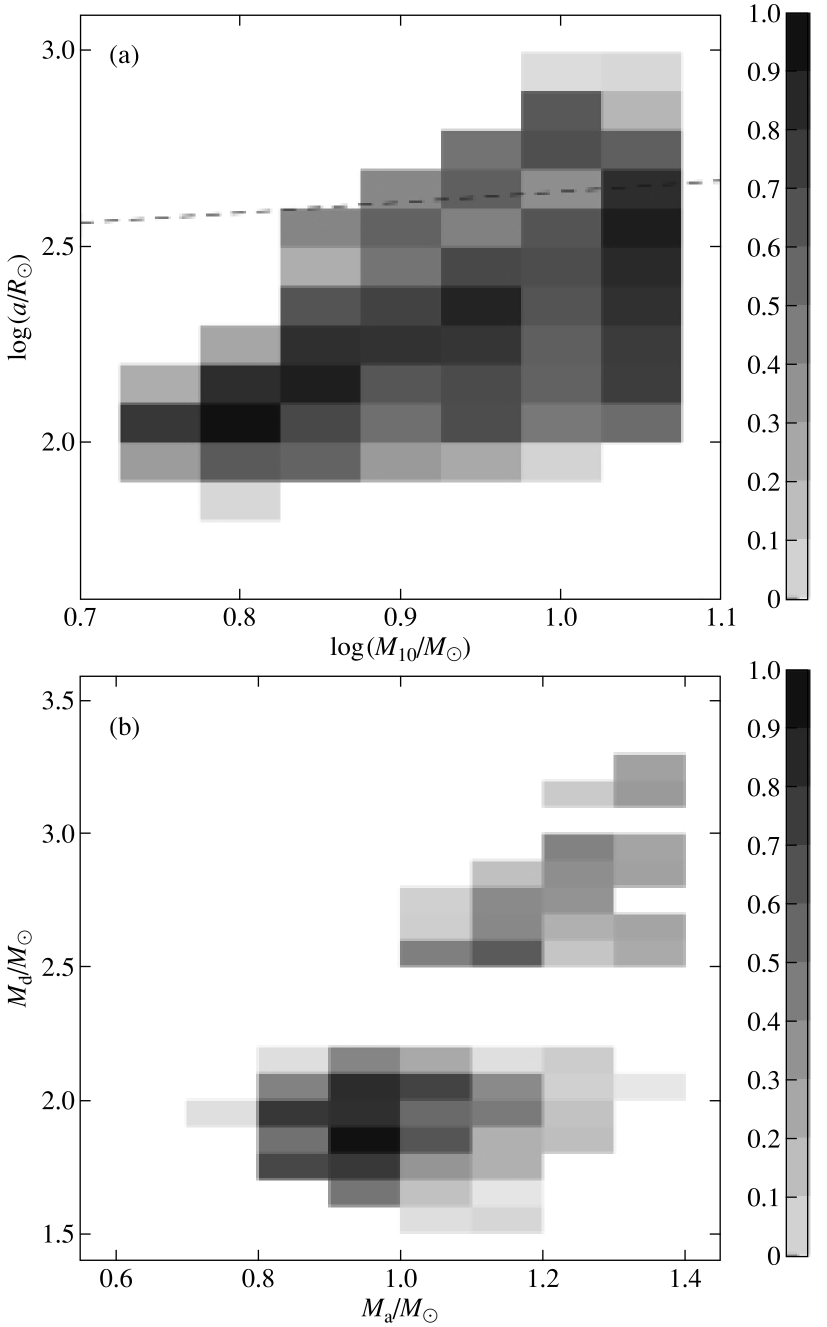

Fig. 5. (a) Progenitors of systems where it is possible for the dwarf to accumulate M_{Ch}, shown on the diagram as "initial mass of the primary—initial separation between the components." The dashed line indicates the distance between the components, which separates the domains where mass loss occurs in cases B and C (at $M_{20} = 2M_{\odot}$). The maximum corresponds to the systems producing an SNe Ia occurrence rate of 0.94×10^{-5} yr^{-1}. (b) Relation between the masses of accretors and donors in systems where the mass of the white dwarf reaches M_{Ch} at the time when the donor fills its Roche lobe (the beginning of stages 7 and 5 in scenarios I and II, respectively). The maximum corresponds to the systems that produce an SNe Ia occurrence rate of 0.15×10^{-4} yr^{-1}. The figure corresponds to model 13 in Table 2.

interval of semimajor axes of SNe Ia progenitors: $\Delta \log a \approx 0.3$–1 (Fig. 5).

(5) A comparison of our results with those of Yungelson and Livio (1998) shows that the inclusion of scenarios where the initial mass of the secondary components exceeds $2.5M_{\odot}$ increases the number of CO dwarfs that accumulate M_{Ch} by no more than ~30%. The increase of the upper limit of the masses of donor stars has a stronger effect on ONe dwarfs: the probability of their collapse increases almost by

a factor of two (cf. Table 1 of Yungelson and Livio (1998)).

Semidetached binaries with accreting white dwarfs with stationary hydrogen burning on their surfaces are usually identified with one of the components of the population of supersoft X-ray sources (van den Heuvel *et al.* 1992; Rappaport *et al.* 1994; Yungelson *et al.* 1996). Table 2 gives for each variant of computations the number of dwarfs that can be observed as supersoft X-ray sources (the total number for scenarios I and II). For stationary objects, we assumed that the lifetime of the supersoft X-ray source is equal to the accretion time corresponding to $\dot{M} \geq \dot{M}_{\rm st}$; for nonstationary objects we assumed that the lifetime is equal to the time after the explosion during which the luminosity of the dwarf exceeds 4×10^{37} erg s^{-1} (see Eq. (12) in the paper by Yungelson *et al.* 1996).

In scenario I, through which most of the systems pass, the matter of donors must be enriched in helium ($Y \sim 0.4$). Note that, so far, no stationary supersoft X-ray sources with manifestations of helium enrichment are known (P. Kahabka, private communication). The only observed helium-enriched source is the recurrent nova U Sco, which is supposed to contain a dwarf with a mass close to $M_{\rm Ch}$ (Hachisu *et al.* 2000; Thoroughgood *et al.* 2001). The estimates of the mass-transfer rate in this system show that in this case, explosions at the surface of the dwarf do not result in its erosion, and it is capable of accumulating $M_{\rm Ch}$ (Sarna *et al.* 2002).

In the Galaxy, two supersoft X-ray sources have been identified, which have orbital periods equal to ~16 h and ~4 days and can belong to the type of systems considered here (Kahabka 2003). The number of sources accessible for observation depends substantially on the poorly known extinction due to interstellar gas and the temperature distribution of sources. For example, Di Stefano and coauthors (Di Stefano and Rappaport 1995, 2003; Di Stefano and Kong 2003) showed that in the Milky Way and other galaxies, the number of observed stationary sources can differ from the total number of such sources by two to three orders of magnitude. When this fact is taken into account, our estimate $N_{\rm SSS}$ (Table 2) does not contradict the observations.

DISCUSSION

The rate with which white dwarfs in semidetached systems accumulate $M_{\rm Ch}$ does not exceed 0.22×10^{-3} yr^{-1} in our models (Table 2, variant 22). Even if we assume that SN Ia explosions really do occur in systems where, according to our definition, accretion-induced collapse takes place, the total occurrence rate does not exceed $\simeq 0.4 \times 10^{-3}$ yr^{-1} (variant 26), this requires a very high $\alpha_{\rm ce} = 5$ and an "optimization" in $\alpha_{\rm th}$. This occurrence rate of explosions makes up only 20% of the lower limit for the empirical estimate of SNe Ia occurrence rate in the Milky Way. This value is actually somewhat overestimated (by 10–20%, since that even if the accretion rate lies within the limits corresponding to stationary hydrogen burning, the accreted mass should be partly lost via the stellar wind of the hot dwarf). The possible contribution of semidetached systems to the total occurrence rate of SNe Ia is nevertheless by no means negligible. Finding hydrogen features in the spectra of SNe Ia would be critical evidence for explosions in these systems. The principal source of hydrogen may be the matter stripped from the companion. Marietta *et al.* (2000) showed that the mass of this matter may amount to $\sim 0.15 M_\odot$ in the systems considered here. Hydrogen can be observed both in very early and in late optical spectra, and in the radio- and X-ray range (Eck *et al.* 1995; Marietta *et al.* 2000; Lentz *et al.* 2002). A discovery of a companion of the exploded white dwarf, which may be, e.g., anomalously luminous during the first $\sim 10^3$–10^4 years after the explosion due to interaction with the SN shell (Marietta *et al.* 2000; Podsiadlowski 2003), would undoubtedly lend support to the explosion scenario. The post-explosion spatial velocity of the companion may be as high as $\simeq 450$ km s^{-1} (Canal *et al.* 2001).

To assess the real role of the semidetached-system channel, it is important to estimate the actual number of supersoft X-ray sources in the Milky Way and other galaxies.

The recently discovered anomalous SN Ia 2002ic (Hamuy *et al.* 2003), which has hydrogen lines in its spectrum, is apparently associated with a massive AGB object that lost several $M_\odot$ before the explosion. SN2002ic may have been either an explosion of a single star (a so-called SN 1.5 (Hamuy *et al.* 2003)), or the explosion of a degenerate component in a symbiotic system.

Our estimates of the frequency with which white dwarfs accumulate $M_{\rm Ch}$ are several times lower than, e.g., those of Hachisu *et al.* (1996, 1999) and Li and van den Heuvel (1997), who found that this frequency may be comparable to the empirical occurrence rate of SNe Ia in the Milky Way. The above authors also used formula (5) to compute the frequency of formation of close binaries, however, they did not perform any detailed population synthesis. Because of the nonlinear nature of the variation of component masses and semimajor axes of the orbits of binary systems during their evolution, simple substitution of the numerical integration of function (5) over three-dimensional space by multiplying the final expressions for the initial intervals of component masses, component mass ratios, and separations between the components, yields a substantially overestimated occurrence frequency of potential SNe Ia.

Under the "standard" assumption, $\alpha_{\rm ce} = 1$, the same population synthesis code yields a rate of 2.1×10^{-3} yr^{-1} for the mergers of binary CO dwarfs with a total mass exceeding $M_{\rm Ch}$, and an occurrence rate of 4.6×10^{-3} yr^{-1} for the detonation of helium in the degenerate layer of accreted matter at the surface of the dwarf star in systems with nondegenerate helium donors. These rates are comparable with the empirically estimated SN Ia rate in the Milky Way.

As pointed out by Yungelson and Livio (1998), the ages at the time of the SN Ia explosion; of the semidetached systems analyzed in this paper do not exceed $\simeq$2.5 Ga. The age of SNe Ia initiated by edge-lit helium detonations does not exceed $\simeq 1$ Gyr (Yungelson and Livio 2000; Regös *et al.* 2003).[2] It follows from this that semidetached systems cannot generate SNe Ia in old populations (elliptical galaxies). Mergers of binary CO-dwarfs appear thus to be the only mechanism capable of producing (super) Chandrasekhar-mass objects in stellar systems of arbitrary age.

The existence of dwarf pairs with the close-to-Chandrasekhar total masses and orbital periods sufficiently short to allow the two components to merge in a shorter-than-Hubble time is now beyond question (Napiwotzki *et al.* 2002, 2003). The number of such pairs is close to what was expected (Nelemans *et al.* 2001): three stars out of ~1000 dwarfs with $V \leq 16^{m}.5$ studied for binarity. However, whether merging triggers carbon burning near the center of the dwarf and results in a SN Ia even remains an open question.

During the coalescence of dwarfs, the less massive object is transformed into a disk surrounding a central "core." The subsequent evolution of the system is determined by the accretion rate of the disk matter, $\dot{M}_{\rm a}$. The accretion rate depends on the time scale $T_{\rm a}$ of the angular momentum transfer in the disk. The latter can be on the order of 10^9 yr if determined by the viscosity of the degenerate matter only. However, due to turbulence in the transition layer between the disk and the core, and very likely presence of magnetic field $T_{\rm a}$, it must be several orders of magnitude shorter (Mochkovitch and Livio 1990) and accretion rate has to be comparable to the limiting Eddington accretion rate ($\dot{M}_{\rm Edd} \approx 2 \times 10^{-5} M_\odot$ yr^{-1} for a $1 M_\odot$ dwarf).

The results of accretion computations are inconclusive even in the case of a one-dimensional model. Nomoto and Iben (1985) and Kawai et al. (1987) showed that carbon ignition near the center of the accretor and the SN Ia explosion when the core grows to the Chandrasekhar mass are possible only at $\dot{M}_{\rm a} \lesssim (0.1{-}0.2)\dot{M}_{\rm Edd}$. At higher $\dot{M}_{\rm a}$, carbon ignition starts in the layer of accreted matter. Carbon ignition in the layer results in the "competition" of two processes: carbon burning and the accumulation of mass by the dwarf as a result of disk accretion, allowing the following simple estimates to be obtained: The maximum burning rate with the allowance for the loss of a part (α_ν) of the released energy via neutrinos is limited by the Eddington luminosity. The accretion rate $\dot{M}_{\rm a}$ is limited by the same factor. The dwarf is capable of accumulating $M_{\rm Ch}$ before it burns to the center if

$$\frac{M_{\rm Ch} - M_{\rm a0}}{M_{\rm Ch}} \frac{\epsilon_g}{(1 - \alpha_\nu) X_C \epsilon_C} < 1. \qquad (7)$$

Here, $M_{\rm a0}$ is the initial mass of the accretor; $X_C \approx 0.5$ is the outer-layer carbon content typical of massive dwarfs; $\epsilon_C \approx 5 \times 10^{17}$ erg g^{-1} is the energy released as a result of burning 1 g of ^{12}C, and $\epsilon_g \approx 5 \times 10^{16}$ erg g^{-1} is the energy released as a result of the accretion of 1 g of disk matter. Since $\alpha_\nu \sim 0.4$ in the burning layer (Saio and Nomoto 1998), estimate (7) shows that a dwarf with $M_{\rm a0} = 1 M_\odot$ can accumulate $M_{\rm Ch}$ before it burns out all its carbon. Thus, carbon ignition in the outer layers of the dwarf may not necessarily prevent the central explosion of carbon and SN Ia. At $\alpha_\nu \gtrsim 0.9$, burning of carbon results in the formation of an oxygen-neon dwarf, which, upon accumulating $M_{\rm Ch}$, transforms into a neutron star via "silent" collapse without SN Ia explosion.

On the other hand, Dunina-Barkovskaya and Imshennik (2003) showed that at the accretion rate of $5 \times 10^{-7} M_\odot$ yr^{-1} in CO dwarfs with the initial mass $1.33{-}1.34 M_\odot$ carbon burning is possible that starts at the edge and proceeds in the delayed detonation mode. This process may result in an SN Ia explosion.

The allowance for rotation may also change the situation. Piersanti et al. (2003) showed that in the case of certain combinations of the accretion rate and angular momentum of the accreted matter, the rapidly rotating dwarf acquires the shape of a triaxial ellipsoid with a quadrupole momentum. As a result, the dwarf loses energy and angular momentum via radiation of gravitational waves and contracts creating conditions for the central explosion and SN Ia. However, adequate 3D-computations are needed to draw final conclusions.

CONCLUSIONS

We performed a detailed analysis of the frequency with which CO and ONe white dwarfs in semidetached systems with main sequence and subgiant companions grow to the Chandrasekhar mass. We

---

[2] It is not improbable that the rotation of the dwarf may prevent the detonation of the helium (Langer *et al.* 2003).

analyzed how the results of computations depend on the common envelope parameter and accretion rate. We put special emphasis on the conditions of the development of common envelopes during intermediate evolutionary stages depending on our assumptions about the character of mixing in the main-sequence star during helium accretion. We also showed that in the case of the most favorable combination of parameters, the white dwarfs of the Galactic disk accumulate $M_{\rm Ch}$ at a rate not exceeding $\simeq 2\times10^{-4}$ yr^{-1}. Thus, in our model, this channel of the formation of potential type-Ia presupernovae cannot account for more than $\simeq$10% of the total SNe Ia rate in the Milky Way. An alternative channel of presupernova formation—white dwarf mergers—is capable of ensuring the required frequency, however, the details of mergers and the explosion mechanism require a further study. These details include, among other things, the structure and evolution of the "core+disk" configuration that forms immediately after the merger; the character of burning; the transfer of mass and momentum in this configuration with allowance for the effects of viscosity and the magnetic field; the character of burning that develops during the merger; the role of neutrino losses; and rotation.

In semidetached binaries of the type considered, neutron stars may form "quietly" (also at a frequency of up to $\sim10^{-4}$ yr^{-1}) as a result of accretion-induced dwarf collapses without SN explosions. This frequency is, in principle, consistent with the constraints found by Fryer *et al.* (1999) that are due to the abundance of r-process products in the interstellar medium.

ACKNOWLEDGMENTS

We are grateful to P. Kahabka for discussing the characteristics of supersoft X-ray sources. This work was supported in part by the Russian Foundation for Basic Research (grant no. 03-02-16254) and the Federal Research and Technology Program for Astronomy.

APPENDIX

Let us make order-of-magnitude estimates of some time scales associated with helium accretion and compare them to the time scale $t_{\rm ex}\simeq10^5$ yr of the mass transfer due to the expansion of a helium star (Iben and Tutukov 1985; Bitzaraki *et al.* 2002). It would appear reasonable that shear instability during disk accretion leads to turbulization of the accreted matter. Let us assume that the typical size of helium cells is equal to the local pressure scale height in the star's envelope, H_p.

The time scale of radiative cooling of an element is

$$t_{\rm cool}\simeq\frac{H_p^2}{cl}\simeq\frac{H_p^2\kappa\rho}{c}, \qquad (A.1)$$

where c is the speed of light; l, the photon free path; κ, the opacity, and ρ, the density. Or, in solar units, we have

$$t_{\rm cool}\simeq10^{-11}\kappa\rho\left(\frac{R}{R_\odot}\right)^4\left(\frac{M}{M_\odot}\right)^2T^2\,{\rm yr}, \qquad (A.2)$$

where R and M are the radius and mass of the star, respectively and T is the temperature. For a star of mass $2M_\odot$, $t_{\rm cool}\lesssim10^3$ yr. It is evident that $t_{\rm cool}\ll t_{\rm ex}$. It follows from this that the temperature of a sinking element with a size of the local pressure scale height is actually equal to the ambient temperature.

Temperature equalization at equal pressure results in the density of the element being different from the ambient density and generation of archimedean force. By equating the force of dynamic friction $\pi H_p^2\rho v^2$ and archimedean force $(4\pi/3)H_p^3 g\Delta\rho$, we find the velocity of sinking: $v\approx c_{\rm s}\sqrt{\Delta\mu/\mu}$, where $c_{\rm s}$ is the local speed of sound. In this case, it takes the element $t_{\rm ff}\approx(R/c_{\rm s})\sqrt{\Delta\mu/\mu}$ to cross the stellar radius R. Given that, for a $2M_\odot$-mass star, time $t_{\rm ff}\simeq2$ h, and the mass-transfer time scale is equal to $t_{\rm ex}\simeq10^5$ yr, we obtain that mixing is almost instantaneous if the fractional difference between the molecular weights of the convective shell and star's envelope

$$\frac{\Delta\mu}{\mu}=\left(\frac{t_{\rm ff}}{t_{\rm ex}}\right)^2\gtrsim10^{-17}, \qquad (A.3)$$

a condition that is obviously satisfied.

Let us now estimate the rate of He diffusion from convective elements. If the element does not change its identity in the process of sinking, its characteristic radius varies as $r=(\rho_0/\rho)^{1/3}H_{p0}$, where $H_{p0}\approx10^8$ cm is the pressure scale height and $\rho_0\approx10^{-8}$ g cm^{-3} is the density of matter in the photosphere. The thermal diffusion time scale can be estimated as

$$\tau_{\rm d}\approx\frac{r^2}{v_\alpha l_\alpha}, \qquad v_\alpha=\sqrt{\frac{3kT}{\mu_\alpha}}. \qquad (A.4)$$

Here, μ_α is the mass of He nuclei; v_α, their velocity; $l_\alpha=1/\sigma n_\alpha$, the free path of nuclei; the concentration and is equal to $n=\rho/\mu_\alpha$.The cross section of the interaction of nuclei is $\sigma=16e^4/(kT)^2$, and e is the electron charge (Lang 1974). We substitute the above ρ_0 and H_{p0} values to obtain:

$$\tau_{\rm d}\approx10^{19}\frac{\rho^{1/3}}{T^{5/2}}\,{\rm yr}. \qquad (A.5)$$

The time scale $\tau_d \simeq 10^2$–10^5 yr is also much shorter than the time scale of mass transfer throughout the entire star, except possibly the uppermost envelope layers with the fractional radius $\Delta R/R \approx 0.01$. The time scale τ_d should be even shorter in the case of the fragmentation of the helium-enriched element during its sinking.

A detailed modeling of the disk accretion of helium by the star also requires an allowance for the spin-up of the star and the mass circulation induced by rotation, which also favor mixing.

The circumstances described above lead us to conclude that the “instantaneous” mixing of the accreted helium throughout the entire volume of the star is highly likely, and that the evolution of the corresponding models must be studied.

REFERENCES

1. O. M. Bitzaraki, C. A. Tout, and H. Rovithis-Livaniou, New Astron. **8**, 23 (2002).
2. R. Canal, J. Méndez, and P. Ruiz-Lapuente, Astrophys. J. **550**, L53 (2001).
3. E. Cappellaro and M. Turatto, *The Influence of Binaries on Stellar Population Studies* (Kluwer Acad., Dordrecht, 2001); Astrophys. Space Sci. Lib. **264**, 199 (2001).
4. J. D. M. Dewi and T. M. Tauris, Astron. Astrophys. **360**, 1043 (2000).
5. R. Di Stefano and A. K. H. Kong, astro-ph/03011622 (2003).
6. R. Di Stefano and S. Rappaport, ASP Conf. Ser. **72**, 155 (1995).
7. R. Di Stefano and A. K. H. Kong, Astrophys. J. **592**, 884 (2003).
8. N. V. Dunina-Barkovskaya and V. S. Imshennik, Pis'ma Astron. Zh. **29**, 13 (2003) [Astron. Lett. **29**, 10 (2003)].
9. C. R. Eck, J. J. Cowan, D. A. Roberts, *et al.*, Astrophys. J. **451**, L53 (1995).
10. C. Fryer, W. Benz, M. Herant, and S. A. Colgate, Astrophys. J. **516**, 892 (1999).
11. I. Hachisu, M. Kato, and K. Nomoto, Astrophys. J. **470**, L97 (1996).
12. I. Hachisu, M. Kato, K. Nomoto, and H. Umeda, Astrophys. J. **519**, 314 (1999).
13. I. Hachisu, M. Kato, T. Kato, *et al.*, Astrophys. J. **534**, L189 (2000).
14. M. Hamuy, M. M. Phillips, N. B. Suntzeff, *et al.*, Nature **424**, 651 (2003).
15. M. S. Hjellming and R. F. Webbink, Astrophys. J. **318**, 794 (1987).
16. I. Iben, Jr., ASP Conf. Ser. **199**, 107 (2000).
17. I. Iben, Jr. and A. V. Tutukov, Astrophys. J., Suppl. Ser. **54**, 331 (1984).
18. I. Iben, Jr. and A. V. Tutukov, Astrophys. J., Suppl. Ser. **58**, 661 (1985).
19. P. Kahabka, *Compact Stellar X-ray Sources,* Ed. by W. Lewin and M. van der Klis (Cambridge, 2003, in press); astro-ph/0212037.
20. M. Kato and I. Iben, Jr., Astrophys. J. **394**, L47 (1992).
21. M. Kato and I. Hachisu, Astrophys. J. **437**, 802 (1994).
22. M. Kato and I. Hachisu, Astrophys. J. **513**, L41 (1999).
23. Y. Kawai, H. Saio, and K. Nomoto, Astrophys. J. **315**, 229 (1987).
24. R. Kippenhahn, G. Ruschenplatt, and H.-C. Thomas, Astron. Astrophys. **91**, 175 (1980).
25. N. D. Kylafis and D. Q. Lamb, Astrophys. J., Suppl. Ser. **48**, 239 (1982).
26. K. R. Lang, *Astrophysical Formulae: a Compendium for the Physicist and Astrophysicist* (Springer, Berlin, 1974; Mir, Moscow, 1978).
27. N. Langer, A. Deutschmann, S. Wellstein, and P. Höflich, Astron. Astrophys. **362**, 1046 (2000).
28. N. Langer, S.-C. Yoon, and J. Petrovic, *IAU Symp. No. 215: Stellar Rotation,* Ed. by A. Maeder and P. Eenens (2003, in press); astro-ph/0302232.
29. E. J. Lentz, E. Baron, P. H. Hauschildt, and D. Branch, Astrophys. J. **580**, 374 (2002).
30. X.-D. Li and E. P. J. van den Heuvel, Astron. Astrophys. **322**, L9 (1997).
31. W. Li, A. V. Filippenko, R. R. Treffers, *et al.*, Astrophys. J. **546**, 734 (2001).
32. E. Livne, Astrophys. J. **354**, L53 (1990).
33. E. Marietta, A. Burrows, and B. Fryxell, Astrophys. J., Suppl. Ser. **128**, 615 (2000).
34. R. Mochkovitch and M. Livio, Astron. Astrophys. **236**, 378 (1990).
35. U. Munari and A. Renzini, Astrophys. J. **397**, L87 (1992).
36. R. Napiwotzki, D. Koester, G. Nelemans, *et al.*, Astron. Astrophys. **386**, 957 (2002).
37. R. Napiwotzki, N. Christlieb, H. Drechsel, *et al.*, ESO Messenger **112**, 25 (2003).
38. G. Nelemans, F. Verbunt, L. R. Yungelson, and S. F. Portegies Zwart, Astron. Astrophys. **360**, 1011 (2000).
39. G. Nelemans, L. R. Yungelson, S. F. Portegies Zwart, and F. Verbunt, Astron. Astrophys. **365**, 491 (2001).
40. K. Nomoto and I. Iben, Jr., Astrophys. J. **297**, 531 (1985).
41. K. Nomoto and Y. Kondo, Astrophys. J. **367**, L19 (1991).
42. L. Piersanti, S. Gagliardi, I. Iben, Jr., and A. Tornambé, Astrophys. J. **583**, 885 (2003).
43. P. Podsiadlowski, astro-ph/0303660 (2003).
44. D. Prialnik and A. Kovetz, Astrophys. J. **445**, 789 (1995).
45. S. Rappaport, R. Di Stefano, and J. D. Smith, Astrophys. J. **426**, 692 (1994).
46. E. Regös, C. A. Tout, D. Wickramasinghe, *et al.*, New Astron. **8**, 283 (2003).
47. H. Saio and K. Nomoto, Astrophys. J. **500**, 388 (1998).

48. M. J. Sarna, E. Ergma, and J. Gerskevits, AIP Conf. Proc. **637**, 47 (2002); astro-ph/0010259.
49. N. Soker, Mon. Not. R. Astron. Soc. **336**, 1229 (2002).
50. R. Stothers and N. R. Simon, Astrophys. J. **157**, 673 (1969).
51. T. Tauris and J. D. M. Dewi, Astron. Astrophys. **369**, 170 (2001).
52. T. D. Thoroughgood, V. S. Dhillon, S. P. Littlefair, *et al.*, Mon. Not. R. Astron. Soc. **327**, 1323 (2001).
53. A. V. Tutukov and A. V. Fedorova, Astron. Zh. **78**, 1008 (2001) [Astron. Rep. **45**, 882 (2001)].
54. A. V. Tutukov and L. R. Yungelson, Astrofizika **12**, 521 (1976).
55. A. V. Tutukov and L. R. Yungelson, Nauchn. Inform. Astron. Soveta Akad. Nauk SSSR **49**, 3 (1981).
56. A. V. Tutukov, A. V. Fedorova, and L. R. Yungelson, Pis'ma Astron. Zh. **8**, 365 (1982) [Sov. Astron. Lett. **8**, 198 (1982)].
57. R. K. Ulrich, Astrophys. J. **172**, 165 (1972).
58. E. P. J. van den Heuvel, D. Bhattacharya, K. Nomoto, and S. A. Rappaport, Astron. Astrophys. **262**, 97 (1992).
59. R. F. Webbink, Astrophys. J. **277**, 355 (1984).
60. J. Whelan and I. Iben, Jr., Astrophys. J. **186**, 1007 (1973).
61. L. R. Yungelson and M. Livio, Astrophys. J. **497**, 168 (1998).
62. L. R. Yungelson and M. Livio, Astrophys. J. **528**, 108 (2000).
63. L. Yungelson, M. Livio, J. W. Truran, *et al.*, Astrophys. J. **466**, 890 (1996).

Translated by A. Dambis

Astronomy Letters, Vol. 30, No. 2, 2004, pp. 86–94. Translated from Pis'ma v Astronomicheskiĭ Zhurnal, Vol. 30, No. 2, 2004, pp. 105–115.
Original Russian Text Copyright © 2004 by Arefiev, Aleksandrovich.

Type-I X-ray Bursts from Voids: Tracers of Weakly Accreting Bursters?

V. A. Arefiev[*] **and N. L. Aleksandrovich**

Space Research Institute, ul. Profsoyuznaya 84/32, Moscow, 117997 Russia

Received June 20, 2003

Abstract—We obtained long-term (10–20 years) light curves for seven X-ray bursters. These sources exhibited no prolonged episodes of luminosities exceeding several percent of the Eddington luminosity over the entire observing period. For four sources, we found upper limits for the luminosity of over 5 years. These limits proved to be below 10^{36} erg s^{-1}. We estimated the total number of such sources in our Galaxy.

Key words: *X-ray bursters.*

INTRODUCTION

Short intense X-ray bursts that reached the Eddington luminosity at their maxima and that lasted from tens to hundreds of seconds (the so-called type-I X-ray bursts) have been observed from many X-ray binaries. Such bursts are the result of the nonstationary thermonuclear burning of material accreted on the surface of a neutron star (Woosley and Taam 1976). They exhibit a sharp rise, a subsequent slower decay of the X-ray flux, and a gradual softening of the radiation spectrum at the decay phase. The sources showing X-ray bursts are called X-ray bursters. In general, bursters generate bursts when their luminosities outside a burst are 10^{36}–10^{37} erg s^{-1}. The detection of a type-I X-ray burst is believed to be sufficient evidence that the compact object in the binary is a neutron star.

Recently, during long-term observations of the Galactic-center region performed in the period 1996–2001, the wide-field X-ray cameras onboard the BeppoSAX satellite detected X-ray bursts from places from which no persistent emission was recorded over the entire observing period (in't Zand *et al.* 1998; Cocchi *et al.* 1999). Cocchi *et al.* (2001) assumed that such bursts from voids are generated by a new class of X-ray sources—weakly accreting X-ray bursters, i.e., bursters with luminosities outside bursts of below 10^{35} erg s^{-1}, which roughly corresponds to the BeppoSAX detection threshold. Subsequent short-term observations of burst regions from the Chandra Observatory (Cornelisse *et al.* 2002a) revealed no sources brighter than $\sim10^{32}$ erg s^{-1}, which indirectly confirms this assumption.

The combination of a low luminosity outside bursts and a long time interval between successive bursts makes it difficult to detect such objects. Therefore, although only a few probable weakly accreting bursters have been found, their total number in our Galaxy may be much (tens or hundreds of times) larger than the number of normal bursters. If there are actually many weakly accreting bursters, then they can contribute significantly to the number of fast X-ray transients, i.e., sources that exhibit episodes of intense X-ray outbursts and are not detectable outside such episodes (Arefiev *et al.* 2003).

To estimate the burst rate as a function of the luminosity or the total number of weakly accreting objects, it is important to perform long-term observations, because the accretion rate may have changed significantly over the previous years or tens of years, and these bursters are weakly accreting objects only during a relatively short period. Ideal instruments for this purpose are the TTM X-ray telescope, which carried out regular intensive observations of several regions of the sky where bursts from voids were observed in the period 1988–1995, and the ASM/RXTE X-ray monitor, which has been operating in orbit since 1996. Together with the ASM/RXTE data, the TTM observations span more than ten years.

In this paper, we present the TTM observational data and systematize the observations carried out from BeppoSAX, ASM/RXTE, and several other satellites for seven X-ray sources that may be classified as weakly accreting X-ray bursters.

OBSERVATIONS

The regions of the sky with bursts from voids were observed mainly with the TTM, WFC/BeppoSAX, and ASM/RXTE.

The TTM coded-aperture X-ray telescope (Brinkman *et al.* 1985) is sensitive in the energy range of

---

[*] E-mail: `gita@hea.iki.rssi.ru`

2–30 keV and has a 15° × 15° total field of view. The 5σ sensitivity for a source at the center of the field of view is $\sim$7–10 mCrab during a single ($\sim$20 min) session if there are no other bright sources within the field. The TTM sensitivity decreases significantly if there are other bright sources within the field or if the source under study is at the edge of the field. In the energy range of 2–30 keV, 1 mCrab is $\sim 3.7 \times 10^{-11}$ erg s^{-1} cm^{-2}.

The WFC/BeppoSAX wide-field camera is sensitive in the energy range of 1.8–28 keV and has a 20° × 20° (FWHM) field of view (Jager *et al.* 1997). The 5σ BeppoSAX sensitivity is $\sim$200 mCrab in 8 s. The total observing time for most of the sources was more than 10^5 s; the sensitivity of the wide-field cameras reached several mCrab.

The ASM/RXTE X-ray monitor is sensitive in the energy range of 2–12 keV. Its sensitivity limit in 1 day is several mCrab. The ASM electronic archive (http://heasarc.gsfc.nasa.gov/xte_weather/) contains data on the light curves of these sources averaged over 1 day of observations. The ASM light curves are available both in the total range and in one of the three energy channels: channel A, 2–3 keV (occasionally given as 1.5–3 keV); channel B, 3–5 keV; and channel C, 5–12 keV. For the Crab Nebula, the ASM flux is 26.8, 23.3, 25.4, and the sum is 75.5 counts s^{-1}, which is 2.8×10^{-8} erg s^{-1} cm^{-2} in the energy range of 1.5–12 keV.

The wide-field X-ray cameras onboard the BeppoSAX satellite recorded X-ray bursts from ten sources from which no persistent flux was detected at the burst recording time. For seven of these sources observed with TTM, Table 1 gives data on the distances, absorption column densities, and the bursts recorded by BeppoSAX. The TTM data for these sources are given in Table 2.

In the original papers, the distances to the sources were determined from the burst transition to a super-Eddington regime, i.e., if evidence of photospheric expansion was observed at the burst time. If no such evidence was observed, then the listed distances are upper limits, assuming the Eddington luminosity at the burst peak. Since all estimates were obtained for an Eddington luminosity of 2×10^{38} erg s^{-1}, they can differ from the values given in the original papers. The hydrogen atomic column densities were taken from the original papers or obtained by interpolating the hydrogen density distribution in the Galaxy from the HEASARC electronic data archive (http://heasarc.gsfc.nasa.gov; adapted from Dickey and Lockman (1990)). The ratio of the burst peak flux to the persistent flux is given for the most intense burst if more than one burst was observed from the source. For all sources, the persistent flux was determined as a 3σ upper limit. In determining the upper limit, we assumed that the photon spectrum outside a burst was described by a power law with an index of $\alpha = 2$ and an absorption from Table 1. In what follows, to determine the fluxes from the sources outside burst, we use the same assumption, unless specified otherwise. Table 1 also gives the number of detected bursts and the total observing time of each source with the BeppoSAX cameras.

Figure 1 shows the light curves of the source, as constructed from ASM/RXTE and TTM data (upper limits), and the BeppoSAX upper limit at the time of burst observation. Peculiarities of the observations for individual sources are given below.

1RXS J1718.4–4029. BeppoSAX (Kaptein *et al.* 2000) detected only one X-ray burst at a distance of $0\overset{'}{.}3$ from the ROSAT source, 1RXS J1718.4–4029 (Voges *et al.* 1999), in September 1996. The ASM/RXTE nondetection confirms that the source 1RXS J1718.4–4029 did not show any periods with a luminosity above several mCrab in the energy range of 2–10 keV over ten years of its observations. If the luminosity of the source was at the level recorded by ROSAT (see Fig. 1b), then the flux ratio at the burst time (Table 1) must be approximately an order of magnitude higher. For a distance of 6.5 kpc, the persistent luminosity was then about 5×10^{34} erg s^{-1}.

SAX J1806.5–2215. TTM observed the error region of X-ray bursts in several observing sessions from 1988 until 1995. In the session of October 20, 1992, the source was identified at a 3.1σ (35.8 ± 11.7 mCrab) level. The light curve of the source is shown in Fig. 1d.

GRS 1741.9–2853. Persistent emission from the source GRS 1741.9–2853 at a 9.6-mCrab level in the energy range of 4–20 keV was recorded only once, in March 1990, by the ART-P X-ray telescope onboard the Granat Astrophysical Observatory (Pavlinsky *et al.* 1994).

SAX J1753.5–2349. We analyzed the PCA/RXTE data available for this source. SAX J1753.5–2349 is located near the Galactic center, where a significant contribution is made by Galactic ridge emission. Thus, the detection of an emission from this region by PCA with a 1° field of view does not suggest that the flux originates from the source proper. For this purpose, we used scanning data from the observatory. In this case, a weak point source can be identified against the background of Galactic ridge emission. The source was observed in three sessions, between MJD 51269.8 and MJD 51481.2. The mean flux from the source was about 1.6 mCrab in the energy range of 3–20 keV. The PCA data are indicated by triangles in Fig. 1g.

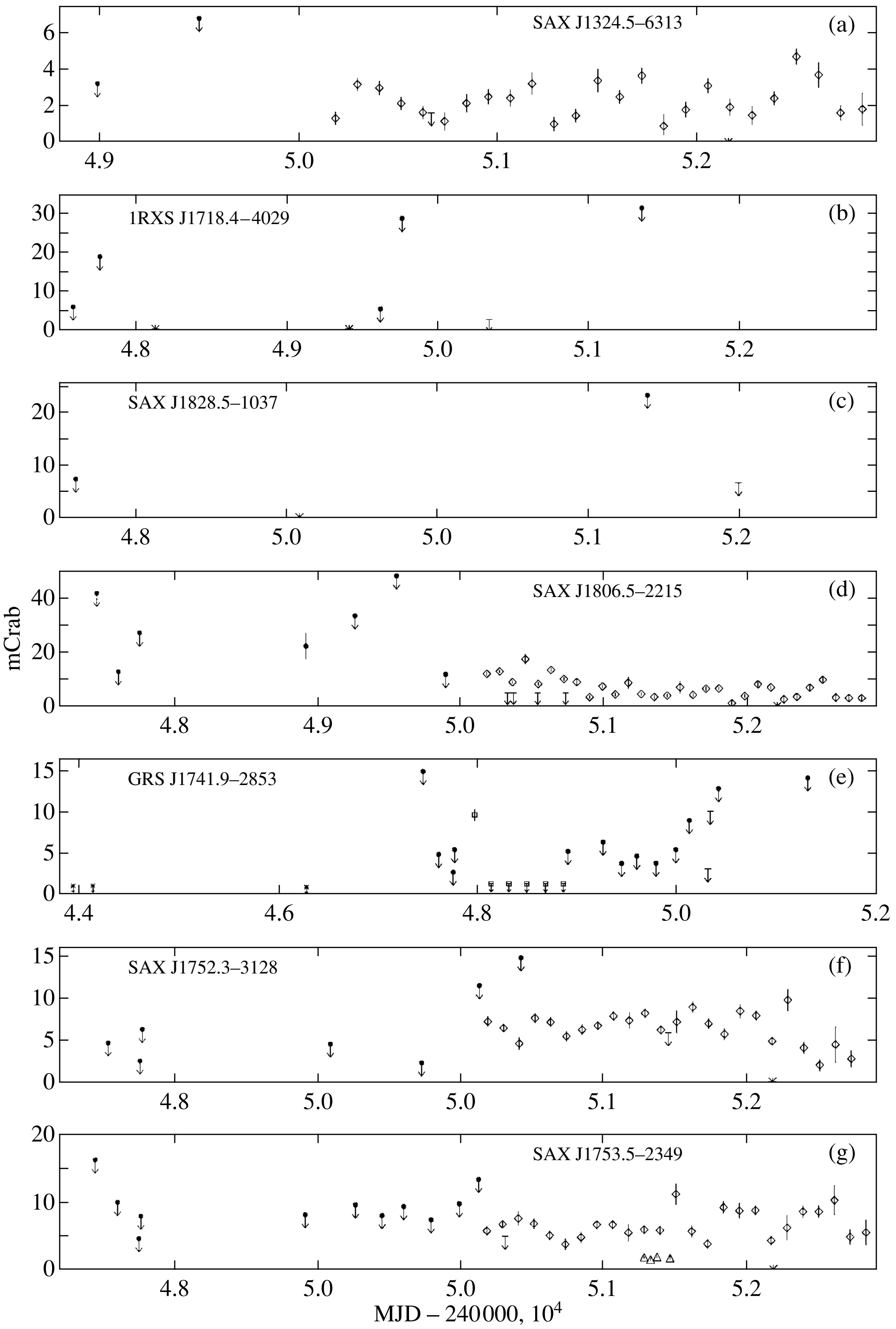

Fig. 1. Light curves for the X-ray bursters: the filled circles are TTM data; the diamonds are ASM data; and the horizontal bars are BeppoSAX data with 1σ errors. The arrows indicate 3σ detection upper limits; (a) SAX J1324.5–6313, the asterisk for Chandra (Cornelisse *et al.* 2002b); (b) 1RXS J1718.4–4029, the asterisk for ROSAT (Voges *et al.* 1999); (c) SAX J1828.5–1037, the asterisk for ROSAT (Cornelisse *et al.* 2002a); (d) SAX J1806.5–2215, the asterisk for Chandra (Cornelisse *et al.* 2002b); (e) GRS 1741.9–2853, the squares for ART-P (Pavlinsky *et al.* 1994), the asterisks for Einstein (Watson *et al.* 1981) and EXOSAT (Warwick *et al.* 1988); (f) SAX J1752.3–3128, the asterisk for Chandra (Cornelisse *et al.* 2002b); (g) SAX J1753.5–2349, the asterisk for Chandra (Cornelisse *et al.* 2002b), the triangles for PCA/RXTE.

Table 1. Data on the sources observed with TTM

Source	Distance, kpc	Equivalent hydrogen column density, $\times 10^{21}$ cm^{-2}	Number of BeppoSAX bursts/ observing time, s	Burst/persistent flux ratio for BeppoSAX
SAX J1324.5-6313	<6.2	15	$1/1.85\times10^4$	$>770^b$
1RXS J1718.4-4029	6.5	9.2	$1/5.5\times10^5$	$>430^c$
GRS 1741.9-2853	7.2	60	$3/2\times10^6$	$>100^d$
SAX J1752.3-3138	8.2	5.64	$1/4\times10^6$	$>110^d$
SAX J1753.5-2349	<8.8	8.3	$1/4\times10^6$	$>180^e$
SAX J1806.5-2215	<8.0	12	4^a	$>380^{e,f}$
SAX J1828.5-1037	<6.2	19	$1/4.02\times10^4$	$>320^b$

[a] The total observing time is unknown.
[b] Cornelisse *et al.* (2002a).
[c] Kaptein *et al.* (2000).
[d] Cocchi *et al.* (1999).
[e] in't Zand (1998).
[f] Cornelisse *et al.* (2002b).

ANALYSIS

We see from the data shown in Fig. 1 that the ASM/RXTE fluxes are systematically higher than the Chandra fluxes. This discrepancy can be explained as follows: (1) the fluxes restored from ASM data are systematically overestimated; (2) since the spectra of the sources differ significantly from the spectrum of the Crab Nebula, the flux is overestimated or underestimated when expressed in mCrab units in a different energy range; and (3) the sources are highly variable on time scales from several ks (the characteristic Chandra observing time) to several days. Below, we briefly consider these possibilities.

Restoration Errors of the ASM *Data*

There are several reasons why the fluxes restored from ASM data may prove to be overestimated: (1) there is uncertainty over the exact lower limit of the ASM soft energy channel (according to various data, it ranges from 1.5 to 2 keV); (2) most of the detected weakly accreting bursters are located in densely populated regions, and ASM may have measured the total flux from several sources; and (3) it is likely that ASM cannot accurately identify a weak point source against the background of a strong ridge emission near the Galactic plane.

Remillard (2003) points out that, within about 15° of the Galactic centre, ASM gives overestimated fluxes for "zero" sources. The restored flux from a source with an intensity below the ASM detection threshold can reach 5 mCrab near the Galactic center and 1 mCrab at distances of more than 15° from it. Clear examples are the PCA/RXTE observations carried out on MJD 51300–51500. We see from Fig. 1g that the average PCA (triangles) flux from SAX J1753.5–2349 was about 4 mCrab lower than the ASM one.

The reasons given above do not rule out the possibility of a physical explanation based on spectral or temporal properties of the sources for the difference between the ASM and Chandra estimates, but force us to treat them with caution.

Spectral Variations

Campana *et al.* (1998a) presented the results of the spectral evolution of the X-ray burster Aql X-1 when its luminosity changed by six orders of magnitude. For a nearly Eddington luminosity, the spectrum is relatively soft, with $kT_{\rm br}\sim 5$ keV. As the luminosity decreases to 10^{35}–10^{36} erg s^{-1}, a high-energy power-law component appears; it extends to $\sim$100 keV with a photon index of $\alpha\sim 2$. As the luminosity decreases further to 10^{32}–10^{33} erg s^{-1}, the spectrum again changes and can be described by soft and hard components. The temperature of the soft component is $kT_{\rm bb}\sim 0.3$ keV, while the hard component is a power-law one, with a photon index of $\alpha\sim$ 1–2; the spectrum becomes harder when the luminosity drops below 10^{33} erg s^{-1}. However, based on Chandra observations, Rutledge *et al.* (2002) found that in half of the observing sessions at a low luminosity, the source Aql X-1 exhibited a one-component

Table 2. TTM observations

Date of observations	MJD = JD−2400000.5	Accumulation time, min	Number of sessions	Upper 3σ flux limit, mCrab
SAX J1324.5−6313				
Jan. 03−10, 1993	48993.996	257.9	14	3.2
May 30−June 02, 1994	49503.636	91.5	6	6.8
1RXS J1718.4−4029				
Feb. 11−Apr. 02, 1989	47593.736	98.7	5	6.2
Aug. 22−Sep. 12, 1989	47770.813	145.0	9	19.0
Sep. 24−Oct. 11, 1994	49627.500	293.1	15	5.7
Feb. 22−24, 1995	49771.656	38.4	2	28.8
June 29−July 02, 1999	51359.756	31.2	2	31.6
GRS 1741.9−2853				
Oct. 21, 1988	47455.586	46.9	4	14.9
Mar. 20−Apr. 01, 1989	47611.758	108.6	5	4.8
Aug. 16−23, 1989	47757.791	596.5	31	2.6
Aug. 31−Sep. 05, 1989	47771.604	171.1	16	5.4
Oct. 17−26, 1992	48916.852	171.0	13	5.2
Sep. 26−Oct. 24, 1993	49270.001	117.6	6	6.3
Mar. 14−May 15, 1994	49456.405	253.6	13	3.7
Aug. 29−Sep. 28, 1994	49608.437	145.2	7	4.6
Feb. 16−Apr. 30, 1995	49800.673	249.7	12	3.7
Sep. 12−Nov. 04, 1995	49998.977	139.1	7	5.4
Feb. 06−Mar. 05, 1996	50133.489	206.6	11	8.9
Sep. 20, 1996−Feb. 24, 1997	50424.691	66.3	4	12.8
Apr. 05−June 27, 1999	51315.108	26.0	2	14.1
SAX J1752.3−3128				
Oct. 21, 1988−Apr. 01, 1989	47536.642	155.5	12	4.9
Aug. 16−23, 1989	47757.791	596.5	31	2.7
Aug. 31−Sep. 10, 1989	47774.212	248.8	23	6.5
Oct. 17, 1992−Oct. 03, 1993	49087.913	257.4	17	4.7
Mar. 15, 1994−Nov. 04, 1995	49726.153	748.4	37	2.4
Feb. 06−Mar. 05, 1996	50133.489	206.6	11	11.6
Sep. 20, 1996−Feb. 24, 1997	50424.691	66.3	4	14.9
June 27, 1999	51356.643	10.0	1	20.9
SAX J1753.5−2349				
Oct. 21, 1988	47455.586	46.9	4	16.4
Mar. 19−Apr. 01, 1989	47611.284	136.9	11	10.1
Aug. 16−23, 1989	47757.695	499.0	26	4.7
Aug. 31−Sep. 05, 1989	47771.604	171.1	16	8.0
Oct. 17−26, 1992	48916.852	171.0	13	8.2
Sep. 26−Oct. 24, 1993	49270.001	117.6	6	9.7
Mar. 14−May 15, 1994	49456.405	253.6	13	8.1
Aug. 29−Sep. 28, 1994	49608.437	145.2	7	9.4
Feb. 16−Apr. 30, 1995	49800.673	273.3	13	7.5
Sep. 12−Nov. 04, 1995	49998.977	139.1	7	9.8
Feb. 06−Mar. 05, 1996	50133.489	206.6	11	13.4
Sep. 20, 1996−Feb. 24, 1997	50424.691	66.3	4	25.4
Apr. 05−June 27, 1999	51315.108	26.0	2	33.8
SAX J1806.5−2215				
Oct. 21, 1988	47455.586	46.9	4	41.8
Mar. 19−20, 1989	47604.836	28.3	3	12.8
Aug. 16, 1989	47754.394	134.6	7	27.1
Nov. 17−20, 1992*	48913.895	74.6	5	22.2 ± 4.8
Sep. 26−Oct. 03, 1993	49259.532	86.4	4	33.3
May 06−Sep. 28, 1994	49550.726	112.1	5	48.2
Apr. 03−Sep. 16, 1995	49893.556	140.2	7	11.8
SAX J1828.5−1037				
Mar. 17−18, 1989	47602.893	33.2	3	7.4
July 29, 1999	51388.369	24.7	1	23.3

* In the session of October 20, 1992, the source was identified at a 3.1σ (35.8 ± 11.7 mCrab) level.

spectrum described by the model of a hydrogen atmosphere (Zavlin *et al.* 1996).

According to ASCA data (Asai *et al.* 1996, 1998), the X-ray burster Cen X-4 at a luminosity of 2–3×10^{32} erg s^{-1} (in the energy range of 0.5–10 keV) also exhibited a two-component spectrum consisting of a blackbody component with a temperature $kT_{\rm bb} \sim$ 0.15 keV and a power-law component with a photon index $\alpha \sim 2$; the intensities of both components were approximately equal. BeppoSAX also observed Cen X-4 with similar parameters of the spectrum and flux (Campana *et al.* 2000).

The spectrum of a neutron star at luminosities of 10^{32}–10^{33} erg s^{-1} can be formed by various physical mechanisms and, therefore, it can differ in shape (see, e.g., Campana *et al.* 1998b). The most likely mechanisms are accretion onto the surface of a neutron star, accretion up to the radius of the magnetosphere (and when the centrifugal barrier is closed, the propeller regime), nonthermal radiation generated by the energy losses of a rapidly rotating neutron star, and thermal radiation from a cooling neutron star. Only the last spectrum formation mechanism generates a one-component thermal spectrum; the three remaining mechanisms suggest the presence of an additional hard power-law component. However, in the absence of accretion (or at its low rates), Zavlin *et al.* (1996) showed that, for neutron stars with a weak magnetic field, an allowance for the influence of the neutron-star atmosphere on the thermal spectrum emitted from the surface leads to a significant change in the spectrum. This influence depends on the chemical composition of the atmosphere, but, in general, in addition to the thermal component, a hard component that can reach the intensity of the thermal component is formed. Thus, for luminosities of up to 10^{32}–10^{33} erg s^{-1}, the spectrum exhibited by Aql X-1 and Cen X-4 may also be expected from other bursters, irrespective of the specific spectrum generation mechanism.

We have at our disposal ASM/RXTE data on four probable weakly accreting bursters (SAX J1324.5–6313; SAX J1752.3–3138; SAX J1753.5–2349; SAX J1806.5–2215), all of which were observed at a luminosity well below the Eddington limit. Indeed, in several cases, the ratio of the burst peak flux to the upper limit on the persistent flux reached several hundred (Table 1). It is well known that the maximum of the luminosity amplitude at the burst time cannot exceed the Eddington limit, which is $\sim 2 \times 10^{38}$ erg s^{-1} for a neutron star of mass $1.4 M_{\odot}$. Thus, the persistent flux from the neutron stars over the time of burst observation did not exceed $\sim 10^{35}$–10^{36} erg s^{-1}. For most of the sources, the bursts did not reach the Eddington limit; therefore, the luminosity outside the bursts was even lower. As a result, if the spectra of these bursters are assumed to evolve with changing luminosity like Aql X-1 and Cen X-4, then they may be considered to be power-law ones in the luminosity range in which they were observed by ASM.

We plotted the X-ray color–color diagram for these sources (Fig. 2). The hard color is defined as the difference between the counts in channels C–B, while the soft color is defined as the difference between the counts in channels B–A normalized to the total flux. All errors are given at a 1σ level. To take into account the systematic overestimation of the ASM fluxes near the Galactic centre, which decreases with increasing distance from it, we subtracted the persistent flux from the ASM data: 1 mCrab for SAX J1806.5–2215 and SAX J1324.5–6313 and 3 mCrab for SAX J1752.3–3138 and SAX J1753.5–2349. For comparison, the uncorrected values are indicated by asterisks. On the color–color diagram, the intersection of the dashed lines indicates the value that corresponds to the spectrum of the Crab Nebula. We see that the experimental data points tend to cluster in the upper left quadrant for all sources. This region corresponds to a two-component spectrum with a power-law component that is slightly harder than the spectrum of the Crab Nebula (i.e., $\alpha \leq 2$) and with an additional soft component.

In any case, it seems unlikely that the discrepancy between the Chandra and ASM data could be explained only by the spectra of the sources. At the same time, the discrepancy between the ASM and PCA data for SAX J1753.5–2349 can be explained by the fact that the 12–20-keV flux from the source falls sharply.

Variability of a Weakly Accreting Source

A possible explanation of the discrepancy between the Chandra and ASM/RXTE data can be strong variability of the source on time scales of several days. If the source spends most of the time at low luminosities, which are occasionally accompanied by a short-duration increase in the flux by several factors (orders of magnitude), then the flux averaged over a long time turns out to be much higher than the flux in the state in which the source spends most of its time. The possibility of this explanation is suggested by the observations of Cen X-4 at minimum luminosity. Campana *et al.* (2000) found that the variability observed on times cales of several days was higher than the variations in average values on long time scales.

To check this possibility, we constructed the probability density functions for the stay of the source

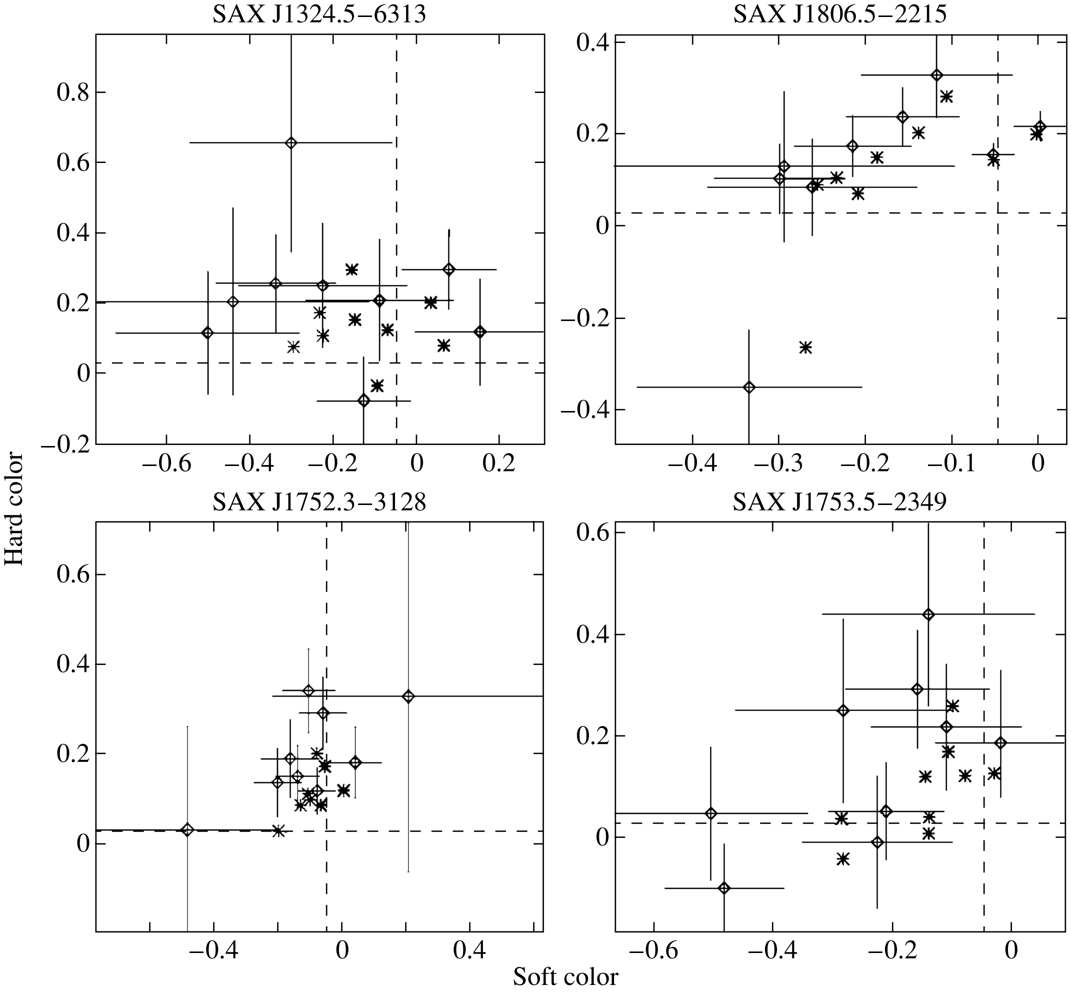

Fig. 2. Color–color diagram: hard color—(C−B)/(A+B+C); soft color—(B−A)/(A+B+C). The intersection of the dashed lines corresponds to a power-law spectrum with an index of $\alpha = 2$. The asterisks indicate data for the uncorrected spectrum.

in a state with a certain flux. If the source spends most of the time at low fluxes, occasionally exhibiting episodes of a higher luminosity, the distribution must be asymmetric, with the maximum at low luminosities and with a long tail at high luminosities. The distributions for our sources look precisely like this (for the Crab Nebula, as expected for a persistent source, we obtained a narrow, normally distributed peak). To eliminate the influence of a nonzero detection threshold for isolating weak signals near the ASM threshold, we took the integrated fraction of the time the source stays in a state below 3 mCrab as an estimate of the distribution, which roughly corresponds to the ASM detection threshold in one day, and found that this fraction varies within the range of 0.14–0.29 for five sources. The change in threshold to 1 or 5 mCrab has only a weak effect. This probability is high enough to explain the discrepancy between the Chandra and ASM data for one source. The probability that all sources were at a luminosity below 3 mCrab at the time of observations is then 2.9×10^{-4}, which seems unlikely.

We also tested the local distributions near the Chandra observations, because some of the sources may have been at a low mean luminosity for a long time during the Chandra observations. To check this possibility, we constructed the probability density functions for the stay at a given luminosity level in a 200-day-long interval including the time of Chandra observations. Indeed, the local probability of stay at a level below 3 mCrab increased by 1/3 for SAX J1753.5−2349 and SAX J1806.5−2215 and by a factor of 2, being 0.29 instead of 0.15, for SAX J1752.3−3138.

Thus, for SAX J1752.3−3138 as well as for SAX J1753.5−2349 and SAX J1806.5−2215, the discrepancy between the Chandra and ASM estimates can be explained in part by the strong variability of the sources.

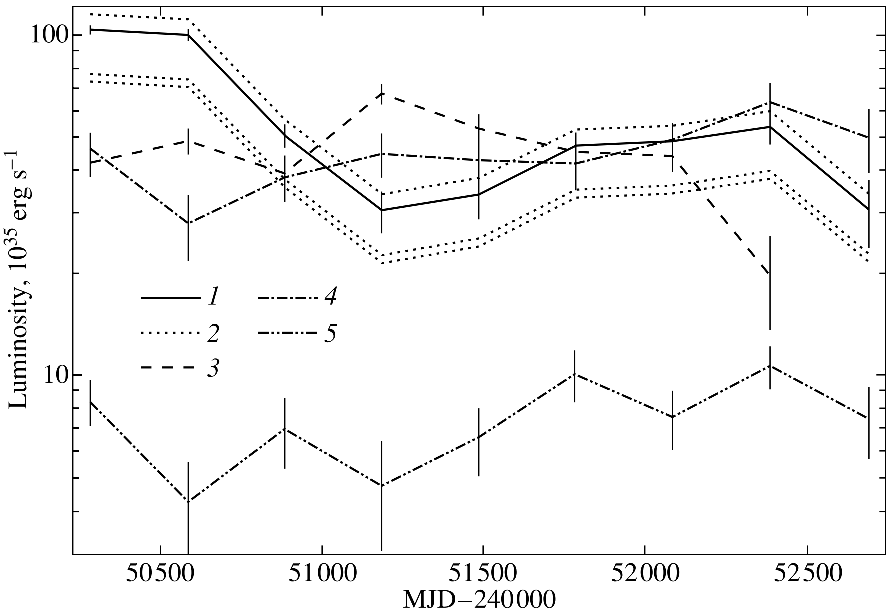

Fig. 3. Restored luminosity curves for the two-component (thermal and power-law) spectrum: (1) SAX J1806.5−2215 ((2) for different forms of the one-component spectrum of the source), (3) SAX J1752.3−3128, (4) SAX J1753.5−2349, (5) SAX J1324.5−6313.

Light Curves in Luminosity Units

To analyze the behavior of weakly accreting bursters, it would be of interest to construct their light curves in luminosity units. For the sources for which ASM data are available, we chose a two-component model of the spectrum that included a soft blackbody component with a temperature $kT_{\rm bb} \sim 0.3$ keV and a hard power-law component with an index of $\alpha \sim 1.5$. The intensity ratio of the two components in the energy range of 0.5–20 keV was 1/3. For the interstellar absorption and distance to the sources, we took the values from Table 1. The derived 0.5–20-keV light curves averaged over 300 days of observations and corrected, by analogy with Fig. 2, for the overestimation of the ASM data are shown in Fig. 3. We see that the sources exhibit a luminosity below $\sim 10^{36}$ erg s^{-1}.

Clearly, if the source spectrum exhibits no such intense blackbody component with a low temperature (which is effectively absorbed by the interstellar medium) then the restored intrinsic luminosity will be lower. We restored the light curves for SAX J1806.5−2215 for the cases where only a power-law component with different photon indices (1.0, 2.0, and 2.5) was present. As would be expected, all of the light curves for the hard one-component power-law spectrum lie below the two-component light curve (dashed line). The scatter of values does not exceed a factor of 2 or 3.

Since only upper limits on the distances are known for all of the sources (except for SAX J1324.5−6313), we may say that Fig. 3 shows upper limits on the intrinsic luminosities of weakly accreting bursters. Taking into account the data on other bursters and the TTM data, we may say that the sources exhibited no episodes of prolonged activity with a luminosity above 10^{36} erg s^{-1}.

The Total Number of Bursts from Bursters with a Low Average Luminosity

Type I X-ray bursts from voids (from which no persistent emission was observed) could be naturally classified as fast X-ray transients. We can estimate how many such bursts from voids are observed in a year in the entire sky by using BeppoSAX data (in't Zand 2001). BeppoSAX observed the Galactic-center region for $T_{\rm obs} = 4 \times 10^6$ s and detected about 1500 type I X-ray bursts from $N_{\rm b} = 31$ sources. During the same period, $B_{\rm e} = 11$ X-ray bursts were observed from seven voids. If all these events occurred on weakly accreting X-ray neutron stars, and if their spatial distribution follows the spatial distribution of normal X-ray bursters, then we can estimate the total number of X-ray bursts from voids in a year in the entire sky as $N_{\rm sky} = (1\ \text{year}/T_{\rm obs}) \times (N_{\rm t}/N_{\rm b}) \times B_{\rm e} \sim 150$ events, where $N_{\rm t} \sim 50$ is the total number of known bursters. If the distribution of weakly accreting X-ray neutron stars is isotropic, then the number of bursts from voids will be by an order of magnitude higher. This simplified estimate agrees well with the estimate obtained from BeppoSAX data by Cornelisse *et al.* (2002a). They found that the total number of such sources in the Galaxy is between 30 and 4000, and the burst recurrence time is half a year (for 30 sources) or several tens of years (for 4000 sources).

CONCLUSIONS

We obtained long-term (10–20 years) light curves for seven weakly accreting X-ray bursters. Because of the lack of accurate distances to the sources and long-term sensitive measurements, we cannot accurately estimate the mean luminosities. For four sources, we found upper limits on the luminosities of over 5 years. They turned out to be lower than 10^{36} erg s^{-1}. If we underestimated the systematic overestimation of the ASM fluxes near the Galactic center, then the upper limits on the mean luminosities decrease to 10^{35} erg s^{-1}.

Since most of the observations carried out in high-sensitivity experiments have yielded upper limits on the source luminosities of 10^{32}–10^{34} erg s^{-1}, these sources probably spend much of their time at low luminosities. Seven sources with burst-to-persistent flux ratios >100 exhibited no prolonged high-luminosity episodes throughout the observations. Thus, the observations of type I X-ray bursts from voids with a large ratio of the burst flux to the upper limit on the persistent flux are indicative of the presence of an X-ray burster with a low persistent luminosity in this region. However, the available results give no reason to assert that the detected bursters belong to the new, special class of weakly accreting bursters. A more detailed analysis requires long-term regular observations of these sources in experiments with sensitivities that are two to three orders of magnitude higher than those of modern X-ray monitors.

ACKNOWLEDGMENTS

The ASM/RXTE observational data were retrieved from the ASM electronic data archive (http://heasarc.gsfc.nasa.gov/xte_weather/). This work was supported in part by the Russian Foundation for Basic Research (project no. 01-02-17295).

REFERENCES

1. V. Arefiev, W. Priedhorsky, and K. Borozdin, Astrophys. J. **586**, 1238 (2003).
2. K. Asai, T. Dotani, K. Mitsuda, *et al.*, Publ. Astron. Soc. Jpn. **48**, 257 (1996).
3. K. Asai, T. Dotani, R. Hoshi, *et al.*, Publ. Astron. Soc. Jpn. **50**, 611 (1998).
4. A. Brinkman, J. Dam, W. Mels, *et al.*, *Nonthermal and Very High Temperature Phenomena in X-ray Astronomy*, Ed. by G. C. Perola and M. Salvati (Institute Astronomico, Rome, 1985), p. 263.
5. S. Campana, L. Stella, S. Mereghetti, *et al.*, Astrophys. J. **499**, L65 (1998a).
6. S. Campana, M. Colpi, S. Mereghetti, *et al.*, Astron. Astrophys. Rev. **8**, 279 (1998b).
7. S. Campana, L. Stella, S. Mereghetti, and D. Cremonesi, Astron. Astrophys. **358**, 583 (2000).
8. M. Cocchi, A. Bazzano, L. Natalucci, *et al.*, Astron. Astrophys. **346**, L45 (1999).
9. M. Cocchi, A. Bazzano, L. Natalucci, *et al.*, Astron. Astrophys. **378**, L71 (2001).
10. R. Cornelisse, F. Verbunt, J. in't Zand, *et al.*, Astron. Astrophys. **392**, 885 (2002a).
11. R. Cornelisse, F. Verbunt, J. in't Zand, *et al.*, Astron. Astrophys. **392**, 931 (2002b).
12. J. Dickey and F. Lockman, Ann. Rev. Astron. Astrophys. **28**, 215 (1990).
13. R. Jager, W. Mels, A. Brinkman, *et al.*, Astron. Astrophys., Suppl. Ser. **125**, 557 (1997).
14. R. Kaptein, J. in't Zand, E. Kuulkers, *et al.*, Astron. Astrophys. **358**, L71 (2000).
15. M. Pavlinsky, S. Grebenev, and R. Sunyaev, Astrophys. J. **425**, 110 (1994).
16. R. Remillard, private communication (2003).
17. R. Rutledge, L. Bildsten, E. Brown, *et al.*, Astrophys. J. **577**, 346 (2002).
18. W. Voges, B. Aschenbach, T. Boller, *et al.*, Astron. Astrophys. **349**, 389 (1999).
19. R. Warwick, A. Norton, M. Turner, *et al.*, Mon. Not. R. Astron. Soc. **232**, 551 (1988).
20. M. Watson, R. Willingale, J. Grindlay, and P. Hertz, Astrophys. J. **250**, 142 (1981).
21. S. Woosley and R. Taam, Nature **263**, 534 (1976).
22. J. in't Zand, J. Heise, J. Muller, *et al.*, Nucl. Phys. B (Proc. Suppl.) **69** (1–3), 228 (1998).
23. J. in't Zand, L. Kuiper, L. Amati, *et al.*, Astrophys. J. **559**, 710 (2001).
24. V. Zavlin, G. Pavlov, and Yu. Shibanov, Astron. Astrophys. **315**, 141 (1996).

Translated by G. Rudnitskiĭ

Astronomy Letters, Vol. 30, No. 2, 2004, pp. 95–99. Translated from Pis'ma v Astronomicheskiĭ Zhurnal, Vol. 30, No. 2, 2004, pp. 115–120.
Original Russian Text Copyright © 2004 by Popov, Soglasnov, Kondrat'ev, Kostyuk.

Polarization Observations of Giant Radio Pulses from the Millisecond Pulsar B1937+21 at a Frequency of 600 MHz

M. V. Popov[*], **V. A. Soglasnov**, **V. I. Kondrat'ev**, and **S. V. Kostyuk**

Astrospace Center, Lebedev Institute of Physics, Russian Academy of Sciences, Profsoyuznaya ul. 84/32,
Moscow, 117997 Russia

Received June 20, 2003

Abstract—We performed polarization observations of giant radio pulses from the millisecond pulsar B1937+21. The observations were carried out in July 2002 with the 64-m Kalyazin radio telescope at a frequency of 600 MHz in two polarization channels with left- and right-hand circular polarizations (RCP and LCP). We used the S2 data acquisition system with a time resolution of 125 ns. The duration of an observing session was 20 min. We detected twelve giant radio pulses with peak flux densities higher than 1000 Jy; five and seven of these pulses appeared in the RCP and LCP channels, respectively. We found no event that exceeded the established detection threshold simultaneously in the two polarization channels. Thus, we may conclude that the detected giant pulses have a high degree of circular polarization, with the frequency of occurrence of RCP and LCP pulses being the same.

Key words: *pulsars, giant pulses, polarization.*

INTRODUCTION

Only a few studies of the properties of giant radio pulses from the millisecond pulsar B1937+21 are known to date. Cognard *et al.* (1996) detected 60 giant pulses at a frequency of 430 MHz during 44 min of observations with the 305-m Arecibo radio telescope. Kinkhabwala and Thorsett (2000) analyzed the observations carried out sequentially at three frequencies, 430, 1420, and 2380 MHz, also with the Arecibo radio telescope. Soglasnov *et al.* (2003) studied giant pulses from the pulsar B1937+21 at 1650 MHz with a time resolution of 31.25 ns using the 70-m Tidbinbilla radio telescope. Over 39 min of observations, they found 309 giant pulses, with the most intense of them having a peak flux density of about 60 000 Jy. All of the detected giant pulses (except for one multicomponent pulse) were unresolved, and their observed shapes reflected the scattering of radio waves with a characteristic time scale of about 70 ns. Popov and Stappers (2003) analyzed the two-frequency observations of the millisecond pulsar B1937+21 with the Westerbork Synthesis Radio Telecope (2210–2250 MHz) and the 64-m Kalyazin radio telescope (1414–1446 MHz). These observations revealed no giant pulse at both frequencies, suggesting that the observed radio spectrum of the giant pulses is frequency-limited at least on a scale of $\Delta\nu/\nu < 0.5$. Of great importance in understanding the nature of giant radio pulses are polarization studies of these pulses. The only information about the polarization of giant radio pulses from the millisecond pulsar B1937+21 is the following brief comment by Cognard *et al.* (1996): Individual giant pulses often have a high degree of circular polarization, and giant pulses with both left- and right-hand circular polarizations (RCP and LCP) have been encountered. In this paper, we analyze the observations carried out in two polarization channels with the 64-m Kalyazin radio telescope at 600 MHz, with the aim of studying the polarization properties of giant radio pulses from the millisecond pulsar B1937+21.

OBSERVATIONS AND DATA PROCESSING

The observations were carried out on July 24, 2002, with the 64-m Kalyazin radio telescope. We used the Astrocomplex receiving system of the Laboratory of Pulsar Astrometry at the Pushchino Radio Astronomy Observatory and the S2 VLBI data acquisition system (Cannon *et al.* 1997; Wietfeldt *et al.* 1998). The central frequency of the reception band was 601.6 MHz. Two frequency channels (upper and lower subbands) with a 4-MHz channel bandwidth were recorded in each polarization channel. In each channel, the S2 system digitized the signal at the Nyquist rate (8 MHz) by means of a two-bit binary code with four quantization levels. The duration of an observing session was 20 min. The S2 records were

---

[*] E-mail: `mpopov@asc.rssi.ru`

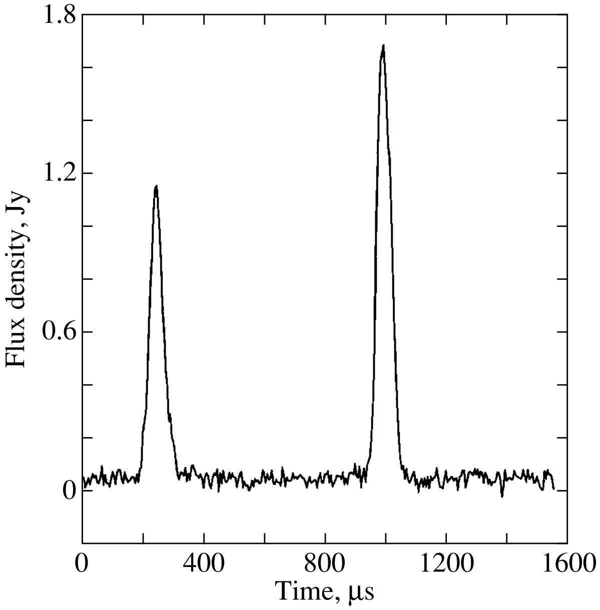

Fig. 1. The total profile obtained by averaging over all frequency and polarization channels during 20 min of observations. The presented data were time-averaged at a step of 4 μs.

played back with a special TCI interface designed at the Centre for Research in Earth and Space Technology (CRESTech), York University (Toronto, Canada), and installed at the Astrospace Center (Lebedev Institute of Physics, Russian Academy of Sciences). During signal decoding, we applied the required correction that depended on the current quantization level, as described by Jenet and Anderson (1998). The decoded data were then processed by the predetector dedispersion method (Hankins 1971; Hankins and Rickett 1975). In our case, the technique consisted of calculating the Fourier transform of the decoded data set of duration T followed by amplitude correction of the spectrum for the nonuniform passband and the phase correction for the dispersion delay of radio waves in the interstellar plasma. In restoring the signal, we used the DM = 71.025 pc cm^{-3} determined by Popov and Stappers (2003). For this dispersion measure, the pulse smearing in the 4-MHz band at 600 MHz is about 10 ms, i.e., slightly less than seven pulse repetition periods of the pulsar under study ($P = 1557.8$ μs). We restored all of the recorded signal in a piecewise continuous fashion. The time interval T for which the Fourier transform and the phase correction were made had a duration of 131.072 ms (1 048 576 readings), i.e., 84.2 pulsar pulse repetition periods. To restore the entire record, we had to superimpose these intervals with an overlap, because each time the information for the time interval equal to the pulse smearing time in the reception band is lost.

To increase the sensitivity in searching for giant pulses, we added up the signals in the two frequency channels of each polarization and analyzed the combined polarization channels separately. Soglasnov *et al.* (2003) showed that giant pulses remain unresolved in a 16-MHz band at 1650 MHz and that their observed shapes are entirely determined by the influence of radio-wave scattering on interstellar plasma nonuniformities. Cognard *et al.* (1996) and Kinkhabwala and Thorsett (2000) were inclined toward the same conclusion. According to the data of these authors, the expected scattering time at 600 MHz must be about 5 μs. Therefore, to increase the sensitivity, we time-smoothed the signal with a time constant of 625 ns (5 readings).

As was first clearly shown by Kinkhabwala and Thorsett (2000), the giant pulses from the pulsar B1937+21 appear in strictly limited longitude ranges, more specifically, in two about 5 μs-wide windows offset by 57 μs from the phase of the main-pulse maximum and by 65 μs from the phase of the interpulse maximum. We used this remarkable property of the giant pulses to search for new giant pulses in our observations; i.e., we checked the data for an excess above some intensity threshold only inside the above narrow time intervals ±20 μs in duration. After signal restoration by the predetector dedispersion method in each pulsar period inside the chosen longitude windows, we compared the amplitude of each reading with the specified threshold and saved the required information when this threshold was exceeded (10σ) for subsequent analysis.

THE AVERAGE PROFILE AND THE DIFFRACTION SPECTRUM OF SCINTILLATIONS

Concurrently with the search for giant pulses, we accumulated the profile averaged over all frequency and polarization channels and calculated the radio spectrum of the restored and dedispersed but undetected signal in the windows corresponding to the positions of the main pulse and the interpulse, as well as in the reference windows outside the pulse. These data were used to obtain the pattern of diffraction distortions of the radio spectrum due to the scattering of radio waves by interstellar plasma nonuniformities.

The total average profile obtained by adding up the signals in all frequency and polarization channels is shown in Fig. 1. The peak flux density at the maximum of the main pulse is 1.7 Jy, and the mean flux density in the main pulse and the interpulse when averaged over the period is 110 mJy. These values are based on the measurement of the equivalent system noise temperature, 170 Jy.

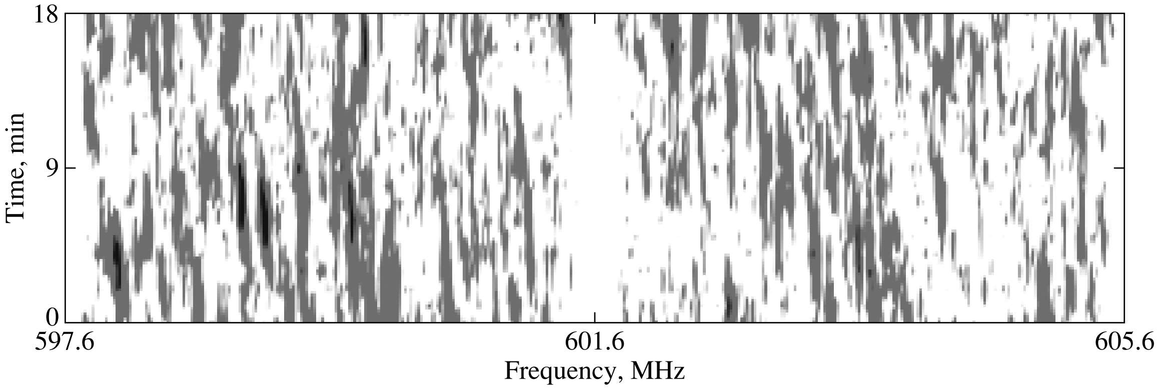

Fig. 2. The dynamic spectrum that shows the pattern of diffraction distortions of the radio spectrum and their evolution during the observing session. The data were averaged over the two polarization channels. Darker stripes correspond to higher intensities. The white spot in the middle of the frequency band is the boundary between the lower and upper video signal frequency bands.

Figure 2 shows the dynamic spectrum obtained by subtracting the radio spectrum outside the pulse from the spectrum computed in the windows corresponding to the positions of the main pulse and the interpulse. This pulse modulation provides high sensitivity in constructing the diffraction structure of the radio spectrum. The diffraction peaks, which are painted gray and black in the figure, have relative amplitudes of about 0.1% ($\Delta T/T \approx 10^{-3}$). The dynamic spectrum in Fig. 2 has an appearance typical of strong scintillations. The frequency decorrelation band that we determined at half maximum in the mean autocorrelation function was 33.6 kHz, and the expected time of pulse broadening by scattering determined from the relation $2\pi\tau\Delta\nu = 1$ must be 4.7 μs. Since the decorrelation band $\Delta\nu$ is more than a factor of 100 narrower than the reception band B, the temporal scintillations of the radio pulsar intensity must be significantly suppressed, and the expected modulation index m is about 10% ($m = \sqrt{\Delta\nu/B}$). Thus, the intensities of the regular and giant pulses must be approximately equal in the upper and lower reception bands. For the regular pulses, this equality was confirmed by comparing the average profiles obtained in the upper and lower bands in each polarization channel.

POLARIZATION PROPERTIES OF THE DETECTED GIANT PULSES

In searching for giant pulses using the procedure described in the section entitled Observations and Data Processing, we found 63 events that exceeded the 10σ level for the total signal in the two frequency bands. We analyzed each event individually and chose for subsequent analysis only the radio bursts that were observed simultaneously in both frequency bands of a given polarization channel (the dispersion delay between the frequency bands was taken into account). An additional criterion was the shape of the burst under consideration, which must correspond to the expected shape for the scattering of a short pulse by interstellar plasma nonuniformities for a real event; more specifically, the burst must have a steep leading edge and an exponential tail with a time constant of about 5 μs. There were only 12 such events: 7 in the LCP channel and 5 in the RCP channel. An example of a detected giant pulse is shown in Fig. 3. We see that the radio burst is present only in

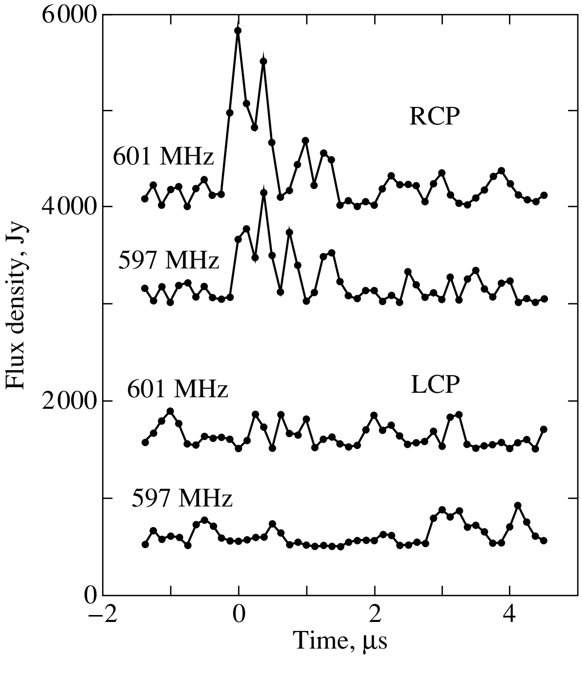

Fig. 3. An example of a giant pulse detected in the two RCP frequency channels. No statistically significant excess of the signal above the noise level is seen in the LCP frequency channels. The sampling interval is 125 ns.

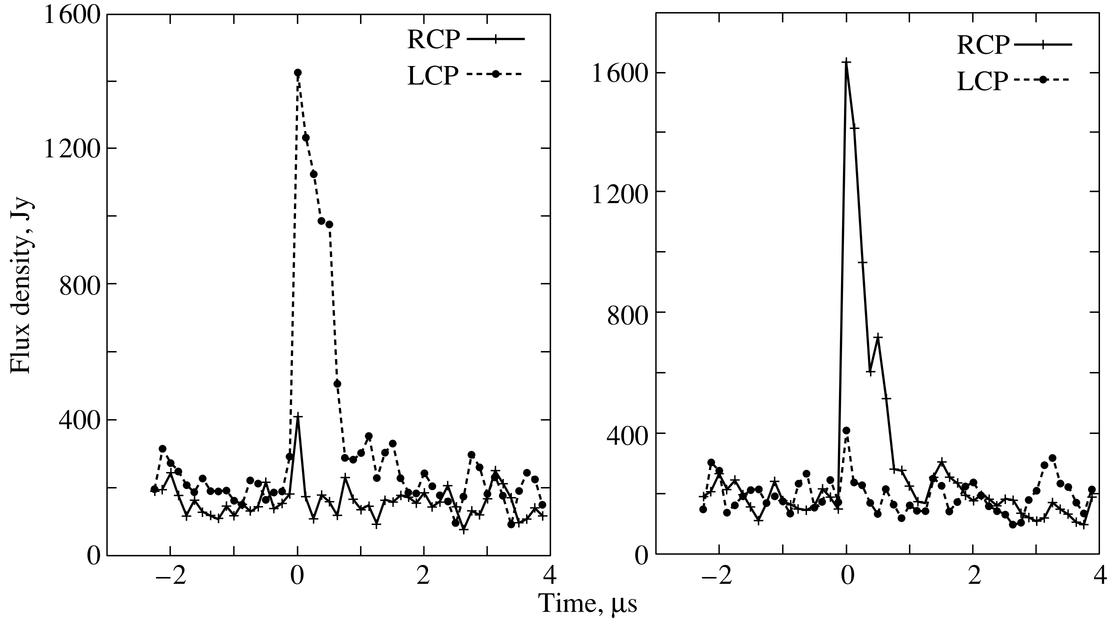

Fig. 4. The average profiles of the giant pulses detected in the LCP (a) and RCP (b) frequency channels. The averaged signal in the frequency channels with opposite polarization is also shown. The time resolution is 125 ns.

the RCP frequency channels. The other giant pulses that we detected also have this property, i.e., all of them appeared only in one polarization channel.

Figure 4 shows the "average profiles" of the detected giant pulses for the two polarization channels. In this case, we use the term "average profile" in quotation marks, because the giant pulses actually differ in occurrence phase, and they were averaged after a time shift through the mutual alignment of each pulse by its sharp leading edge; more specifically, they were aligned by the first point at which the flux density exceeded the 30% level of the peak value for a given giant pulse. We also added up the signals in the other polarization channel in which no visible traces of a signal excess above noise was seen with the same time shift. However, after averaging in the "quiet" polarization channel, the leading edge exhibited a significant deviation. Thus, as we see from Fig. 4, the giant pulses detected in the LCP channel are accompanied by a weak radio burst in the RCP channel and vice versa. The weak and short radio burst in the "quiet" polarization channel occurs at the leading edge of the giant pulse. In other words, all of the giant radio pulses that we detected have a high degree of circular polarization (LCP or RCP), and a weak linear polarization ($<10\%$) can be present only at the leading edge. As we already mentioned in the Introduction, Cognard *et al.* (1996) observed the same properties in giant pulses from the millisecond pulsar at 430 MHz. Hankins *et al.* (2003) reported the detection of isolated short pulses (<2 ns in duration) in the structure of giant pulses from the Crab pulsar. These nanosecond pulses also have a high degree of circular polarization, both LCP and RCP.

CONCLUSIONS

Giant radio pulses from pulsars are the shortest events of all those ever observed among astronomical objects. We may conclude from simple considerations (disregarding relativistic effects) that spatial scales of about one meter correspond to time scales of several nanoseconds; in this case, the measured instantaneous intensity of the giant radio pulses is indicative of a brightness temperature of about 10^{37}–10^{39} K (Soglasnov *et al.* 2003; Hankins *et al.* 2003). Undoubtedly, in studying the properties of giant radio pulses, we come close to the investigation of the true generation of coherent radio emission in an unsteady flow of relativistic electron–positron plasma in the magnetosphere of a neutron star. At present, we have no universally accepted model for this coherent mechanism, in which the energy release probably depends on specific local plasma parameters; their small changes can lead to great changes in the instantaneous intensity of a radio emission. The models for the formation of short micropulses in the radio emissions from pulsars are based on the analysis of nonlinear effects that arise when a stream of charged relativistic particles interacts with plasma waves in a pulsar magnetosphere (Asseo 1993). The high degree of circular polarization in the radio emission of giant pulses imposes severe constraints on the nature of the generation mechanism of these pulses.

ACKNOWLEDGMENTS

This work was supported by the Russian Foundation for Basic Research (project no. 01-02-16871) and the Federal Science and Technology Program for Astronomy. The pulsar receiving system on the Kalyazin radio telescope is maintained by the Laboratory of Pulsar Astrometry at the Pushchino Radio Astronomy Observatory headed by Yu.P. Ilyasov. We wish to thank V.V. Oreshko from this Laboratory for help in preparing and performing the observations. We also wish to thank S.F. Likhachev and A.V. Chibisov from the AstroSpace Center (Lebedev Institute of Physics, Russian Academy of Sciences) for maintaining the operation of the S2-TCI playback system.

REFERENCES

1. E. Asseo, Mon. Not. R. Astron. Soc. **264**, 940 (1993).
2. I. Cognard, J. A. Shrauner, J. H. Taylor, and S. E. Thorsett, Astrophys. J. **457**, L81 (1996).
3. W. H. Cannon, D. Baer, G. Feil, *et al.*, Vistas Astron. **41**, 297 (1997).
4. T. H. Hankins, Astrophys. J. **169**, 487 (1971).
5. T. H. Hankins and B. J. Rickett, *Methods in Computational Physics: Advances in Research and Applications,* Vol. 14: *Radio Astronomy,* Ed. by B. Alder, S. Fernbach, and M. Rotenberg (Academic, New York, 1975), p. 55.
6. T. H. Hankins, J. S. Kern, J. C. Weatherall, and J. A. Eilek, Nature **422**, 141 (2003).
7. F. A. Jenet and S. B. Anderson, Publ. Astron. Soc. Pac. **110**, 1467 (1998).
8. A. Kinkhabwala and S. E. Thorsett, Astrophys. J. **535**, 365 (2000).
9. M. V. Popov and B. Stappers, Astron. Zh. **80**, 635 (2003) [Astron. Rep. **47**, 660 (2003)].
10. V. A. Soglasnov, M. V. Popov, N. Bartel, *et al.*, Astrophys. J. (2003, in press).
11. R. D. Wietfeldt, W. Van Straten, D. Del Rizzo, *et al.*, Astron. Astrophys., Suppl. Ser. **131**, 549 (1998).

Translated by G. Rudnitskii